

DISSERTATION

# Flow Patterns and Valve Dynamics in Multi-Valve Reciprocating Compressors

ausgeführt zum Zwecke der Erlangung des akademischen Grades eines  
Doktors der technischen Wissenschaften unter der Leitung von

Ao.Univ.Prof. Dipl.-Ing. Dr. techn. Herbert Steinrück  
E322  
Institut für Strömungslehre und Wärmeübertragung

eingereicht an der Technischen Universität Wien  
Fakultät für Maschinenwesen und Betriebswissenschaften

von

Dipl.-Ing. Thomas Müllner  
Matrikelnummer 9925693  
2120 Wolkersdorf, Am Stiegl 5

Wien, im September 2015

# Contents

<b>1</b>	<b>Introduction</b>	<b>5</b>
1.1	Objective of the Thesis . . . . .	5
1.2	Compressor Working Principle . . . . .	6
1.3	Historical Development . . . . .	6
1.4	Application of CFD . . . . .	7
1.5	Valve Simulation and Valve Life . . . . .	10
1.6	Heat Transfer . . . . .	10
1.7	Outline . . . . .	12
<b>2</b>	<b>Compressor Model Setup</b>	<b>14</b>
2.1	Working Chamber . . . . .	14
2.1.1	Dimensions . . . . .	15
2.1.2	Operating Conditions . . . . .	17
2.2	Valves . . . . .	17
2.2.1	Geometric Parameters . . . . .	18
2.2.2	Flow Parameters . . . . .	21
2.2.3	Mechanical Parameters . . . . .	21
<b>3</b>	<b>Physical Description</b>	<b>23</b>
3.1	Models for a Reciprocating Compressors . . . . .	23
3.2	Equations for Fluid Flow . . . . .	23
3.2.1	Navier-Stokes Equations . . . . .	23
3.2.2	Euler Equations . . . . .	25
3.2.3	Material Equation . . . . .	27
3.2.4	Entropy Equation . . . . .	27
3.2.5	Isentropic Relations . . . . .	28
3.2.6	Sound Speed and Mach Number . . . . .	28
3.2.7	Rankine-Hugoniot Conditions . . . . .	29
3.2.7.1	Contact Discontinuity . . . . .	31
3.2.7.2	Shock Discontinuity . . . . .	31
3.3	Boundary Conditions for Fluid Flow . . . . .	31
3.3.1	Walls . . . . .	32
3.3.2	Valves . . . . .	32
3.4	The Idealized Compressor Process . . . . .	34
3.4.1	Pressure over Volume and Crank Angle . . . . .	34

3.4.2	Instantaneous Mass Flow and Driving Power . . . . .	35
3.4.3	Average Mass Flow and Driving Power . . . . .	36
3.5	Estimates for Solid Body Motion . . . . .	36
<b>4</b>	<b>Properties of Partial Differential Equations</b>	<b>38</b>
4.1	Introduction to PDEs . . . . .	38
4.2	System of Non-Linear PDEs . . . . .	38
4.2.1	Rotational Invariance . . . . .	39
4.2.2	Local Linearization . . . . .	40
4.2.3	Hyperbolicity . . . . .	41
4.3	System of Linear PDEs . . . . .	41
4.3.1	Eigenvalues and Eigenvectors . . . . .	41
4.3.2	Diagonalization and Wave Decomposition . . . . .	42
4.4	Linear Scalar Advection-Diffusion Equation . . . . .	42
4.4.1	Wave Solutions . . . . .	42
4.4.2	Total Variation . . . . .	45
4.5	Non-Linear Scalar Advection Equation . . . . .	46
<b>5</b>	<b>Numerical Methods</b>	<b>47</b>
5.1	Introduction in Numerics . . . . .	47
5.2	Approximation Methods . . . . .	47
5.2.1	Point Values and Mean Values . . . . .	49
5.2.2	Interpolation and Reconstruction . . . . .	51
5.2.2.1	Local Interpolation Trough Points . . . . .	51
5.2.2.2	Local Reconstruction Of Mean Values . . . . .	52
5.2.3	Approximation Accuracy . . . . .	53
5.3	Linear Scalar Advection Equation . . . . .	54
5.3.1	Cauchy Kowalewski Procedure . . . . .	54
5.3.2	Finite Difference Methods . . . . .	54
5.3.2.1	First Order Upwind Scheme . . . . .	54
5.3.2.2	Second Order Central Scheme . . . . .	55
5.3.2.3	Third Order Upwind-Biased Scheme . . . . .	57
5.3.3	Finite Volume Methods . . . . .	57
5.3.3.1	First Order Upwind Scheme . . . . .	58
5.3.3.2	Second Order Central Scheme . . . . .	59
5.3.3.3	Third Order Upwind-Biased Scheme . . . . .	60
5.3.3.4	High Resolution Scheme . . . . .	60
5.3.4	Numerical Diffusion . . . . .	61
5.3.5	Von Neumann Stability . . . . .	62
5.3.5.1	First Order Upwind Scheme . . . . .	63
5.3.5.2	Second Order Central Scheme . . . . .	63
5.3.5.3	Third Order Upwind-Biased Scheme . . . . .	64
5.3.6	TVD Stability . . . . .	64
5.3.7	TVD Flux Limiter . . . . .	65

<b>6</b>	<b>Numerical Euler-Equation Solver</b>	<b>70</b>
6.1	Godunov Method . . . . .	71
6.2	Godunov-Type Methods . . . . .	71
6.3	Roe Method . . . . .	72
6.3.1	Numerical Flux on Moving Meshes . . . . .	74
6.4	Mesh Strategy . . . . .	75
6.4.1	Moving Structured Cylinder Mesh . . . . .	75
6.4.2	Non-Moving Unstructured Valve Pocket Mesh . . . . .	77
6.4.3	Interface Coupling Method . . . . .	78
6.5	Positivity Criterion . . . . .	80
6.6	Numerical Boundary Conditions for Valves . . . . .	82
6.6.1	Suction Valve . . . . .	82
6.6.2	Discharge Valve . . . . .	83
<b>7</b>	<b>Results</b>	<b>86</b>
7.1	Results Overview . . . . .	86
7.2	Investigated Cases . . . . .	87
7.3	Global Flow Properties . . . . .	88
7.3.1	Mass and Massflows . . . . .	88
7.3.2	Valve Plate Motion . . . . .	90
7.3.2.1	Original Valve-Spring Data . . . . .	90
7.3.2.2	Smaller Valve-Spring Stiffness and Maximal Plate Lift . . . . .	91
7.3.2.3	Valve Plate Lifts and Velocities . . . . .	92
7.3.3	Valve Plate Forces and Piston Force . . . . .	97
7.4	Local Flow Properties . . . . .	100
7.4.1	Pressure Distribution on the Piston . . . . .	100
7.4.1.1	After Discharge Valve Opening . . . . .	100
7.4.1.2	At the Top-Dead-Center . . . . .	102
7.4.1.3	After the Top-Dead-Center . . . . .	103
7.4.2	Velocity Distribution near the Piston . . . . .	105
7.4.3	Mach-numbers for Subsonic and Supersonic Flow . . . . .	106
<b>A</b>	<b>Roe 3D-Solver Derivation</b>	<b>108</b>
A.1	Basic Idea . . . . .	108
A.2	Roe Condition . . . . .	108
A.3	Roe Averages . . . . .	109
A.3.1	Eigenvalues and Eigenvectors . . . . .	110
A.3.2	Characteristic Variables . . . . .	111
A.4	Intermediate States . . . . .	112
<b>B</b>	<b>Solver Testing</b>	<b>113</b>
B.1	Motivation . . . . .	113
B.2	Modified Shock Tube Test . . . . .	115
B.2.1	Test Case Description . . . . .	115
B.2.2	3D-Model Setup . . . . .	115

B.2.3 Comparison 1d/3d-Results . . . . .	117
<b>Reference</b>	<b>119</b>
<b>Curriculum Vitae</b>	<b>123</b>

# Chapter 1

## Introduction

### 1.1 Objective of the Thesis

The objective of the presented thesis is to investigate the three-dimensional flow of gas inside the working chambers of multi-valve reciprocating compressors and the fluid-structure interaction (FSI) with the self-acting suction and discharge valves, that control the mass and energy flow to the suction and discharge chambers, having pressure  $p_s$  and  $p_d$ , respectively. In the original goal of the thesis, the heat transfer from the gas to the walls based on a three-dimensional flow simulation was thought to be included. However, if the heat flow is part of interest, for large compressors this may be computed in a post-processing procedure. The flow occurring in a reciprocating compressor is highly unsteady, and the flow patterns in the working chambers are expected to be extremely influenced by geometrical design parameters and operating conditions. Therefore, a self-developed CFD-solver using the unsteady Euler equations for an arbitrary moving domain (ALE formulation) is presented, that offers the ability to easily modify the number of valves incorporated, and to locate them at any arbitrary angular position along the circumferential surface of the cylinder, without the need for creating a completely new geometry or mesh. In Figure 1.1, important parameters used within this work are sketched for a barrel design reciprocating compressor in horizontal arrangement.

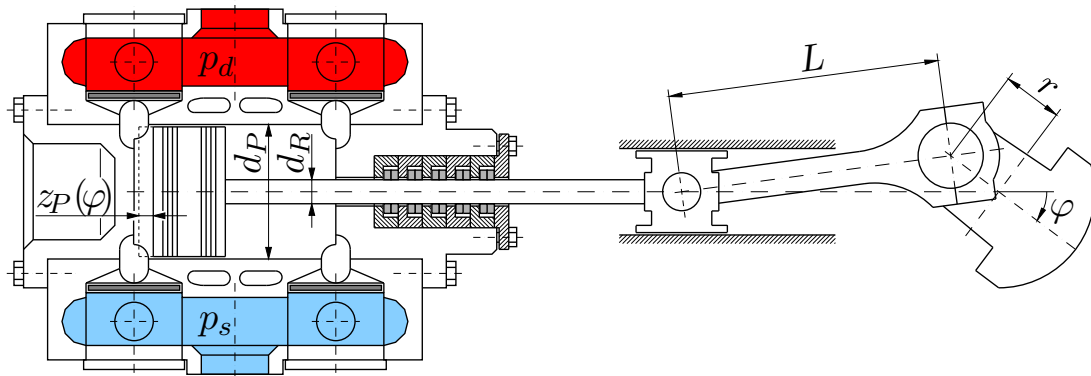


Figure 1.1: Main parameters of a barrel design horizontal reciprocating compressor

## 1.2 Compressor Working Principle

The task of a reciprocating compressor is to compress gas stored in the suction chamber with pressure  $p_s$  to a higher pressure  $p_d > p_s$  in the discharge chamber. The motion of the driven crank shaft, rotating with constant angular speed  $\dot{\varphi}$ , changes the position of the piston  $z_P(\varphi)$  with diameter  $d_P$ , and the volume inside the working chamber  $V(\varphi)$ , according to Equations (1.1) and (1.2).

$$z_P(\varphi) = r - r \cos \varphi + L - \sqrt{L^2 - r^2 \sin^2 \varphi}. \quad (1.1)$$

$$V(\varphi) = V_{min} + \frac{\pi}{4}(d_P^2 - d_R^2)z_P(\varphi). \quad (1.2)$$

The working chamber volume has its minimum value  $V_{min}$  at  $\varphi = 0$ , and its maximum value at  $\varphi = \pi$ . If the gas inside the working chamber does not enclose a piston rod, the piston rod diameter  $d_R$  has to be set equal to zero in Equation (1.2), to ensure the correct computation of the volume  $V(\varphi)$ . Since the crank angle  $\varphi = \dot{\varphi} t$  is a function of time  $t$ , the actual piston velocity  $v_P(t) = \dot{\varphi} \frac{d}{d\varphi} z_P(\varphi)$  is the time-derivative of the piston position. On the other hand, with the time  $2\pi/\dot{\varphi}$  the crank shaft needs to complete a full rotation of angle  $2\pi$ , and with the distance  $4r$  the piston travels in that time, the average piston velocity

$$\bar{v}_P = \frac{2}{\pi} r \dot{\varphi} \quad (1.3)$$

can be defined. The time-dependend change of the working chamber volume causes the gas to change density  $\rho$  and pressure  $p$ . As a consequence, the self-acting suction and discharge valves sketched in grey color in Figure 1.1, open and close according to the pressure difference of working chamber pressure  $p$ , and the pressure in the suction and discharge chambers, respectively. A detailed description of the pressure-volume diagram important for the thermodynamic description of a compressor is shown in Bloch & Hoefner [12] or Küttner [47].

## 1.3 Historical Development

A good overview of the historical development of reciprocating compressor design and operating conditions with a special focus on the fifth edition of the API Standard 618 “Reciprocating Compressors for Petroleum, Chemical and Gas Industry Services”. is given by Kopschick [46]. The article discusses what is the “allowable speed” of a reciprocating compressor, yet in API 618 these terms are not defined sharp. The reason behind is, that the standard originally applied only to low-speed reciprocating compressors for refinery service. Kopschick [46] categorizes low-speed according to the rotating speeds shown in Table 1.1.

	Low-Speed	Moderate-Speed
Rotating speed (rpm)	200-600	600-1200

Table 1.1: Low and moderate compressor rotating-speeds

In that terminology, high-speed compressors run at rotation speeds larger than 1200 rpm. Compressors installed in the early 1900s were operated at approximately 100 rpm, while during the 1950s and 1960s most reciprocating compressors installed in refineries were either integral engine/compressors, electric motor, or steam turbine driven. Averaged piston speed needed to be limited to about  $3.8\text{ m/s}$ , or maximal  $3.6\text{ m/s}$  for unlubricated compressors, in order to achieve the desired three years of uninterrupted operation between maintenance. These compressors usually run at 300 rpm, while those operating over 300 rpm did not provide the desired uninterrupted service life.

In contrary to the integral unit low-speed compressors, moderate-speed compressors are driven by gas engines operating at 1000 rpm or higher. Originally they were used in oil and gas production, where the required time of uninterrupted service is not that critical as for a refinery application. Based on the improvements of high-speed compressors, commonly running at 1400 rpm without changing the wear parts during 18 month of uninterrupted operation, moderate-speed compressors suitable for critical service application were developed, using new designs and materials. For example, Kopsick [46] mentions a 4.5 inch ( $114.3\text{ mm}$ ) stroke high speed compressor designed for 1500 rpm ( $5.72\text{ m/s}$ ), that can be used in an API 618 application when operated at either 900 rpm ( $3.4\text{ m/s}$ ) or 720 rpm ( $2.7\text{ m/s}$ ). Today, when nonmetallic materials and new compressor valve designs are used, piston speeds of  $4.2\text{ m/s}$  to  $4.4\text{ m/s}$  are quite common. Nonlubricated compressors are typically limited to  $3.8\text{ m/s}$  averaged piston speed.

## 1.4 Application of CFD

With increasing rotational speed and modern design of process gas compressors, usually having a bore to stroke ratio larger than 1, the flow inside the working chambers and through the valve ports gains more and more interest.

Cyklis [20] used a commercial software package for the simulation of the flow through the self-acting suction valve of a compressor with a rather simple geometry. Birari et al. [11] show an example of a refrigerator compressor using a combination of structured and unstructured meshes to consider the complexity of the geometry, while keeping computational expenses, numerical diffusion and setup time in mind. Nowadays, commercial CFD software is frequently used to investigate the influence of internal compressor flow on the valves and pressure losses. An example for applying CFD during the design stage of a large bore process gas compressor with a piston diameter up to  $1.2\text{ m}$  is given by Koop [45]. The presented CFD-results suggest a modification of the conventional valve location to a configuration where the valve ports are moved outside the running zone of the piston.

Although a CFD simulation with a moving piston is possible, Pratelli et al. [64] perform a steady state RANS calculation with a  $k\text{-}\omega$  turbulence model locating the



piston in an intermediate position, where it does not mask the gas passages between cylinder chamber and valves, denominated as valve pockets. Furthermore, the valve geometry was substituted by an equivalent porous media model for the evaluation of pressure losses due to suction and discharge valve flow. The authors mention, that this approach allows for using an unstructured tetrahedral mesh without the need of re-constructing and re-meshing the geometries. In their presentation, the complexity of the flow patterns along the suction and discharge flow paths can be clearly seen. Since cylinder chamber, valve pockets, valve cages and valve unloaders are included in their simulation, the number of elements is quite large (15 million elements).

For compressors having only two valves, one suction valve and one discharge valve respectively, many designs do not need a detailed three-dimensional flow calculation to describe the interaction of the pressure waves inside the working chamber with the valve dynamics, as long as unsteady flow effects are considered. Including unsteady effects during valve opening was proposed by Böswirth [13]. However, the modified Bernoulli equation used by Böswirth [13] does not seem to represent the correct physical situation. Simulations for a reciprocating compressor using the one-dimensional (1d) unsteady Euler equations with a variable cross section area for the cylinder domain description have been performed by Machu [53], showing good agreement with measurements. An important argument for the 1d-simulation is, that in daily business, the exact geometry of the machine is not available, and that the computation time is very short compared with a full three-dimensional model. With this simple model, it is possible to describe the in-cylinder pressure wave running back and forth across the piston. Hence, this phenomena explains the increased power requirement during discharge as an unsteady effect. In order to avoid the pulsations, Machu [52] recommends to use a tapered piston. However, such a configuration can not easily be considered in a 1d-model.

Aigner et al. [3],[4] simulated compressors with two valves based on a self-coded CFD-solver for the 1d-Euler equations, and compared the results with measurements. For cases where more than two valves are involved, Aigner [6] extended the flow computation, applying the 2d-unsteady-Euler equations in the cylinder plane using a variable height in axial direction, while applying the 1d-model for the flow inside the valve pockets. Thus, this method may be classified as a 2d/1d-hybrid for cylinder flow and valve pocket flow, respectively. Figure 1.2 illustrates a categorization of different models for the CFD-calculation of reciprocating compressors, used by different authors from the fluid mechanics institute at TU-Vienna, in terms of spatial dimensions, number of valves, and consideration of viscous effects.

Rovaris & Deschamps [75] developed a combined method of integral and differential formulations using large eddy simulation (LES) for the flow through the discharge valves. Important flow features, like pressure overshoots and recirculating flow have been observed. A further simplified numerical method for the in-cylinder flow at the top dead center was presented by Ribas & Deschamps [68]. The authors

mention, that gas inertia plays an important role for compressors with large bore and small clearance between the piston and the cylinder head, and that the mass flow through the closing discharge valve may be larger than the predicted one by steady state theory. The whole operating cycle of a small refrigeration reciprocating compressor based on a two-dimensional model was simulated by Matos et al.[58], including the flow inside the cylinder and through the suction and discharge valves. Kerpici & Oguz [43] used a transient modeling for the flow through the suction port and valve leaves of a hermetic reciprocating compressor for fixed valve lifts. Three-dimensional (3d) simulations for a process gas compressor with two valves using the 3d-unsteady Navier–Stokes equations with a Reynolds-averaged turbulence model have been performed by Meyer [59], relying on a commercial software package. Meyer [59] implemented the model for the valve flow and the valve dynamics in that software applying a user defined function. A 3d-flow computation for a reciprocating compressor requires to solve the equations on a moving zone, while the masking of the piston causes severe challenges, e.g. at the conjunction of cylinder and valve pocket domains. Furthermore, the detailed representation of the complex valve pocket geometries automatically requires the use of unstructured meshes, especially for modern multi-valve compressor designs, that try to minimize the size of the working chamber volume near the pistons top dead center.

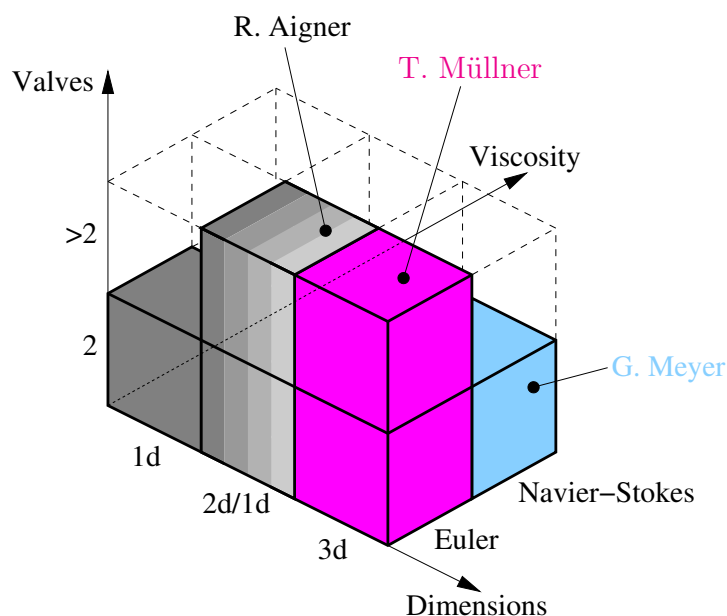


Figure 1.2: Reciprocating compressor CFD-models used by authors at TU-Vienna

Although additional difficulties in three dimensions have to be considered, a self-coded CFD-solver for a moving grid in combination with a so-called conservative non-conformal sliding mesh interface was developed by the present author. Such an interface, today frequently used for moving meshes in geometrically complex

industrial applications, allows extreme flexibility in geometrical valve pocket design and mesh generation, namely an unstructured tetrahedral mesh, while keeping the advantages of a structured hexahedral grid for re-meshing and solution interpolation on the cylinder domain.

## 1.5 Valve Simulation and Valve Life

The motion of valve sealing elements is an important topic for the layout of a reciprocating compressor. The sealing element shows interaction with the flow inside the working chamber and the flow in the valve cages, respectively. Furthermore, the impact velocity of the valve sealing elements on the valve seat or the valve guard is a measure for valve life. One of the first approaches for the modeling of the dynamics of spring loaded valves was the mass-spring model of Costagliola [18]. Modifications and extensions of this simple model are still in use, e.g. see the comparative analysis of Pereira et al. [62]. Flade [29] computed the effect of the unsteady flow through the valve ports on the valve elements. For the dynamics of reed valves, a simulation tool was developed by Machu et al. [55]. Machu [54] recognized, that the pulsations inside the working chambers are a potential reason for the damage of valves. The effects of valve plate dynamics on valve life and compressor performance are discussed in Brun et al. [14]. Manfrone & Raggi [57] use measurements and a dynamic CFD simulation to investigate how the lift of a valve plate depends on the position relative to the cylinder. They also include a non-zero impact angle of the valve sealing element in their consideration, usually referred as valve plate tumbling. An automatic meshing tool for CFD is used to investigate the valve flow and pressure loss, coupling two straight ducts during valve design stage, with the goal of gaining more insight in the flow and valve dynamic interaction.

## 1.6 Heat Transfer

For large compressors, the heat flow from the gas inside the working chamber to the compressor walls, or vice versa, is in general relatively small compared with the cycle-averaged in- or outstreaming enthalpy flows. Therefore, assuming the surrounding walls as adiabatic, works very well for many situations. However, if a compressor is small and operated with a very high pressure ratio  $p_d/p_s$ , leading to a high gas temperature at the end of compression, the heat flow may not be negligible. Since the heat flux is the product of the temperature difference of gas and wall, and the convective heat transfer coefficient, it is necessary to compute both of them accurately. Usually, the temperature of the walls is assumed to be a prescribed function in space, e.g. a constant, that is not changing with respect to time. The change of gas temperature is mainly caused by gas compression and expansion inside the compressors working chamber, while the occurring wall heat flow has only a little effect on the gas temperature. Anyway, the computation of the convective heat transfer coefficient is a difficult task, because it highly depends on local flow patterns inside the working chamber. Therefore, it is necessary to trust

on an unsteady 3d-simulation for accurate flow and heat transfer prediction. For the compressor of a truck braking system with a piston diameter  $d_P = 0.1\text{ m}$  and a pressure ratio  $p_d/p_s = 13.5$ , Müllner & Bielmeier [60] investigated the convective heat transfer for different valve configuration in detail, using a commercial software package with an unsteady RANS turbulence model ( $k\text{-}\varepsilon$ ). The CFD-results for the instantaneous heat flow through the walls  $\dot{Q}(t)$ , may then be used together with the pistons instantaneous driving power  $P(t)$  and the in- and outstreaming enthalpy flows  $\dot{m}_{in}(t) h_s$  and  $\dot{m}_{out}(t) h_d$ , sketched in Figure 1.3 for a motor driven compressor,

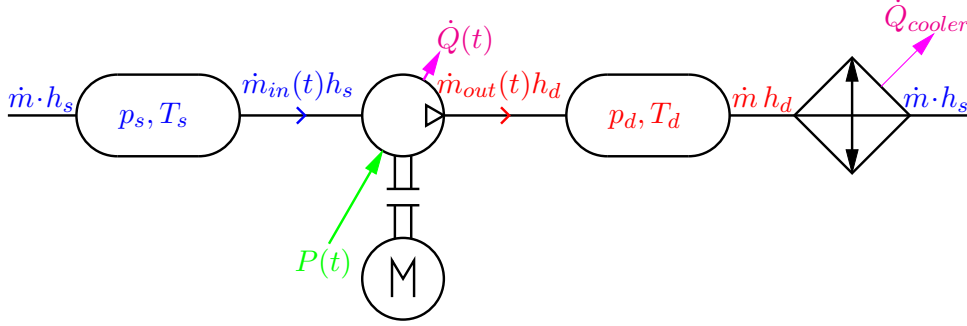


Figure 1.3: Energy flows of a motor driven reciprocating compressor

to apply the first law of thermodynamics

$$\frac{d}{dt}H(t) = P(t) - \dot{Q}(t) + \dot{m}_{in}(t) h_s - \dot{m}_{out}(t) h_d. \quad (1.4)$$

Hence, according to Baehr [9] and Baehr & Stephan [10], the time-derivative of the enthalpy inside the working chamber  $H(t)$  simply equals the right side of Equation (1.4). In case of a time-periodic solution, the time average of Equation (1.4) over one period gives  $0 = \bar{P} - \bar{\dot{Q}} - \dot{m} (h_d - h_s)$ , where  $\dot{m}$  is the time-independent mass flow before and after the pulsation dampers at suction and discharge side, respectively. For the braking system compressor mentioned above, it turns out, that the ratio of cycle averaged heat flow and average driving power  $|\bar{\dot{Q}}|/\bar{P}$  is between 7.8% and 9.2%, depending on the specific location of the suction and discharge valves in the cylinder head. Although these results are obtained under the assumptions of a constant wall temperature, both values indicate, that the heat loss is quite small compared to the increase of enthalpy flow  $\dot{m} (h_d - h_s)$ . However, for piston compressors even smaller than  $d_P = 0.1\text{ m}$ , e.g. used in refrigerators, the net heat flow may be of the same order as the time-averaged piston driving power. It can be expected for even smaller fast-running compressors, that the heat transfer has a major influence on the thermodynamic cycle. Hermetic compressors that are completely encapsulated, are investigated by Abidin et al. [1] and Burgstaller [15]. For a very simple compressor geometry with a single rigid reed valve at suction and discharge side, the heat transfer was computed based on a  $k\text{-}\varepsilon$  model and the logarithmic wall function by Pereira et al. [63]. The results illustrate, that the raise of heat flux during suction is caused by the incoming flow, leading to a higher convective heat

transfer coefficient on valve plate, piston and cylinder wall respectively.

For combustion engines simpler correlations for the heat transfer exist, that are based on mixed theoretical models and experimental data. The most prominent are that of Woschni [87] and Annand [7]. It may be a goal to find simpler correlations for the heat flow also for reciprocating compressors. One of the first attempts to find a formula for the Nußelt number depending on Reynolds number and Prandtl number was given by Adair et al. [2], based on experimental investigation. Recently, Disconzi et al. [22] used CFD-results for a very simple compressor geometry to find correlations for the Nußelt number. From CFD-results obtained by the present author, it can be observed, that there is a strong correlation of the heat flow with the flow of enthalpy passing the suction valves and discharge valves. The ratio of heat flow to enthalpy flow is a Stanton number, that is usually dependent on the friction coefficient, e.g. in turbulent pipe flows. As shown by Aigner & Steinrück [5], the agreement of CFD-obtained heat flows and estimated heat flows using Stanton numbers multiplied with enthalpy flows is excellent during suction and discharge. A major drawback of this description, is that these Stanton numbers are obtained by fitting the CFD-results, and are not derived from first principles. A minor drawback of this method for the application in reciprocating compressors, is the unknown characteristic flow speed, when all valves are closed. The time-independent average piston speed does not seem to be a very meaningful reference velocity for the flow during this phase. As a consequence, no adequate measures for the mass and enthalpy flows during the time of closed valves are known as well. However, the heat flow estimates may be improved significantly, if temporal and spatial velocities near the walls are known from 3d-CFD calculations obtained in acceptable computational time.

## 1.7 Outline

After the short introduction into the topic of reciprocating compressors, the structure of the thesis includes the specific compressor model setup in terms of dimensions and operation conditions, followed by the physical descriptions of the compressor models in different forms. Some important mathematical properties of the models convenient for the numerical solution-finding are discussed. A brief overview of numerical methods other than that used for the compressor solver, is also included in the thesis. The effects of numerical methods are then demonstrated for the solution of simple linear 1d test-equations. This also gives an impression of possible improvements of the methodology used at the moment. What follows, is a special focus on the Euler-solver and its Roe approximate Riemann solver in ALE-formulation, used for the reciprocating compressor with its permanently moving geometries and meshes. The mesh strategy is presented, and the implementation of numerical boundary conditions for the valves are described in detail.

After this, results are presented and discussed in the last chapter, to demonstrate the conservation property, the functionality, and the flexibility of the solver for any number and location of suction and discharge valve pockets. A proof of solver robustness is the supersonic flow appearing for a short time in a compressor running with overspeed. In order to allow the reader to focus on the main topic, a detailed derivation of the Roe solver in 3d, and a comparison of results derived with a 1d and 3d version of the Euler-solver for the famous shock tube test are deferred to the appendix.

# Chapter 2

## Compressor Model Setup

This chapter provides a short introduction in the design details of a reciprocating compressor, and shows the setup of the working chamber model, that is used for the numerical computations within the presented work. The dimensions and the operating conditions of the cases calculated with the model are collected in tables, and the parameters of the suction and discharge valves, that build the boundary conditions of the model, are derived from basic considerations.

### 2.1 Working Chamber

The working chamber of a reciprocating compressor consists of the space inside the liner, a cylindrical domain that guides the motion of the back and forth going piston, and ports that connect the cylinder with the valves, usually referred to as valve pockets. Figure 2.1, download from <http://woodgroupfs.com/compressor-pump-repair.html>, offers a look inside the working chamber of a typical process gas reciprocating compressor with 8 poppet valves, when the cylinder head is removed.



Figure 2.1: Working chamber with removed cylinder head

The location of the valves is usually along the circumferential surface of the cylinder for large bore compressors. Smaller compressors can be found, that have their valves located in the cylinder head, or a combination of both situations. Many designs exist, where the geometry of the suction valve pockets and the discharge valve pockets are geometry the same. Therefore, in the present work the connecting channels of the valves to the cylinder are represented by a single geometry. However, the parameter settings of suction valves and discharge valves may be completely different. The angular positions of the valve pockets along the circumferential surface are not regular distributed for all designs. The chosen description herein basically allows to locate a pre-designed valve pocket geometry at any angular location. Placing the valve pockets completely on the cylinder head surface is thinkable for the actual working chamber model, but requires to create the geometry and the mesh for the valve pockets of such an arrangement. However, in order to allow better fluid flow and do not have any restrictions in terms of cross-section, at least a fraction of the original cylinder head surface should be used to connect the cylindrical part of the working chamber with the valve pockets.

### 2.1.1 Dimensions

The dimensions of the working chamber model used for the computed cases are sketched in Figure 2.2, showing the cartesian coordinate system  $(x, y, z)$  as well.

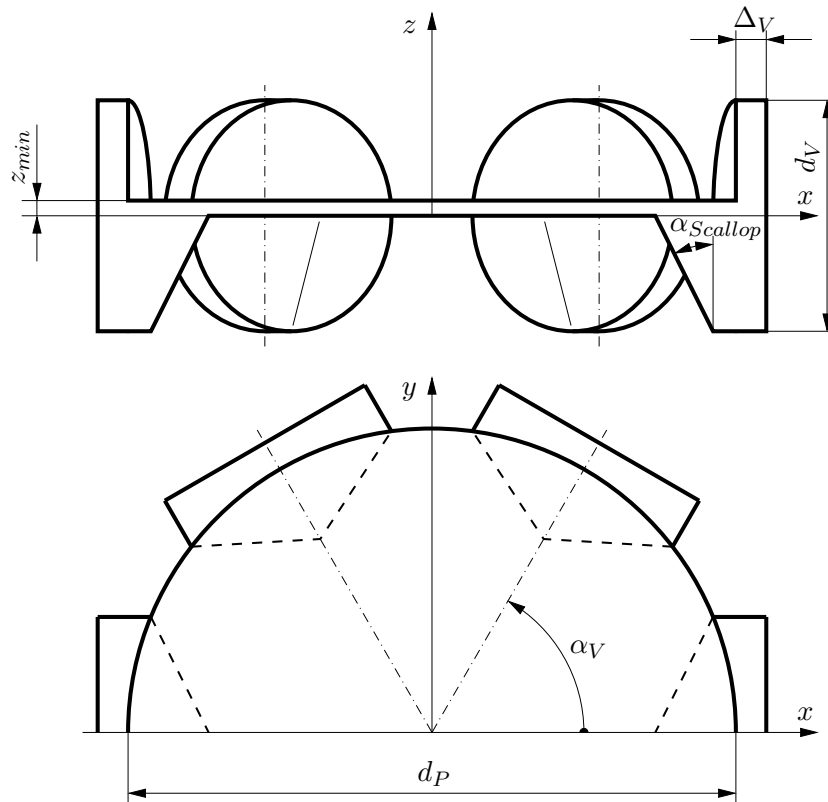


Figure 2.2: Dimensions of the working chamber model



Only one half of the geometry used for the simulations is shown. The presented model uses the complete cylinder and does not allow to split the geometries of the valve pockets in the middle. The geometry representation is quite simple, but includes the basic features of a reciprocating compressors working chamber. The piston is flat, having a piston diameter  $d_P$ , and its minimal distance to the cylinder head surface is  $z_{min}$ . In order to allow the fluid inside the cylinder to easily flow into the valve pocket domain, a cone-shaped scallop builds the connection of the valve pocket with the cylinder head surface at  $z = 0$ . The distance of the valves to the piston is  $\Delta_V$ . A cylindrical part of the valve pocket with diameter  $d_V$  connects the valve with the circumferential surface swept partially by the piston. It is possible, to set the angular location  $\alpha_V$  of the valve pockets along the cylinder circumference for every single suction and discharge valve. Table 2.1 lists the dimensions for four different cases, presented in this work. Figure 7.1 in section 7 gives an good impression of the compressor dimensions, illustrating the huge difference in size of the cases 1,2,3 and 4. Since for these cases, the working chambers do not enclose the rod, the piston rod diameter  $d_R$  listed in Table 2.1 is irrelevant.

Case	1	2	3	4
$r$ (m)	0.075	0.075	0.075	0.075
$L$ (m)	0.300	0.300	0.300	0.300
$d_P$ (m)	0.680	0.340	0.170	0.085
$d_R$ (m)	0.050	0.050	0.050	0.050
$d_V$ (m)	0.200	0.125	0.080	0.054
$z_{min}$ (m)	0.0015	0.0015	0.0015	0.0015
$\Delta_V$ (m)	0.004	0.004	0.004	0.004
$\alpha_{Scallop}$ ( $^\circ$ )	22	24	23	10
$\alpha_{V,Suc,1}$ ( $^\circ$ )	108	112.5	120	135
$\alpha_{V,Suc,2}$ ( $^\circ$ )	144	157.5	180	225
$\alpha_{V,Suc,3}$ ( $^\circ$ )	180	202.5	240	
$\alpha_{V,Suc,4}$ ( $^\circ$ )	216	247.5		
$\alpha_{V,Suc,5}$ ( $^\circ$ )	252			
$\alpha_{V,Dis,1}$ ( $^\circ$ )	288	292.5	300	315
$\alpha_{V,Dis,2}$ ( $^\circ$ )	324	337.5	0	45
$\alpha_{V,Dis,3}$ ( $^\circ$ )	0	22.5	60	
$\alpha_{V,Dis,4}$ ( $^\circ$ )	36	67.5		
$\alpha_{V,Dis,5}$ ( $^\circ$ )	72			

Table 2.1: Dimensions and angular valve location for different cases

With the given geometrical parameters, the ratio  $\varepsilon = V_{min}/[\frac{\pi}{4}(d_P^2 - d_R^2) 2r]$  built with  $V_{min}$  in Equation (1.2) and the volume swept by the piston  $\frac{\pi}{4}(d_P^2 - d_R^2) 2r$  is  $\varepsilon = 0.126$  for cases 1, 2, 3 and 4, respectively. The ratio of crank-radius to connecting rod length  $\lambda = r/L$  becomes  $\lambda = 0.25$  for all cases. Both ratios,  $\varepsilon$  and  $\lambda$ , are important dimensionless reciprocating compressor quantities, see also Equation (3.39) for more details.

## 2.1.2 Operating Conditions

As can be seen in Table 2.1, all cases have a crank radius of  $r = 0.075\text{ m}$ . If a barrel design as shown in Figure 1.1 is used for each of these cases, a boxer compressor consisting of four barrels driven by a single crank shaft can be built. Setting the angular crank speed to  $800\text{ rpm}$  or  $\dot{\varphi} = \frac{\pi}{30}800\text{ rad/s}$  leads to an averaged piston speed of  $4\text{ m/s}$ , common for an API 618 application. The cases 1, 2, 3 and 4 can be thought of as the stages of a gas compression process, where the gas is compressed in barrel 1 and cooled down to the suction temperature after compression, before it flows into the suction chamber of barrel 2, and so forth. Since, for an ideal gas the density  $\rho$  is proportional to pressure divided by temperature, an increase of suction pressure  $p_s$  leads to increased suction density  $\rho_s$  as well, if the suction temperature  $T_s$  is thought to be the same. Table 2.2 collects the operating conditions for the presented cases.

Case	1	2	3	4
$\dot{\varphi}\text{ (rad s}^{-1}\text{)}$	$\frac{\pi}{30}800$	$\frac{\pi}{30}800$	$\frac{\pi}{30}800$	$\frac{\pi}{30}800$
$\rho_s\text{ (kg m}^{-3}\text{)}$	1.0	4.0	16.0	64.0
$p_s\text{ (Pa)}$	$1 \cdot 10^5$	$4 \cdot 10^5$	$16 \cdot 10^5$	$64 \cdot 10^5$
$p_d\text{ (Pa)}$	$4 \cdot 10^5$	$16 \cdot 10^5$	$64 \cdot 10^5$	$256 \cdot 10^5$

Table 2.2: Operating conditions for different cases

The piston diameter of a stage is chosen half the value of the previous stage. Thus, based on simple geometrical and thermodynamical considerations, a pressure ratio  $p_d/p_s = 4$  allows to fill the gas of a stage in the barrel of the next stage, because the cycle-averaged mass flow can be expected to be the same for all stages.

## 2.2 Valves

The proper design of valves is a significant issue for the layout of a reciprocating compressor. Therefore, the flow properties of a valve depending on the geometrical and mechanical parameters are briefly discussed in this section. Although the cases shown within the present work are just examples, it may be desired to be quite realistic. For reciprocating compressors valves with different valve elements are used. A plate valve, as shown in Figure 2.3, has a single moving part, the valve plate, located between the valve plate seat and the guard. In combination with the valve springs, shown in Figure 2.3 in red color, the plate forms a mass-spring system.



Figure 2.3: Plate valve

Valves consisting of more than one moving part are ring valves or poppet valves. Although these valves allow better conditions for the flow through the valves than plate valves, the motion of the moving elements is not that easy to control as for a single plate. Therefore, as a first attempt, only plate valves are further discussed herein.

### 2.2.1 Geometric Parameters

The dimensions of a plate valve, important for the flow through the valves, are sketched in Figure 2.4. The plate is shown in fully open position with maximal valve plate lift  $x_{V,max}$ . Valves can be used either as suction valves or discharge valves, depending on the main flow direction. In Figure 2.4 the valve seat ports are located at the lower side, while the valve guard ports are on the upper side of the sketch.

For a discharge valve, the flow coming from the compressor working chamber enters the ports on the valve seat side. The gas then streams through the cuts of the valve plate and finally reaches the discharge chamber after passing the guard ports. This situation is also illustrated by the red arrow lines in Figure 2.5.

On the other hand, using the valve as a suction valve, the flow coming from the suction chamber enters the ports on the guard side, and then flows into the compressors working chamber passing the valve plate and the seat ports.

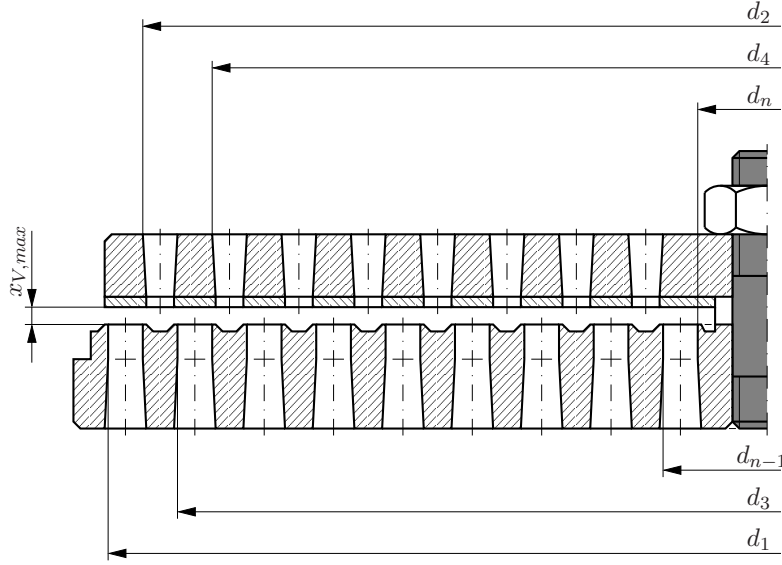


Figure 2.4: Dimensions of a plate valve

With the outer diameters  $d_1, d_3, \dots, d_{n-1}$  of the valve seat ports and the inner diameters  $d_2, d_4, \dots, d_n$  of the ports, the geometrical passage area  $f_e(x_V)$  between valve plate and valve plate seat depends on the actual valve plate lift  $x_V$ , and on the geometrical passage area per valve lift  $f_{e1mm}$ .

$$f_e(x_V) = f_{e1mm} x_V, \quad (2.1)$$

$$f_{e1mm} = (d_1 + d_2 + d_3 + d_4 + \dots + d_{n-1} + d_n) \pi. \quad (2.2)$$

In Table 2.3, the seat port diameters used to calculate  $f_{e1mm}$  within the present work are listed for the valves applied to the cases 1, 2, 3 and 4. The corresponding valve diameters  $d_V$  are given in Table 2.1.

It is worth to mention, that within the present work, the data in Table 2.3 is only used to compute an estimate for  $f_{e1mm}$  and the valve cross sections based on a given valve size. It is definitely not meant to describe the geometrical valve features in every detail. For a detailed layout of valves, a lot of know-how and experience from valve producing and delivering companies is required. However, the choice of the presented diameters are expected to be at least plausible in combination with the other compressor dimensions and operation parameters.

Case	1	2	3	4
$d_1(m)$	0.190	0.116	0.072	0.047
$d_2(m)$	0.180	0.107	0.064	0.040
$d_3(m)$	0.170	0.098	0.056	0.033
$d_4(m)$	0.160	0.089	0.048	0.026
$d_5(m)$	0.150	0.080	0.040	0.019
$d_6(m)$	0.140	0.071	0.032	0.012
$d_7(m)$	0.130	0.062	0.024	–
$d_8(m)$	0.120	0.053	0.016	–
$d_9(m)$	0.110	0.044	–	–
$d_{10}(m)$	0.100	0.035	–	–
$d_{11}(m)$	0.090	0.026	–	–
$d_{12}(m)$	0.080	0.017	–	–
$d_{13}(m)$	0.070	–	–	–
$d_{14}(m)$	0.060	–	–	–
$d_{15}(m)$	0.050	–	–	–
$d_{16}(m)$	0.040	–	–	–
$d_{17}(m)$	0.030	–	–	–
$d_{18}(m)$	0.020	–	–	–

Table 2.3: Valve seat port diameters used to calculate  $f_{e1mm}$

Based on the diameters in Table 2.3, the cross sectional area of the valve seat ports  $f_{ports}$  can be calculated using the sum of ring sectional areas

$$\begin{aligned}
f_{ports} &= \frac{\pi}{4} [(d_1^2 - d_2^2) + (d_3^2 - d_4^2) + \dots + (d_{n-1}^2 - d_n^2)] \\
&= \pi \left[ \frac{d_1 + d_2}{2} \frac{d_1 - d_2}{2} + \frac{d_3 + d_4}{2} \frac{d_3 - d_4}{2} + \dots + \frac{d_{n-1} + d_n}{2} \frac{d_{n-1} - d_n}{2} \right]. \quad (2.3)
\end{aligned}$$

If all ports have the same radial width  $\Delta_{ports} = \frac{d_1 - d_2}{2} = \frac{d_3 - d_4}{2} = \dots = \frac{d_{n-1} - d_n}{2}$ , the area of the ports simplifies to

$$f_{ports} = \frac{\Delta_{ports}}{2} (d_1 + d_2 + d_3 + d_4 + \dots + d_{n-1} + d_n) \pi = \frac{\Delta_{ports}}{2} f_{e1mm}. \quad (2.4)$$

For the flow through the valves, it is not favourable to feel large changes in the size of the cross sectional area, while passing the ports and the passage between valve plate and seat. Therefore, the maximal valve plate lift  $x_{V,max}$  may be chosen in such a way, that the maximal geometrical passage area  $f_e(x_{V,max}) = f_{e1mm} x_{V,max}$  is of the same size as the area of the ports. Setting  $f_e(x_{V,max}) \approx f_{ports}$  gives

$$x_{V,max} \approx \frac{f_{ports}}{f_{e1mm}} = \frac{\Delta_{ports}}{2}. \quad (2.5)$$

## 2.2.2 Flow Parameters

For the flow to occur between valve plate and seat it can not be expected to be able to fully use the geometrically available area. Therefore, the contraction of the nozzle-like flow must be considered in some sense. In order to describe the effective passage area  $\phi(x_V)$  for the flow, the geometrical passage area  $f_e(x_V)$  must be modified by a correction function  $\zeta(x_V)$  depending on the valve plate lift  $x_V$  and on the coefficients  $\alpha$  and  $\beta$ , usually determined by measurements.

$$\phi(x_V) = \frac{f_{e1mm} x_V}{\sqrt{\zeta(x_V)}}. \quad (2.6)$$

$$\zeta(x_V) = \alpha + \beta x_V^2. \quad (2.7)$$

Although herein  $\alpha$  and  $\beta$  are not known, and in general are specific for a particular valve design, an estimate can be made. In the limit of small and large valve plate lifts

$$\lim_{x_V \rightarrow 0} \phi(x_V) = \frac{f_{e1mm} x_V}{\sqrt{\alpha}}, \quad \lim_{x_V \rightarrow \infty} \phi(x_V) = \frac{f_{e1mm}}{\sqrt{\beta}}, \quad (2.8)$$

it shows that  $\alpha$  plays a role for small  $x_V$ , while  $\beta$  dominates the  $\phi(x_V)$ -behaviour for large  $x_V$ . Since  $\phi(x_V)$  has to be definitely smaller than the geometrical passage area  $f_{e1mm} x_V$  for small  $x_V$ , and smaller than  $f_{e1mm} x_{V,max}$  for large  $x_V$ , it can easily be seen, that the conditions

$$\alpha > 1, \quad \beta > \frac{1}{x_{V,max}^2}, \quad (2.9)$$

are necessary. With this knowledge in mind, the parameters chosen for the valves used in the compressor flow simulations are set to  $x_{V,max} = \Delta_{ports}/2$ ,  $\alpha = 2$ ,  $\beta = 1.125/x_{V,max}^2$ . Using equation (2.2) and the port diameters given in Table 2.3 gives the values shown in Table 2.4.

Case	1	2	3	4
$x_{V,max} (m)$	$2.5 \cdot 10^{-3}$	$2.25 \cdot 10^{-3}$	$2.0 \cdot 10^{-3}$	$1.75 \cdot 10^{-3}$
$f_{e1mm} (m)$	5.938	2.507	1.106	0.556
$\alpha (1)$	2.0	2.0	2.0	2.0
$\beta (m^{-2})$	$1.800 \cdot 10^5$	$2.222 \cdot 10^5$	$2.813 \cdot 10^5$	$3.673 \cdot 10^5$

Table 2.4: Valve design parameters used for the flow simulations

## 2.2.3 Mechanical Parameters

The mechanical parameters are responsible for the valve plate dynamics. A sketch of the valve plate opening procedure is shown in Figure 2.5.

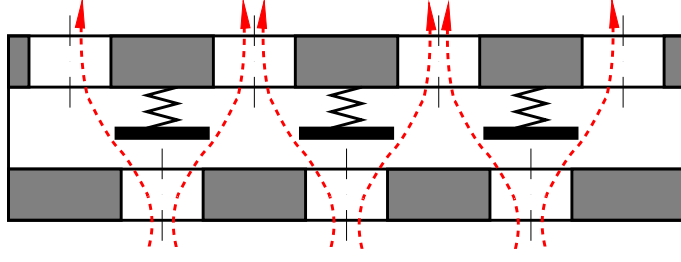


Figure 2.5: Mass-spring model for the valve plate

The gas pressure  $p$  acts on the so-called force area  $A_f$  on both sides of the valve plate with mass  $m_V$ , and causes a pressure force  $\Delta p A_f$  due to the pressure difference  $\Delta p = p_{seat} - p_{guard}$  of seat side and guard side pressure. Using a mass-spring model

$$m_V \frac{d^2 x_V}{dt^2} = \Delta p A_f - k_V (x_V + L_V) \quad (2.10)$$

the lift of the valve plate  $x_V = x_V(t)$  depends on the spring constant  $k_V$ , and the initial deflection of the springs  $L_V$ . If the plate sits on the seat ( $x_V = 0$ ) and is not accelerated ( $dx_V^2/dt^2 = 0$ ), the valve is still closed at the pressure difference  $\Delta p_{closed} = k_V L_V / A_f$ , and opens after  $\Delta p_{closed}$  is exceeded. If the plate is caught by the guard ( $x_V = x_{V,max}$ ) and not accelerated ( $dx_V^2/dt^2 = 0$ ), the valve is fully open at the pressure difference  $\Delta p_{open} = k_V (x_{V,max} + L_V) / A_f$ , and starts to close if the pressure difference falls below  $\Delta p_{open}$ . Hence, the spring constant and the spring initial deflection can be written as

$$k_V = \frac{(\Delta p_{open} - \Delta p_{closed}) A_f}{x_{V,max}}, \quad (2.11)$$

$$L_V = \frac{\Delta p_{closed}}{\Delta p_{open} - \Delta p_{closed}} x_{V,max}. \quad (2.12)$$

The force area  $A_f = 1.2 f_{ports}$  is estimated to be 20% larger than the area of the ports given in equation (2.3). The valve plate mass is calculated using  $m_V = \rho_{steel} A_f \delta$ , where  $\rho_{steel} = 7850 \text{ kg m}^{-3}$  is the density of the plate material, and  $\delta = 1.5 \cdot 10^{-3} \text{ m}$  is the thickness of the plate. The plate area is assumed to be equal with the force area  $A_f$ . The choice  $\Delta p_{closed} / (\Delta p_{open} - \Delta p_{closed}) = 0.3$  gives  $L_V = 0.3 x_{V,max}$ , and  $\Delta p_{closed} = 0.01 p_s$  gives  $k_V = 0.01 p_s A_f / L_V$ . Table 2.5 shows the values used for the simulations.

Case	1	2	3	4
$A_f \text{ (m}^2\text{)}$	$1.781 \cdot 10^{-2}$	$6.769 \cdot 10^{-3}$	$2.654 \cdot 10^{-3}$	$1.168 \cdot 10^{-3}$
$m_V \text{ (kg)}$	$210 \cdot 10^{-3}$	$79.7 \cdot 10^{-3}$	$31.3 \cdot 10^{-3}$	$13.8 \cdot 10^{-3}$
$k_V \text{ (N m}^{-1}\text{)}$	23750	40112	70774	142352
$L_V \text{ (m)}$	$7.5 \cdot 10^{-4}$	$6.75 \cdot 10^{-4}$	$6.0 \cdot 10^{-4}$	$5.25 \cdot 10^{-4}$

Table 2.5: Mechanical valve parameters used for the simulations

# Chapter 3

## Physical Description

### 3.1 Models for a Reciprocating Compressors

The goal of this section is to present the physical models, that describe the motion of the fluid inside the working chamber of a reciprocating compressor, and to give some important information of the required boundary conditions, e.g. the average piston velocity. The mathematical description starts with the differential form of the Navier-Stokes equations, and simplifications based on dimensionless numbers, that lead to the integral form of the Euler-equations on an arbitrary moving domain, suitable for the description of the flow inside a reciprocating compressor. This so-called ALE-formulation of the Euler-equations is the basis for the numerical solver presented in section 6. In order to close the system of equations, the material equation for ideal gas is given as a function of the state variables, suitable for the finite volume discretization method described in section 6.

The physical boundary conditions of moving and non-moving walls are presented, and the boundary conditions of valves are described based on the assumption of isentropic flow through the valves. The concept of isentropic flow is also used for the idealized compressor process, assuming zero valve losses and an adiabatic compression and expansion of an inviscid fluid. In section 7.3, the idealized compressor process is used for comparison with the massflows obtained from CFD-results. Furthermore, the Rankine-Hugoniot jump conditions are presented for the Euler-equations. In section 6.6 the Rankine-Hugoniot conditions are used in the sense of a Godunov-method as a numerical boundary condition for suction and discharge valves.

### 3.2 Equations for Fluid Flow

#### 3.2.1 Navier-Stokes Equations

In continuous fluid mechanics the motion of a single-phase fluid can be described by the Navier-Stokes equations, see e.g. Laney [48]. The transport-equations for



mass per volume  $\rho$ , momentum per volume  $\rho \mathbf{u}$  and total inner energy per volume  $\rho e + \rho \|\mathbf{u}\|^2/2$  in differential form read

$$\frac{\partial}{\partial t} \rho + \nabla \cdot (\rho \mathbf{u}) = 0, \quad (3.1)$$

$$\frac{\partial}{\partial t} (\rho \mathbf{u}) + \nabla \cdot (\rho \mathbf{u} \mathbf{u} - \boldsymbol{\sigma}) = \rho \mathbf{g}, \quad (3.2)$$

$$\frac{\partial}{\partial t} \left( \rho e + \rho \frac{\|\mathbf{u}\|^2}{2} \right) + \nabla \cdot \left[ \rho \mathbf{u} \left( e + \frac{\|\mathbf{u}\|^2}{2} \right) - \boldsymbol{\sigma} \cdot \mathbf{u} + \mathbf{q} \right] = \rho \mathbf{g} \cdot \mathbf{u}, \quad (3.3)$$

where  $\boldsymbol{\sigma}$  is the stress tensor, and  $\mathbf{q}$  is the heat flux density vector. Forces per volume are considered by the term  $\rho \mathbf{g}$  in Equation (3.1). The Navier-Stokes equations have a first time derivative  $\partial/\partial t$  of the state variables, and space derivatives  $\nabla = [\partial/\partial x, \partial/\partial y, \partial/\partial z]^\top$  that appear on the left side of the Equations (3.1), (3.2), (3.3) as a divergence of fluxes. Integration over a control volume allows to find the integral form of the Navier-Stokes equations. The divergence property of the fluxes easily allows to transform the volume integrals over the divergence of the fluxes into flux integrals over the surface of the control volume, by simply applying the divergence theorem. This so-called conservation property of the Equations (3.1), (3.2), (3.3) is an important argument for the use of finite volume methods, when searching for approximate solutions of the Navier-Stokes equations.

For the computation of the flow inside a reciprocating compressor, some simplifications of the field equations are considered. Introducing reference quantities  $\rho_{\text{ref}}$ ,  $u_{\text{ref}}$ ,  $L_{\text{ref}}$ , for density, length and velocity, the relevance of the terms, e.g. in Equation (3.2) can be discussed based on dimensionless numbers. For a reciprocating compressor, the suction density  $\rho_s$ , the average piston velocity  $\bar{v}_P$  from Equation (1.3), and four times the crank radius  $4r$  seem to be a natural choice for these reference quantities. The reference time  $t_{\text{ref}} = L_{\text{ref}}/u_{\text{ref}}$  automatically turns out to be the time  $2\pi/\dot{\varphi}$  needed for a full crank rotation. Applying the reference values  $\rho_{\text{ref}}$ ,  $u_{\text{ref}}$ ,  $L_{\text{ref}}$  to a scaling of kinematic and kinetic quantities

$$\tilde{t} = \frac{t}{L_{\text{ref}}/u_{\text{ref}}}, \quad \tilde{\rho} = \frac{\rho}{\rho_{\text{ref}}}, \quad \tilde{\mathbf{x}} = \frac{\mathbf{x}}{L_{\text{ref}}}, \quad \tilde{\mathbf{u}} = \frac{\mathbf{u}}{u_{\text{ref}}}, \quad \tilde{\boldsymbol{\sigma}} = \frac{\boldsymbol{\sigma}}{\rho_{\text{ref}} u_{\text{ref}}^2}, \quad \tilde{\mathbf{g}} = \frac{\mathbf{g}}{u_{\text{ref}}^2/L_{\text{ref}}} \quad (3.4)$$

gives for Equation (3.2) multiplied with  $L_{\text{ref}}/(\rho_{\text{ref}} u_{\text{ref}}^2)$ , the dimensionless equation  $\partial(\tilde{\rho} \tilde{\mathbf{u}})/\partial \tilde{t} + \tilde{\nabla} \cdot (\tilde{\rho} \tilde{\mathbf{u}} \tilde{\mathbf{u}} - \tilde{\boldsymbol{\sigma}}) = \tilde{\rho} \tilde{\mathbf{g}}$ , where  $\tilde{\nabla} = [\partial/\partial \tilde{x}, \partial/\partial \tilde{y}, \partial/\partial \tilde{z}]^\top$  is the non-dimensional Nabla operator. The term  $\rho \mathbf{g}$  on the right side of Equation (3.2) represents a body force per volume. A prominent example is a gravitational force, where  $\mathbf{g}$  is the gravity vector. The Froude number

$$Fr = \frac{u_{\text{ref}}^2}{g L_{\text{ref}}} \quad (3.5)$$

is a measure for the ratio of inertia to gravity force, where  $g = \|\mathbf{g}\|$  is the modulus of the gravitation vector. For compressors running at high speed  $u_{\text{ref}}$ , the Froude

number is usually large. Therefore, the term  $\tilde{\rho} \tilde{\mathbf{g}}$  can be neglected compared to the order one term  $\partial(\tilde{\rho} \tilde{\mathbf{u}})/\partial \tilde{t} + \tilde{\nabla} \cdot (\tilde{\rho} \tilde{\mathbf{u}} \tilde{\mathbf{u}} - \tilde{\boldsymbol{\sigma}}) = \mathcal{O}(1)$ . Hence, the expressions  $\rho \mathbf{g}$  in Equation (3.2) and  $\rho \mathbf{g} \cdot \mathbf{u}$  in Equation (3.3) are not considered. The magnitude of the viscous forces for a Newtonian fluid can be estimated with  $\nu \rho_{\text{ref}} u_{\text{ref}}/L_{\text{ref}}$ , where  $\nu$  is the molecular viscosity and  $u_{\text{ref}}/L_{\text{ref}}$  is a measure for the strain rate. An expression that measures the inertia of fluids is twice the stagnation pressure  $\rho_{\text{ref}} u_{\text{ref}}^2$ . Dividing this pressure by the estimate for the viscous stresses gives the Reynolds number

$$Re = \frac{u_{\text{ref}} L_{\text{ref}}}{\nu}. \quad (3.6)$$

In flows with large Reynolds numbers, e.g. large reciprocating compressors running on high average piston speed, forces due to molecular viscosity can be neglected compared to the inertia forces almost everywhere in the fluid domain. However, in a thin zone close to the walls, the boundary layers, the size of the viscous forces becomes comparable with the inertia terms. For a viscous fluid, the no-slip boundary condition  $\mathbf{u} = \dot{\mathbf{x}}$  has to be applied at the wall, where  $\dot{\mathbf{x}} = [\dot{x}, \dot{y}, \dot{z}]^\top$  is the velocity of the moving wall. However, if the boundary layers are neglected, the boundary condition for an impermeable wall  $(\mathbf{u} - \dot{\mathbf{x}}) \cdot \mathbf{n} = \mathbf{0}$ , where  $\mathbf{n}$  is the unit normal vector of the wall, has to be used instead of the no-slip condition. Since for  $Re \rightarrow \infty$  the molecular viscosity  $\nu$  of the fluid does not appear in the equations anymore, the fluid is sometimes said to be “inviscid”. Scaling the pressure  $p = \rho_{\text{ref}} u_{\text{ref}}^2 \tilde{p}$ , where  $\tilde{p} = \mathcal{O}(1)$ , shows that for  $Re \rightarrow \infty$  the viscous terms  $\mathbb{T} = \mathcal{O}(\nu \rho_{\text{ref}} u_{\text{ref}}/L_{\text{ref}})$  in the stress tensor  $\boldsymbol{\sigma} = -p \mathbf{I} + \mathbb{T}$  are negligible compared to the pressure component  $p \mathbf{I} = \mathcal{O}(\rho_{\text{ref}} u_{\text{ref}}^2)$ . Hence, the stress tensor reads  $\boldsymbol{\sigma} = -p \mathbf{I}$  for inviscid fluids, where  $\mathbf{I}$  is a  $3 \times 3$  identity matrix. Furthermore, as already discussed in the introduction in section 1.6, for large compressors the heat flow is rather small compared with the time-averaged power driving the piston, or compared with the flow of enthalpy passing the valves. A local and time-dependent dimensionless quantity is the Stanton number

$$St = \frac{(\mathbf{q} \cdot \mathbf{n}) A_{\text{ref}}}{h_{\text{ref}} \dot{m}_{\text{ref}}}, \quad (3.7)$$

where  $\mathbf{q} \cdot \mathbf{n}$  is the heat flux component normal to a wall with reference area  $A_{\text{ref}}$ , and  $h_{\text{ref}} \dot{m}_{\text{ref}} = (e_{\text{ref}} + p_{\text{ref}}/\rho_{\text{ref}}) \dot{m}_{\text{ref}}$  is a reference enthalpy flow, e.g. built with the massflow  $\dot{m}_{\text{ref}}$  passing the suction or discharge valves. The Stanton number as defined in Equation (3.7) is not really a characteristic number, because it depends on results, and not on predefined scales derived from boundary conditions. However, the Stanton number can be expected to be small. Therefore, the heat flux  $\mathbf{q}$  in Equation (3.3) is neglected. If the heat transfer at the walls is of interest, the flow can first be computed assuming zero heat flux. With the flow solution given, the relatively small heat flux can then be calculated afterwards.

### 3.2.2 Euler Equations

If the effects of viscosity and heat flux are neglected in the transport equations for mass, momentum and inner energy, the Navier-Stokes equations become the

Euler-equations. For that set of equations, discontinuous solutions for the density and the inner energy become possible, see e.g. the shock-solutions in section 3.2.7. For the finding of discontinuous solutions on moving domains, it is convenient to use the Arbitrary Lagrangian Eulerian (ALE) framework of the Euler equations, see Marie et al.[56]. This so-called integral form of the Euler equation can be obtained by integrating the transport equations in differential form over a time-depending domain  $V(t)$

$$\frac{d}{dt} \underbrace{\int_{V(t)} \begin{bmatrix} \rho \\ \mathbf{M} \\ E \end{bmatrix} dV}_{\text{states}} + \underbrace{\oint_{S(t)} \begin{bmatrix} \rho(\mathbf{u} - \dot{\mathbf{x}}) \cdot \mathbf{n} \\ \mathbf{M}(\mathbf{u} - \dot{\mathbf{x}}) \cdot \mathbf{n} + p \mathbf{n} \\ E(\mathbf{u} - \dot{\mathbf{x}}) \cdot \mathbf{n} + p \mathbf{u} \cdot \mathbf{n} \end{bmatrix} dS}_{\text{fluxes}} = \mathbf{0}, \quad (3.8)$$

where  $S(t)$  is the surface of the domain moving with velocity  $\dot{\mathbf{x}}$ , and  $\mathbf{n}$  is the out-pointing unit normal vector related to every surface element  $dS$ . The domain surface appears because the divergence theorem for the transformation of volume and surface integrals has been applied. The state vector  $\mathbf{U} = [\rho, \mathbf{M}^\top, E]^\top$  consists of the density  $\rho$ , the momentum per volume  $\mathbf{M} = \rho \mathbf{u}$ , and the total inner energy per volume  $E = \rho e + \rho |\mathbf{u}|^2/2$ . The additional terms in the fluxes depending on  $\dot{\mathbf{x}}$  are caused by the motion of the domain surface. In contrast to the partial time derivative  $\partial/\partial t$  in the differential form of the equations, the total time derivative  $d/dt$  of the volume integrals appears in the integral formulation. A domain moving with the velocity of the fluid  $\dot{\mathbf{x}} = \mathbf{u}$  is referred to as Lagrange formulation, while the non-moving domain  $\dot{\mathbf{x}} = 0$  is referred to as Euler formulation. Therefore, the transport equations written on an arbitrary moving domain are called ALE-formulation. In compact form, Equation (3.8) can be written as

$$\frac{d}{dt} \mathcal{U}(t) + \mathcal{F}(t) = \mathbf{0}, \quad (3.9)$$

where  $\mathcal{U}(t)$  contains the volume integrals of the state variables, and  $\mathcal{F}(t)$  contains the integrals of fluxes over the surface  $S(t)$ . In physical terms  $\mathcal{F}(t)$  is the flow of the state quantities. The integral form of the transport equations for mass, momentum and inner energy, are more general than the differential form. Although only the Euler equations are presented in integral form, the Navier-Stokes equations can be written in the same fashion as Equation (3.9) as well. Source terms, e.g. volume forces, are not considered here. It is worth to mention, that for smooth solutions, the total derivative of any scalar quantity  $a$  can be written as

$$\frac{d}{dt} \int_{V(t)} a dV = \int_{V(t)} \frac{\partial a}{\partial t} dV + \oint_{S(t)} a \dot{\mathbf{x}} \cdot \mathbf{n} dS. \quad (3.10)$$

Hence, in contrast to the ALE-formulation, the velocity of the domain boundary  $\dot{\mathbf{x}}$  does not show up in the differential form of the Euler equations

$$\frac{\partial}{\partial t} \mathbf{U} + (\nabla \cdot \hat{\mathbf{f}}(\mathbf{U}))^\top = \mathbf{0}, \quad (3.11)$$

where the  $3 \times 5$  flux matrix  $\hat{\mathbf{f}}(\mathbf{U}) = [\mathbf{M}, \mathbf{M}\mathbf{M}/\rho + p\mathbf{I}, (E + p)\mathbf{M}/\rho]$  depends solely on the state variables, when the pressure  $p = p(\mathbf{U})$  is prescribed using the material equation. In the notation of Equation (3.11),  $\nabla$  is a  $1 \times 3$  object, the dot-product with  $\hat{\mathbf{f}}(\mathbf{U})$  gives a  $1 \times 5$  object, while its transpose gives a  $5 \times 1$  vector comparable with the state vector  $\mathbf{U}$ . Note that  $\mathbf{M}\mathbf{M}$  is a dyadic product of two  $3 \times 1$  objects forming a  $3 \times 3$  matrix.

### 3.2.3 Material Equation

The equation for the material  $p = p(\mathbf{U})$  is necessary to close the description for fluid motion. For ideal gas with constant specific heat capacities  $c_v$  and  $c_p$ , the temperature  $T = e/c_v$  only is a function on the specific inner energy. Using  $\mathcal{R}/\mathcal{M} = c_p - c_v$ , where  $\mathcal{R}$  is the universal gas constant and  $\mathcal{M}$  is the molar mass, and the ratio of heat capacities  $\gamma = c_p/c_v$ , the pressure equation  $p = \rho T \mathcal{R}/\mathcal{M}$  for ideal gas can be written in terms of state variables

$$p = (\gamma - 1)[E - \rho^{-1}\mathbf{M}^2/2]. \quad (3.12)$$

In general, the temperature  $T = T(\rho, e)$  can be inserted in any equation of state  $p = p(\rho, T)$  to find  $p = p(\mathbf{U})$ . Hence, solving Equation (3.8) for any fluid is possible. However, finding the function  $T = T(\rho, e)$  from  $e = e(\rho, T)$  can be complicated. Furthermore, the material equation may have severe influence on the properties of the solution  $\mathbf{U}(\mathbf{x}, t)$ . Therefore, only Equation (3.12) for ideal gas is considered.

### 3.2.4 Entropy Equation

The second law of thermodynamics can be used to select which solutions of the Equations (3.1), (3.2), (3.3) are physically possible. Basically it states, that the entropy  $s$ , defined by Gibbs fundamental thermodynamic equation

$$ds = \frac{1}{T} \left( de - \frac{p}{\rho^2} d\rho \right) \quad (3.13)$$

can not decrease in an isolated system, where isolated means that no mass flow and no energy flow passes the system boundaries. An expression similar to the right side of Equation (3.13) can also be obtained from Equations (3.1), (3.2), (3.3), assuming that all quantities are continuous and differentiable functions. Using the substantial derivative  $D/Dt = \partial/\partial t + \mathbf{u} \cdot \nabla$  and splitting the stress tensor  $\boldsymbol{\sigma} = -p\mathbf{I} + \mathbb{T}$  in a pressure term and a viscous stress tensor  $\mathbb{T}$ , the equations for mechanical energy and thermal energy

$$\rho \frac{D}{Dt} \frac{\|\mathbf{u}\|^2}{2} = -\nabla p \cdot \mathbf{u} + (\nabla \cdot \mathbb{T}) \cdot \mathbf{u} + \rho \mathbf{g} \cdot \mathbf{u}, \quad (3.14)$$

$$\rho \frac{De}{Dt} = \frac{p}{\rho} \frac{D\rho}{Dt} + \mathbb{T} : \nabla \mathbf{u} - \nabla \cdot \mathbf{q}, \quad (3.15)$$

can be obtained by multiplying Equation (3.2) with the dot-product of  $\mathbf{u}$ , and subtracting Equation (3.14) from Equation (3.3). In Equation (3.15)  $\nabla \cdot \mathbf{u} = -\rho^{-1} D\rho/Dt$

was inserted from Equation (3.1) and  $\mathbb{T} : \nabla \mathbf{u} = \nabla \cdot (\mathbb{T} \cdot \mathbf{u}) - (\nabla \cdot \mathbb{T}) \cdot \mathbf{u}$  was used for the dissipation. Hence, comparing Equation (3.15) with the right side of Equation (3.13) gives

$$\rho T \frac{Ds}{Dt} = \mathbb{T} : \nabla \mathbf{u} - \nabla \cdot \mathbf{q} . \quad (3.16)$$

This shows, that the substantial derivative of the entropy is zero, if the fluid is inviscid ( $\mathbb{T} = \mathbf{0}$ ) and the heat flux is zero. Flows, where  $s = \text{const}$  are said to be isentropic.

### 3.2.5 Isentropic Relations

For isentropic flow the pressure  $p = (\gamma - 1) \rho e$  for ideal gas from Equation (3.12) can be inserted in Equation (3.13) to find  $\frac{1}{e} de = (\gamma - 1) \frac{1}{\rho} d\rho$ . Since for a calorically ideal gas the temperature  $T = e/c_v$  is directly connected to the specific inner energy via the constant  $c_v$ , the solution for temperature and pressure

$$T/T_{\text{ref}} = (\rho/\rho_{\text{ref}})^{\gamma-1} , \quad (3.17)$$

$$p/p_{\text{ref}} = (\rho/\rho_{\text{ref}})^\gamma , \quad (3.18)$$

are quite simple. Usually, the values in the stagnation point are taken for  $\rho_{\text{ref}}$ ,  $p_{\text{ref}}$  and  $T_{\text{ref}}$ . However, the choice of reference values is completely free. Equations (3.17) and (3.18) are used for the boundary conditions of the valves, while solving the mass, momentum and energy equation inside the working chamber for inviscid fluid without heat flux automatically results in the isentropic relation for the thermodynamic variables, as long as the solution is continuous.

### 3.2.6 Sound Speed and Mach Number

For the flow inside a reciprocating compressor and the interaction with the valves it is extremely important how information is transported in the gas. Small pressure disturbances in materials propagate with the speed of sound

$$c = \sqrt{\left(\frac{\partial p}{\partial \rho}\right)_s} , \quad (3.19)$$

where the index  $s$  indicates, that this happens at constant entropy. If the disturbances are moderate, the propagation speed is slightly different to  $c$ , while it can differ enormously if the pressure disturbances are large. Hence, the speed  $c$  is a measure for the size of the domain effected by a weak disturbance in a point, in a certain time. As a consequence, the activity of a point in space and time effects the solution in other points in the so-called range of influence. On the other hand, the result of a single point is determined by the so-called domain of dependence. For an ideal gas, used for the reciprocating compressor model, the isentropic relations from Equations (3.17) and (3.18) can be used to find

$$c = \sqrt{\gamma \frac{p}{\rho}} , \quad (3.20)$$

where  $p/\rho = T\mathcal{R}/\mathcal{M}$  from the ideal gas equation emphasizes the dependence on the temperature  $T$ . Relating the modulus of the local flow velocity vector  $\mathbf{u}$  to the speed of sound, gives the dimensionless Mach number

$$Ma = \frac{\|\mathbf{u}\|}{c}. \quad (3.21)$$

The flow behavior is radically different for  $Ma < 1$  than for  $Ma > 1$ . Therefore,  $Ma = 1$  is called the critical Mach number.

### 3.2.7 Rankine-Hugoniot Conditions

In contrast to the continuous solutions, discontinuous solution can also be found for the Navier-Stokes and the Euler equations. The possibility, that some field quantities in a fluid may be discontinuous, was first remarked by Stokes [78], working on Challis's paradox [17]. Stokes expected an abrupt change of density and velocity, when passing across a surface of discontinuity. Stokes [78] proofed, that the existence of such a surface is possible, applying the jump conditions for mass and momentum for an inviscid compressible fluid. However, Stokes [78] did not consider a change of sound speed across the surface of discontinuity. According to Wilson [85],[86], Lord Rayleigh and also Sir W. Thomson pointed out in an correspondance with Stokes in the year 1848, that the conservation of energy would lead to a different result, if the flow is assumed to be reversible. Wilson [86] mentions in a historical review, that there was still an ongoing discussion about that question in the year 1880.

Riemann [69] published a paper on the propagation of sound waves of finite amplitude in the year 1860, deriving the jumps in mass and momentum for an isentropic (reversible) flow. Riemann [69] discussed the wave patterns for various initial conditions with jumps in density and velocity, nowadays referred to as the solutions of the Riemann problem. However, Riemann's assumption of isentropic behavior across a shock is not correct from the view of thermodynamics. The first correct consideration of thermodynamics and the relations to the wave-like propagations of a finite longitudinal disturbance was presented by Rankine [66] in the year 1870. Rankine [66] was the first to explain, that during the shock transition the particles "exchange heat" with each other, but that no heat is received from the outside. A theory on the propagation of motion in bodies based on characteristic curves for partial differential equations was published in 1887 by Hugoniot [34]. Note, that this paper discusses the motion of gases in the absence of discontinuities. The famous equation know as the Hugoniot-condition for the jump of energy appears in the second paper of Hugoniot [35], published in 1889.

The work of Hugoniot [34],[35] was the basis for the lecture propagation of waves, given by Hadamard [33] in the year 1903. Hadamard's lemma uses the concept of a singular surface. The exact definition of a singular surface is described e.g. in Truesdell and Toupin [84]. However, for convenience we give a stripped-down explanation: Consider an arbitrary chosen volume  $V$  and let  $\mathbf{x}$  be the position of point

inside  $V$ . The regular surface  $S$  divides the volume into two regions  $V^+$  and  $V^-$ . Let  $\Phi(\mathbf{x})$  be a function which is continuous and differentiable in both regions, though not at the surface  $S$ . From the regions  $V^+$  and  $V^-$  the function  $\Phi(\mathbf{x})$  approaches the two different limiting values  $\Phi^+$  and  $\Phi^-$  at the surface  $S$ . Following the notation of Christoffel [19], the jump in  $\Phi$  while crossing the surface  $S$  at the point  $\mathbf{x}$  is denoted by the symbol  $[[\Phi]] = \Phi^+ - \Phi^-$ . Since the function  $\Phi(\mathbf{x})$  at the surface  $S$  is not continuous, the surface  $S$  is considered to be a singular surface with respect to  $\Phi$ . The quantity  $[[\Phi]]$ , the so-called jump function, is a function of its position  $\mathbf{x}$  on  $S$ . A generalization of the jump conditions for a singular surface moving with velocity  $\dot{\mathbf{x}}$  has been derived by Kotchine [44]. Integrating Equations (3.1), (3.2), (3.3) over a moving domain and applying the integrals to each of the both sub-domains  $V^+$  and  $V^-$ , gives after some mathematical manipulation according to Kotchine [44] for every point on the singular surface moving with velocity  $\dot{\mathbf{x}}$

$$[[\rho(\mathbf{u} - \dot{\mathbf{x}}) \cdot \mathbf{n}]] = 0, \quad (3.22)$$

$$[[\rho \mathbf{u}(\mathbf{u} - \dot{\mathbf{x}}) \cdot \mathbf{n}]] = [[\boldsymbol{\sigma} \cdot \mathbf{n}]], \quad (3.23)$$

$$[[\rho(e + \frac{1}{2}|\mathbf{u}|^2)(\mathbf{u} - \dot{\mathbf{x}}) \cdot \mathbf{n}]] = [[(\boldsymbol{\sigma} \cdot \mathbf{u} - \mathbf{q}) \cdot \mathbf{n}]], \quad (3.24)$$

where  $[[\ ]]$  denotes the jump of the quantities inside the brackets, and  $\mathbf{n}$  is the unit normal vector of the singular surface. The jump conditions found by Rankine [66] and Hugoniot [34] are derived for a one-dimensional flow in direction of the singular surface normal. Using the state vector  $\mathbf{U}$  and the flux vector  $\mathbf{f}$  for an inviscid fluid without heat flux

$$\mathbf{U} = \begin{bmatrix} \rho \\ \rho u \\ \rho e + \rho u^2/2 \end{bmatrix}, \quad \mathbf{f} = \begin{bmatrix} \rho u \\ \rho u^2 + p \\ u(\rho e + \rho u^2/2 + p) \end{bmatrix}, \quad (3.25)$$

the Rankine-Hugoniot conditions can be written in compact form

$$[[\mathbf{f}]] = \sigma [[\mathbf{U}]], \quad (3.26)$$

where  $[[\mathbf{U}]] = \mathbf{U}_2 - \mathbf{U}_1$  and  $[[\mathbf{f}]] = \mathbf{f}_2 - \mathbf{f}_1$  are the jumps of the state vector and the flux vector built with values on side 1 and side 2 of the discontinuity, and  $\sigma = \dot{\mathbf{x}} \cdot \mathbf{n}$  is the surface normal speed. With the pressure  $p = (\gamma - 1)\rho e$  for ideal gas, the Rankine-Hugoniot conditions form the system

$$\rho_2 u_2 - \rho_1 u_1 = \sigma(\rho_2 - \rho_1), \quad (3.27)$$

$$\rho_2 u_2^2 - \rho_1 u_1^2 + p_2 - p_1 = \sigma(\rho_2 u_2 - \rho_1 u_1), \quad (3.28)$$

$$\frac{1}{2}(\rho_2 u_2^3 - \rho_1 u_1^3) + \frac{\gamma}{\gamma - 1}(u_2 p_2 - u_1 p_1) = \sigma \left[ \frac{1}{2}(\rho_2 u_2^2 - \rho_1 u_1^2) + \frac{1}{\gamma - 1}(p_2 - p_1) \right]. \quad (3.29)$$

Assuming  $\rho_1, u_1, p_1$  are given, the conditions determine how  $u_2, \rho_2, \sigma$  depend on  $p_2$ . In section 6.6.2 this form of the Rankine-Hugoniot conditions is used to determine numerical boundary conditions for discharge valves. Two different types of discontinuities can be observed, contact discontinuities and shocks.

### 3.2.7.1 Contact Discontinuity

The contact discontinuity is obtained, when the singular surface moves with the speed of the fluid in normal direction  $\sigma = u_1$ . Then, Equation (3.27) shows  $u_2 = u_1$  and Equation (3.28) gives  $p_2 = p_1$ . However, Equation (3.29) is fulfilled automatically, and does not determine  $\rho_2$ . Any choice  $\rho_2 \neq \rho_1$  or  $\rho_2 = \rho_1$  is a solution to the system of equations. Therefore, the solution for a contact discontinuity,

$$\sigma = u_1, \quad u_2 = u_1, \quad p_2 = p_1, \quad (3.30)$$

shows, that the jump of the normal velocity  $\llbracket u \rrbracket$  and the jump of the pressure  $\llbracket p \rrbracket$  are zero across a discontinuity surface being part of domains  $V_1$  and  $V_2$ . Hence, in the sense of Hadamard [33], for  $\rho_2 \neq \rho_1$  the discontinuity surface normal to the motion of the fluid is said to be singular with respect to the density  $\rho$ .

### 3.2.7.2 Shock Discontinuity

In contrast to the contact discontinuity, the shock discontinuity is found for  $\sigma \neq u_1$ . The speed of the discontinuity  $\sigma = (\rho_2 u_2 - \rho_1 u_1)/(\rho_2 - \rho_1)$  derived from Equation (3.27) can be inserted in Equation (3.28) to find for the density behind the shock

$$\rho_2 = \frac{1}{1 - \frac{\rho_1(u_2 - u_1)^2}{p_2 - p_1}} \rho_1, \quad (3.31)$$

where  $u_2$  is still unknown. However, plugging  $\sigma$  and  $\rho_2$  in Equation (3.29) gives the equation  $2(p_2 - p_1)^2 - \rho_1[(\gamma - 1)p_1 + (\gamma + 1)p_2](u_2 - u_1)^2 = 0$  with shock solutions

$$u_2 = u_1 \mp (p_2 - p_1) \sqrt{\frac{2}{\rho_1[(\gamma - 1)p_1 + (\gamma + 1)p_2]}}, \quad (3.32)$$

and the solution of the constact discontinuity  $u_2 = u_1$ , that was discussed already. With Equation (3.20) the speed of sound  $c_1 = \sqrt{\gamma p_1/\rho_1}$  for ideal gas can be used to substitute the density  $\rho_1$  in Equation (3.32)

$$u_2 = u_1 \mp c_1 \frac{p_2/p_1 - 1}{\sqrt{\frac{\gamma}{2}(\gamma - 1) + \frac{\gamma}{2}(\gamma + 1)p_2/p_1}}. \quad (3.33)$$

This form will be used in Equation (6.13) to determine the numerical boundary conditions of suction valves.

## 3.3 Boundary Conditions for Fluid Flow

For the reciprocating compressor working chamber model the following two distinct boundary conditions are used on the surface of the domain:

- Walls,
- Valves



The walls can be either moving, e.g. the piston, or non-moving. The boundary type wall is also used for the valve boundary condition, when the valve plate lift  $x_V$  is zero. For zero lift, the plate blocks the passage for the flow, and no exchange of mass or energy can occur from the working chambers to the valve retainers outside the modeled domain. Hence, this is in fact the same boundary conditions as a non-moving wall. On the other hand, for  $x_V > 0$  mass and energy can pass the slots of the valves, and a sophisticated model has to be applied to find physically correct mass, momentum and energy flow boundary conditions.

### 3.3.1 Walls

As already discussed, the Euler equations require to allow a velocity slip in tangential direction along the walls. However, in order to guarantee that no mass and energy flows through the wall, the impermeable wall condition

$$(\mathbf{u} - \dot{\mathbf{x}}) \cdot \mathbf{n} = 0 \quad (3.34)$$

has to be applied, where  $\mathbf{u}$  is the fluid velocity at the wall, and  $\dot{\mathbf{x}}$  is the velocity vector of the wall motion. The dot-product with the unit normal vector of the wall  $\mathbf{n}$  leads to a vanishing component of the relative velocity in wall normal direction. The only moving boundary zone in the model is the piston, with a motion  $\dot{\mathbf{x}} = [0, 0, \dot{\varphi} \frac{d}{d\varphi} z_P(\varphi)]^\top$  only in  $z$ -direction. For non-moving walls  $\dot{\mathbf{x}} = \mathbf{0}$ , Equation (3.34) automatically fulfills the simpler condition  $\mathbf{u} \cdot \mathbf{n} = 0$ .

### 3.3.2 Valves

The flow through the valves is not resolved in all its three-dimensional details, as this is done, e.g. by Flade [29]. However, for the flow computation of the reciprocating compressor, it is important to know how much massflow and energy-flow passes the valves, when the valve plate opens a passage for the flow. Equation (2.6) provides the empirical formula for the passage area  $\phi(x_V)$ , depending on the valve plate lift  $x_V$ . As shown in Figure 3.1 for a suction valve and a discharge valve, the valves are modeled using locally the flow trough a nozzle hole with effective cross section  $\phi_2$ , computed with the valve-lift dependend function  $\phi(x_V)$ .

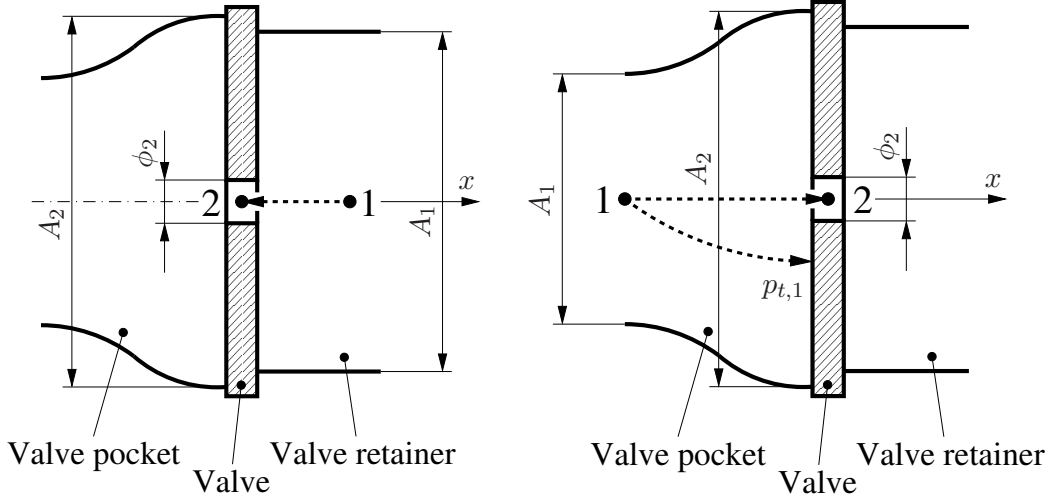


Figure 3.1: Flow model for suction valve (left) and discharge valve (right)

Isentropic flow from point 1 into the nozzle (point 2) is assumed. For an ideal gas with constant specific heat capacities  $c_p$ ,  $c_v$  and isentropic coefficient  $\gamma = c_p/c_v$ , the stagnation (or total) pressure  $p_{t,1}$  is obtained using the (steady) energy equation for the stagnation (or total) temperature  $T_{t,1} = T_1 + \frac{1}{2}u_1^2/c_p$

$$\frac{p_{t,1}}{p_1} = \left(\frac{T_{t,1}}{T_1}\right)^{\frac{\gamma}{\gamma-1}} = \left(1 + \frac{1}{2} \frac{u_1^2}{c_p T_1}\right)^{\frac{\gamma}{\gamma-1}} = \left(1 + \frac{\gamma-1}{2} Ma_1^2\right)^{\frac{\gamma}{\gamma-1}}, \quad (3.35)$$

where  $\rho_1$ ,  $u_1$ ,  $p_1$ ,  $Ma_1 = u_1/\sqrt{\gamma p_1/\rho_1}$  are density, flow velocity, pressure and Mach number in point 1, respectively. With the density  $\rho_2$  and the flow velocity  $u_2$

$$\rho_2 = \rho_1 \left(\frac{p_2}{p_1}\right)^{1/\gamma}, \quad |u_2| = \sqrt{u_1^2 + \frac{2\gamma}{\gamma-1} \left(\frac{p_1}{\rho_1} - \frac{p_2}{\rho_2}\right)}, \quad (3.36)$$

the mass flow through the valve

$$|\dot{m}_2| = \phi_2 \rho_2 |u_2| = \phi_2 \rho_1 \left(\frac{p_2}{p_1}\right)^{1/\gamma} \sqrt{u_1^2 + \frac{2\gamma}{\gamma-1} \frac{p_1}{\rho_1} \left[1 - \left(\frac{p_2}{p_1}\right)^{1-1/\gamma}\right]} \quad (3.37)$$

depends on  $\rho_1$ ,  $u_1$ ,  $p_1$  and the pressure  $p_2$  behind the valve. If the suction valve retainer is not modeled and the flow comes from a very large suction chamber with negligible flow velocity, the given suction values  $\rho_1 = \rho_s$ ,  $u_1 = 0$ ,  $p_1 = p_s$  are used. If the discharge valve retainer is not modelled the pressure is taken from the discharge chamber  $p_2 = p_d$ .

## 3.4 The Idealized Compressor Process

### 3.4.1 Pressure over Volume and Crank Angle

In order to make the 3d-simulation results comparable, the idealized compressor process can be used. Due to the motion of the piston  $z_P(\varphi)$  given in Equation (1.1), the volume in the working chamber  $V(\varphi)$  changes between  $V_{min}$  and  $V_{max}$ , where

$$V_{max} = V_{min} + \frac{\pi}{4}(d_P^2 - d_R^2) 2r \quad (3.38)$$

is equal to  $V(\pi)$  from Equation (1.2). Figure 3.2 shows the pressure-volume diagram for the idealized compressor cycle operating between suction pressure  $p_s$  and discharge pressure  $p_d$ . The process runs counter-clockwise following the points 1, 2, 3, 4 and consists of the four phases suction, compression, discharge and expansion.

The term idealized is used, because during suction and discharge, where the suction and the discharge valves are open, there is no pressure difference to the suction pressure  $p_s$  and the discharge pressure  $p_d$ , and the compression and expansion lines follow isentropic curves. Hence, the idealized compressor process neglects valve losses and assumes adiabatic walls surrounding an inviscid gas. The idealized compressor process can be used as a reference process for the comparison with the 3d CFD-simulation results.

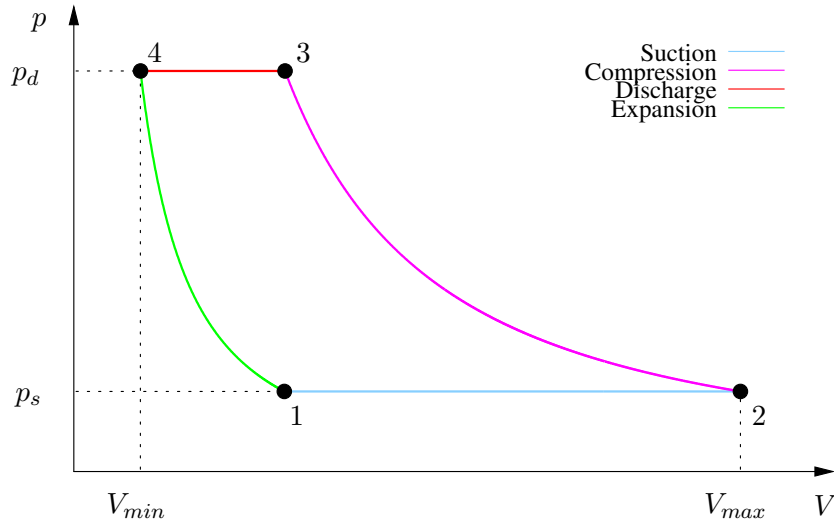


Figure 3.2:  $p$ - $V$  diagram of the idealized compressor cycle

In order to show how the pressure  $p$  of the idealized compressor process depends on the crank-angle  $\varphi$ , it is favourable to express all terms in dimensionless quantities. Using the ratios

$$\lambda = \frac{r}{L}, \quad \varepsilon = \frac{V_{min}}{V_{max} - V_{min}}, \quad \psi = \frac{p_d}{p_s}, \quad \gamma = \frac{c_p}{c_v}, \quad (3.39)$$

it is possible to completely describe the pressure of the idealized process as a function of the crank angle  $\varphi$

$$\frac{p}{p_s} = \begin{cases} \psi \left( \frac{\varepsilon}{\varepsilon + 0.5 z_P(\varphi)/r} \right)^\gamma & : 0 \leq \varphi < \varphi_s \\ 1 & : \varphi_s \leq \varphi < \pi \\ \left( \frac{\varepsilon + 1}{\varepsilon + 0.5 z_P(\varphi)/r} \right)^\gamma & : \pi \leq \varphi < \varphi_d \\ \psi & : \varphi_d \leq \varphi < 2\pi \end{cases}, \quad (3.40)$$

$$z_P(\varphi)/r = 1 - \cos \varphi + \lambda^{-1} - \sqrt{\lambda^{-2} - \sin^2 \varphi}, \quad (3.41)$$

$$\varphi_s = \arccos \left[ \frac{1 (1 + \lambda^{-1} - 2\varepsilon(\psi^{1/\gamma} - 1))^2 + 1 - \lambda^{-2}}{2 (1 + \lambda^{-1} - 2\varepsilon(\psi^{1/\gamma} - 1))} \right], \quad (3.42)$$

$$\varphi_d = 2\pi - \arccos \left[ \frac{1 (1 + \lambda^{-1} - 2(\varepsilon + 1)\psi^{-1/\gamma} + 2\varepsilon)^2 + 1 - \lambda^{-2}}{2 (1 + \lambda^{-1} - 2(\varepsilon + 1)\psi^{-1/\gamma} + 2\varepsilon)} \right], \quad (3.43)$$

where  $z_P(\varphi)/r$  can be derived for Equation (1.1), the crank angle positions  $\varphi_s$  and  $\varphi_d$  indicate the beginning of suction and discharge, respectively. Figure 3.3 shows the pressure over the crank angle for the example  $\lambda = 0.3$ ,  $\varepsilon = 0.1$ ,  $\psi = 5$ ,  $\gamma = 1.4$ . The curves for density and temperature can then be obtained easily using the isentropic relations.

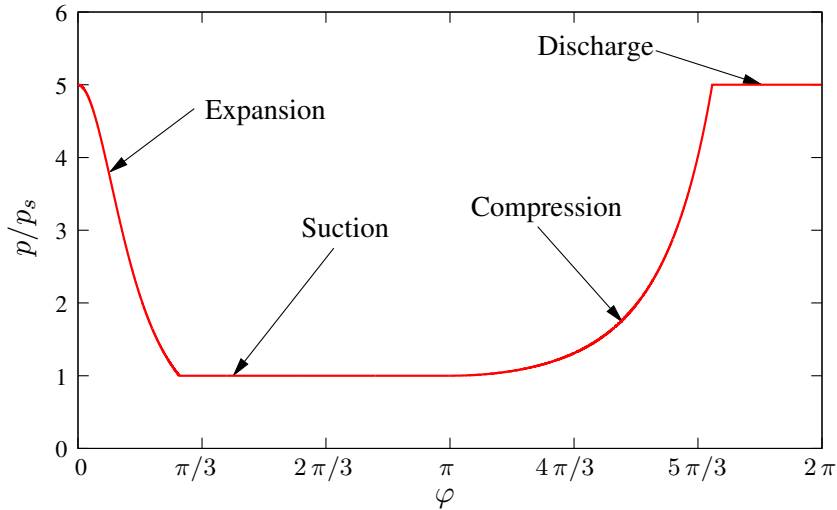


Figure 3.3: Relative pressure curve over crank angle

### 3.4.2 Instantaneous Mass Flow and Driving Power

With  $\rho(\varphi) = \rho_s (p(\varphi)/p_s)^{1/\gamma}$  the density curve over crank angle  $\varphi$  can be computed using Equation (3.40). For the idealized compressor process, the density and the pressure are assumed to be constant during suction and discharge. Assuming, that the Mach number in the whole working chamber is small, the flow can be considered

to be almost incompressible. However, this assumptions may be heavily violated by a practical application, but for the idealized process, it allows to compute the massflow passing the valves, using the massflow generated by the motion of the piston

$$\dot{m}(\varphi) = \frac{\pi}{4}(d_P^2 - d_R^2) \rho(\varphi) \dot{\varphi} \frac{d}{d\varphi} z_P(\varphi). \quad (3.44)$$

During compression and expansion  $\dot{m}(\varphi) = 0$ , because the idealized model assumes closed valves. The instantaneous driving power  $\dot{W}$  of the compressor is the product of piston force and piston velocity. Assuming the pressure inside the working chamber is only a function of crank angle, this reads

$$\dot{W}(\varphi) = \frac{\pi}{4}(d_P^2 - d_R^2) p(\varphi) \dot{\varphi} \frac{d}{d\varphi} z_P(\varphi). \quad (3.45)$$

Equation (3.45) is valid for all values of the crank angle  $\varphi$ .

### 3.4.3 Average Mass Flow and Driving Power

The difference between the mass inside the cylinder during compression  $m_c = (\mathcal{M} p_s V_{max})/(\mathcal{R} T_s)$  and expansion  $m_e = (\mathcal{M} p_d V_{min})/(\mathcal{R} T_d)$  is transported through the valves, while the crank shaft makes one rotation. So the average mass flux  $\bar{m}$  over a compressor cycle can be defined as

$$\bar{m} = \frac{m_c - m_e}{2\pi/\dot{\varphi}} = \frac{\dot{\varphi}}{2\pi} \underbrace{\frac{\mathcal{M} p_s}{\mathcal{R} T_s}}_{\rho_s} (V_{max} - V_{min}) \left[ 1 - \varepsilon \left( \psi^{\frac{1}{\gamma}} - 1 \right) \right]. \quad (3.46)$$

The compressor changes the state of the gas from  $(p_s, T_s)$  to  $(p_d, T_d)$ . If no heat flows over the walls the specific work

$$w = h_d - h_s = c_p (T_d - T_s) = c_p T_s \left( \psi^{\frac{\gamma-1}{\gamma}} - 1 \right) \quad (3.47)$$

needed, is equal to the difference in the specific enthalpies at suction and discharge, if the kinetic energy can be neglected. The time-averaged driving power then becomes

$$\bar{W} = \bar{m} w = \frac{\dot{\varphi}}{2\pi} \frac{\gamma}{\gamma - 1} p_s (V_{max} - V_{min}) \left( \psi^{\frac{\gamma-1}{\gamma}} - 1 \right) \left[ 1 - \varepsilon \left( \psi^{\frac{1}{\gamma}} - 1 \right) \right]. \quad (3.48)$$

## 3.5 Estimates for Solid Body Motion

Although the focus of this thesis is on the description of the fluid motion in the working chamber and the thermodynamics of a reciprocating compressor, a detailed understanding of the solid body motion and of the forces acting on compressor parts is usually of more importance for the layout and design of such machines.

One aspect is the permanent acceleration and deceleration of the piston due to the back and forth going linear motion. Some estimates show, that the averaged piston velocity  $\bar{v}_P$  from Equation (1.3) is an important measure for the solid parts, as well as it is for the motion of the gas inside the working chamber of the compressor. Geometrically similar machines with a characteristic length scale  $r$ , that run with the same mean piston speed  $\bar{v}_P$  are said to be mechanically similar, if the gas pressure  $p$  acting on the piston is the same, and the parts are made of materials having the same density  $\rho_{solid}$ . The mechanical stresses  $\sigma_{solid}$ , say in the piston of a reciprocating machine, are caused by the gas pressure  $p$  on the one hand, and by forces due to the acceleration ( $\sim \bar{v}_P^2/r$ ) of the piston mass ( $\sim \rho_{solid} r^3$ ) divided by cross section area ( $\sim r^2$ ) on the other hand. The ratio of the estimate for the stresses caused by mass acceleration ( $\rho_{solid} r^3$ )  $\cdot (\bar{v}_P^2/r)$   $\cdot (1/r^2)$  and the stresses caused by the gas pressure ( $\sim p_{max}$ ) is a Cauchy number

$$Ca = \frac{\rho_{solid} \bar{v}_P^2}{p_{max}}, \quad (3.49)$$

where  $p_{max}$  is used instead of a Young's modulus  $E$  in the usual Cauchy number definition for solid bodies. The pressure  $p_{max}$  and the mean piston speed  $\bar{v}_P$  appear as an operating condition for a built machine with density  $\rho_{solid}$ . Hence, reciprocating compressors with the same Cauchy number are mechanically equivalent, independent of  $r$  or any other measure for the compressor size. For the fluid the piston velocity appears as a moving boundary condition.

# Chapter 4

## Properties of Partial Differential Equations

### 4.1 Introduction to PDEs

In this chapter some relevant mathematical properties of the partial differential equations (PDEs) describing the physics of the flow inside a reciprocating compressor are discussed. In the present work a numerical method is used to solve the Euler equations approximately, that uses properties of the exact equations. For the three-dimensional Roe solver presented in section 6, the rotational invariance and the hyperbolicity of the linearized Euler equations are crucial properties. For hyperbolic PDEs a diagonalization of the system is possible, allowing a decomposition in decoupled waves. These properties build the basis for the first order accurate upwind approximation of the Roe method for locally linearized system of PDEs. However, the first order accuracy of the Roe scheme leads to a phenomenon called numerical diffusion. The numerical diffusion appearing in the approximate solutions of advection problems solved with first order upwind methods, shows a behavior similar to real physical diffusion processes. In order to demonstrate this effect, the wave solution of the linear advection-diffusion equation is presented, and the consequences on the change of the so-called total variation (TV) is shown. The results plotted in Figure 5.2 for a one-dimensional situation indicate, that numerical methods that consider the property of non-increasing TV of the underlying PDE (so called TVD-schemes) can dramatically improve the results for continuous and discontinuous solutions compared to the first order upwind method. Since the non-increasing TV of PDEs in the three-dimensional case is much more complex, these aspects will not be discussed in detail.

### 4.2 System of Non-Linear PDEs

A system of  $n$  non-linear partial differential equations (PDEs) including a first time-derivative  $\partial/\partial t$  and all the first space derivatives  $\partial/\partial x$ ,  $\partial/\partial y$ ,  $\partial/\partial z$  may be written

in the following vector notation form

$$\frac{\partial \mathbf{U}}{\partial t} + \frac{\partial \mathbf{f}^{(x)}}{\partial x} + \frac{\partial \mathbf{f}^{(y)}}{\partial y} + \frac{\partial \mathbf{f}^{(z)}}{\partial z} = \mathbf{0}, \quad (4.1)$$

where  $\mathbf{U} = [U_1, \dots, U_n]^\top$  is the vector of  $n$  state variables  $U_1, \dots, U_n$  depending on time  $t$  and space  $\mathbf{x} = [x, y, z]^\top$ . The space components  $x, y, z$  usually form a cartesian coordinate system. The flux functions in the directions of the coordinate system are  $\mathbf{f}^{(x)} = [f_1^{(x)}, \dots, f_n^{(x)}]^\top$ ,  $\mathbf{f}^{(y)} = [f_1^{(y)}, \dots, f_n^{(y)}]^\top$  and  $\mathbf{f}^{(z)} = [f_1^{(z)}, \dots, f_n^{(z)}]^\top$ . Combining the flux functions in a single matrix  $\hat{\mathbf{f}} = [\mathbf{f}^{(x)}, \mathbf{f}^{(y)}, \mathbf{f}^{(z)}]$  allows to write the system of PDEs in so-called divergence form

$$\frac{\partial \mathbf{U}}{\partial t} + \nabla \cdot \hat{\mathbf{f}} = \mathbf{0}, \quad (4.2)$$

where the vector notation  $\nabla = [\partial/\partial x, \partial/\partial y, \partial/\partial z]^\top$  is used for the divergence operator. If the PDE represents a physical model that describes the advection of the state vector quantities without the presence of diffusion, the combined matrix of flux functions  $\hat{\mathbf{f}} = \hat{\mathbf{f}}(\mathbf{U})$  only depends on the components of the state vector  $\mathbf{U}$ . If the physical model describes a process of advection and diffusion of the state vector quantities, the flux function matrix  $\hat{\mathbf{f}} = \hat{\mathbf{f}}(\mathbf{U}, \nabla \mathbf{U})$  depends on the state vector  $\mathbf{U}$  and its gradient  $\nabla \mathbf{U}$ . As a consequence of diffusion, the divergence of the flux function matrix  $\nabla \cdot \hat{\mathbf{f}}$  leads to second derivatives in space for advection-diffusion models, while only first derivatives in space appear in  $\nabla \cdot \hat{\mathbf{f}}$  for a pure advection model equation. This has severe consequences on the properties of the PDE-solutions and on the required boundary conditions. The presence of diffusion leads to an instant spread of information from a point in space over the whole domain, while in the absence of diffusion, the advection determines the propagation speed of information.

### 4.2.1 Rotational Invariance

If Equation (4.2) is integrated over a non-moving control volume

$$\frac{d}{dt} \int_V \mathbf{U} dV + \oint_S \hat{\mathbf{f}} \cdot \mathbf{n} dS = \mathbf{0}, \quad (4.3)$$

the integrand in the surface integral can be written as

$$\hat{\mathbf{f}} \cdot \mathbf{n} = n^{(x)} \mathbf{f}^{(x)} + n^{(y)} \mathbf{f}^{(y)} + n^{(z)} \mathbf{f}^{(z)}, \quad (4.4)$$

where  $n^{(x)}$ ,  $n^{(y)}$ ,  $n^{(z)}$  are the components of the outward unit vector  $\mathbf{n}$  normal to the surface. The local properties of the product  $\hat{\mathbf{f}} \cdot \mathbf{n}$  on the surface element  $dS$  of the domain are important for some classifications of the partial differential equation. As shown in Toro [81], the Euler equations are rotational invariant. Using a spherical coordinate system for the surface normal vector  $\mathbf{n}$ , and a rotation matrix



$\mathbf{T}$  applicable to vectors  $\mathbf{f}^{(x)}$ ,  $\mathbf{f}^{(y)}$ ,  $\mathbf{f}^{(z)}$  with five rows

$$\mathbf{n} = \begin{bmatrix} n^{(x)} \\ n^{(y)} \\ n^{(z)} \end{bmatrix} = \begin{bmatrix} \cos \theta^{(y)} \cos \theta^{(z)} \\ \cos \theta^{(y)} \sin \theta^{(z)} \\ \sin \theta^{(z)} \end{bmatrix}, \quad (4.5)$$

$$\mathbf{T} = \begin{bmatrix} 1 & 0 & 0 & 0 & 0 \\ 0 & \cos \theta^{(y)} \cos \theta^{(z)} & \cos \theta^{(y)} \sin \theta^{(z)} & \sin \theta^{(y)} & 0 \\ 0 & -\sin \theta^{(z)} & \cos \theta^{(z)} & 0 & 0 \\ 0 & -\sin \theta^{(y)} \cos \theta^{(z)} & -\sin \theta^{(y)} \sin \theta^{(z)} & \cos \theta^{(y)} & 0 \\ 0 & 0 & 0 & 0 & 1 \end{bmatrix}, \quad (4.6)$$

the identity

$$\cos \theta^{(y)} \cos \theta^{(z)} \mathbf{f}^{(x)}(\mathbf{U}) + \cos \theta^{(y)} \sin \theta^{(z)} \mathbf{f}^{(y)}(\mathbf{U}) + \sin \theta^{(z)} \mathbf{f}^{(x)}(\mathbf{U}) = \mathbf{T}^{-1} \mathbf{f}^{(x)}(\mathbf{T}\mathbf{U}) \quad (4.7)$$

proves the rotational invariance of the PDE system. Hence, if Equation (4.7) is fulfilled, only the component  $\mathbf{f}^{(x)}$  is required to compute the flux in the direction of the surface normal.

## 4.2.2 Local Linearization

In general, the advective flux functions  $\mathbf{f}^{(x)}(\mathbf{U})$ ,  $\mathbf{f}^{(y)}(\mathbf{U})$ ,  $\mathbf{f}^{(z)}(\mathbf{U})$  depend non-linearly on the state vector  $\mathbf{U}$ . However, linear equations are locally good approximations to the non-linear equations, and help to understand how the solution evolves with respect to time in the very near future. Based on the Jacobi matrices of the flux functions

$$\mathbf{A}^{(x)}(\mathbf{U}) = \frac{\partial}{\partial \mathbf{U}} \mathbf{f}^{(x)}(\mathbf{U}), \quad (4.8)$$

$$\mathbf{A}^{(y)}(\mathbf{U}) = \frac{\partial}{\partial \mathbf{U}} \mathbf{f}^{(y)}(\mathbf{U}), \quad (4.9)$$

$$\mathbf{A}^{(z)}(\mathbf{U}) = \frac{\partial}{\partial \mathbf{U}} \mathbf{f}^{(z)}(\mathbf{U}), \quad (4.10)$$

see e.g. Hirsch [38] and [39], Equation (4.1) can be written as

$$\frac{\partial \mathbf{U}}{\partial t} + \mathbf{A}^{(x)}(\mathbf{U}) \frac{\partial \mathbf{U}}{\partial x} + \mathbf{A}^{(y)}(\mathbf{U}) \frac{\partial \mathbf{U}}{\partial y} + \mathbf{A}^{(z)}(\mathbf{U}) \frac{\partial \mathbf{U}}{\partial z} = \mathbf{0}. \quad (4.11)$$

This is still a non-linear set of equations, because the Jacobi matrices also depend on the state vector  $\mathbf{U}$ . However, if the Jacobi matrices are frozen by a constant state vector  $\bar{\mathbf{U}}$ , the equation

$$\frac{\partial \mathbf{U}}{\partial t} + \mathbf{A}^{(x)}(\bar{\mathbf{U}}) \frac{\partial \mathbf{U}}{\partial x} + \mathbf{A}^{(y)}(\bar{\mathbf{U}}) \frac{\partial \mathbf{U}}{\partial y} + \mathbf{A}^{(z)}(\bar{\mathbf{U}}) \frac{\partial \mathbf{U}}{\partial z} = \mathbf{0} \quad (4.12)$$

becomes linear. Finding the solutions of linear systems of partial differential equations can be accomplished applying a wave ansatz to the equations. An important requirement to solve the equations with this ansatz, is the hyperbolicity of the equation system. In the hyperbolic case, the time evolution of the initial function can be predicted by the decomposition into single waves.

### 4.2.3 Hyperbolicity

According to Leveque [51] and Toro [81], a system of PDEs shown in Equation (4.1) is hyperbolic in time, if the matrix

$$\mathbf{A}(\mathbf{U}, \mathbf{n}) = n^{(x)} \mathbf{A}^{(x)}(\mathbf{U}) + n^{(y)} \mathbf{A}^{(y)}(\mathbf{U}) + n^{(z)} \mathbf{A}^{(z)}(\mathbf{U}) \quad (4.13)$$

is diagonalizable for all choices of the unit normal vector  $\mathbf{n} = [n^{(x)}, n^{(y)}, n^{(z)}]^\top$ . The vector  $\mathbf{n}$  shows the direction of a plane wave solution to the Equation (4.1). A diagonalizable matrix  $\mathbf{A}(\mathbf{U}, \mathbf{n})$  has only real eigenvalues. If all real eigenvalues of  $\mathbf{A}(\mathbf{U}, \mathbf{n})$  are distinct, the system given by Equation (4.1) is said to be strictly hyperbolic. However, for the three-dimensional Euler equations, this is not the case, while the one-dimensional Euler equations  $\mathbf{U}_t + \mathbf{f}_x = \mathbf{0}$  using the state and flux vector of Equation (3.25) are strictly hyperbolic.

## 4.3 System of Linear PDEs

In order to demonstrate the advantages of linear partial differential equation systems, the properties of a hyperbolic problem

$$\mathbf{U}_t + \mathbf{A}(\bar{\mathbf{U}}) \mathbf{U}_x = \mathbf{0} \quad (4.14)$$

are briefly discussed. Similar examples are found in Leveque [50] and Hirsch [38], [39]. For simplicity, only a state vector  $\mathbf{U} = [U_1, U_2]^\top$  containing two components  $U_1$  and  $U_2$  is used, giving a  $(2 \times 2)$  matrix  $\mathbf{A}(\bar{\mathbf{U}})$  with four constant entities  $A_{11}$ ,  $A_{12}$ ,  $A_{21}$ ,  $A_{22}$  determined by the choice of  $\bar{\mathbf{U}} = [\bar{U}_1, \bar{U}_2]^\top$ .

### 4.3.1 Eigenvalues and Eigenvectors

The eigenvalues  $\lambda^{(1)}$ ,  $\lambda^{(2)}$  and eigenvectors  $\mathbf{r}^{(1)}$ ,  $\mathbf{r}^{(2)}$  of a  $(2 \times 2)$  matrix  $\mathbf{A}$  can be found using  $\mathbf{A} \cdot \mathbf{r}^{(1)} = \lambda^{(1)} \mathbf{r}^{(1)}$  and  $\mathbf{A} \cdot \mathbf{r}^{(2)} = \lambda^{(2)} \mathbf{r}^{(2)}$

$$\underbrace{\begin{bmatrix} A_{11} & A_{12} \\ A_{21} & A_{22} \end{bmatrix}}_{\mathbf{A}} \cdot \underbrace{\begin{bmatrix} r_1^{(1)} \\ r_2^{(1)} \end{bmatrix}}_{\mathbf{r}^{(1)}} = \lambda^{(1)} \underbrace{\begin{bmatrix} r_1^{(1)} \\ r_2^{(1)} \end{bmatrix}}_{\mathbf{r}^{(1)}}, \quad \underbrace{\begin{bmatrix} A_{11} & A_{12} \\ A_{21} & A_{22} \end{bmatrix}}_{\mathbf{A}} \cdot \underbrace{\begin{bmatrix} r_1^{(2)} \\ r_2^{(2)} \end{bmatrix}}_{\mathbf{r}^{(2)}} = \lambda^{(2)} \underbrace{\begin{bmatrix} r_1^{(2)} \\ r_2^{(2)} \end{bmatrix}}_{\mathbf{r}^{(2)}}. \quad (4.15)$$

Collecting the eigenvalues in the diagonal matrix  $\mathbf{\Lambda} = \text{diag}[\lambda^{(1)}, \lambda^{(2)}]$  and the eigenvectors in the matrix  $\mathbf{R} = [\mathbf{r}^{(1)}, \mathbf{r}^{(2)}]$ , one matrix equation can be formed

$$\underbrace{\begin{bmatrix} A_{11} & A_{12} \\ A_{21} & A_{22} \end{bmatrix}}_{\mathbf{A}} \cdot \underbrace{\begin{bmatrix} r_1^{(1)} & r_1^{(2)} \\ r_2^{(1)} & r_2^{(2)} \end{bmatrix}}_{\mathbf{R}} = \underbrace{\begin{bmatrix} r_1^{(1)} & r_1^{(2)} \\ r_2^{(1)} & r_2^{(2)} \end{bmatrix}}_{\mathbf{R}} \cdot \underbrace{\begin{bmatrix} \lambda^{(1)} & 0 \\ 0 & \lambda^{(2)} \end{bmatrix}}_{\mathbf{\Lambda}}, \quad (4.16)$$

where the matrix  $\mathbf{A} = \mathbf{R} \mathbf{\Lambda} \mathbf{R}^{-1}$  is said to be written in diagonal form.

### 4.3.2 Diagonalization and Wave Decomposition

The diagonalization of  $\mathbf{A}$  can be used to decouple the system of linear hyperbolic equations into equations for the vector of characteristic variables  $\mathbf{v} = [v_1, v_2]^\top$

$$\mathbf{U}_t + \mathbf{A}\mathbf{U}_x = \mathbf{0}, \quad (4.17)$$

$$\underbrace{\mathbf{R}^{-1}\mathbf{U}_t}_{\mathbf{v}_t} + \mathbf{R}^{-1}\mathbf{R}\mathbf{\Lambda}\mathbf{R}^{-1}\underbrace{\mathbf{U}_x}_{\mathbf{v}_x} = \mathbf{0}, \quad (4.18)$$

$$\begin{bmatrix} v_1 \\ v_2 \end{bmatrix}_t + \begin{bmatrix} \lambda^{(1)} & 0 \\ 0 & \lambda^{(2)} \end{bmatrix} \cdot \begin{bmatrix} v_1 \\ v_2 \end{bmatrix}_x = \begin{bmatrix} 0 \\ 0 \end{bmatrix}, \quad (4.19)$$

with the solutions  $v_1(x, t) = v_1(x - \lambda^{(1)}t)$ ,  $v_2(x, t) = v_2(x - \lambda^{(2)}t)$ . Taking  $\xi = x - \lambda^{(1)}t$  the proof is simple  $v_{1,t} + \lambda^{(1)}v_{1,x} = v_{1,\xi}\xi_t + \lambda^{(1)}v_{1,\xi}\xi_x = -v_{1,\xi}\lambda^{(1)} + \lambda^{(1)}v_{1,\xi} = 0$ . The final solution

$$\mathbf{U}(x, t) = \mathbf{R}\mathbf{v} = \begin{bmatrix} r_1^{(1)} & r_1^{(2)} \\ r_2^{(1)} & r_2^{(2)} \end{bmatrix} \cdot \begin{bmatrix} v_1 \\ v_2 \end{bmatrix} = \begin{bmatrix} v_1 r_1^{(1)} + v_2 r_1^{(2)} \\ v_1 r_2^{(1)} + v_2 r_2^{(2)} \end{bmatrix} = v_1(x - \lambda^{(1)}t) \mathbf{r}^{(1)} + v_2(x - \lambda^{(2)}t) \mathbf{r}^{(2)} \quad (4.20)$$

has to be fitted to the initial conditions, determining  $v_1(x, 0)$  and  $v_2(x, 0)$ .

## 4.4 Linear Scalar Advection-Diffusion Equation

### 4.4.1 Wave Solutions

A simple model equation for transport phenomena in one space dimension is the linear advection-diffusion equation for the evolution of a space and time-dependent scalar  $u = u(x, t)$

$$\frac{\partial}{\partial t}u(x, t) + a\frac{\partial}{\partial x}u(x, t) = d\frac{\partial^2}{\partial x^2}u(x, t), \quad (4.21)$$

where  $a$  characterizes the strength of advection, and  $d$  is a diffusion coefficient. The advection coefficient  $a$  can be equal to zero, or any positive or negative real value, while due to physical reasons the sign of  $d$  is always positive. In the diffusion-free limit  $d = 0$  the advection-diffusion equation reduces to the linear advection equation  $\partial u / \partial t + a \partial u / \partial x = 0$ . A solution of the linear advection-diffusion equation for given initial data  $u_0(x) = u(x, 0)$  on an unbounded spatial domain  $-\infty < x < \infty$  can be found using the coordinate transformation to a reference frame moving with advection speed  $a$

$$x(\tilde{x}, \tilde{t}) = \tilde{x} + a\tilde{t}, \quad (4.22)$$

$$t(\tilde{t}) = \tilde{t}. \quad (4.23)$$

Applying the chain rule to the expression  $u(x(\tilde{x}, \tilde{t}), t(\tilde{t}))$  gives the derivatives

$$\frac{\partial u}{\partial \tilde{x}} = \frac{\partial u}{\partial x} \frac{\partial x}{\partial \tilde{x}} = \frac{\partial u}{\partial x}, \quad (4.24)$$

$$\frac{\partial^2 u}{\partial \tilde{x}^2} = \frac{\partial}{\partial x} \left( \frac{\partial u}{\partial x} \frac{\partial x}{\partial \tilde{x}} \right) = \frac{\partial^2 u}{\partial x^2}, \quad (4.25)$$

$$\frac{\partial u}{\partial \tilde{t}} = \frac{\partial u}{\partial x} \frac{\partial x}{\partial \tilde{t}} + \frac{\partial u}{\partial t} \frac{\partial t}{\partial \tilde{t}} = a \frac{\partial u}{\partial x} + \frac{\partial u}{\partial t}. \quad (4.26)$$

The advection-diffusion equation in coordinates  $\tilde{x}$  and  $\tilde{t}$  transforms to the so-called heat equation

$$\frac{\partial}{\partial \tilde{t}} u(\tilde{x}, \tilde{t}) = d \frac{\partial^2}{\partial \tilde{x}^2} u(\tilde{x}, \tilde{t}). \quad (4.27)$$

The initial condition in new variables is  $u_0 = u(\tilde{x}, 0)$ . With the Fourier transform  $\hat{u}(\omega)$  of a function  $u(\tilde{x})$  and its inverse Fourier transform

$$\hat{u}\{u(\tilde{x})\}(\omega) = \frac{1}{\sqrt{2\pi}} \int_{-\infty}^{+\infty} u(\tilde{x}) \exp(i\omega \tilde{x}) d\tilde{x}, \quad (4.28)$$

$$u\{\hat{u}(\omega)\}(\tilde{x}) = \frac{1}{\sqrt{2\pi}} \int_{-\infty}^{+\infty} \hat{u}(\omega) \exp(-i\tilde{x}\omega) d\omega, \quad (4.29)$$

the solution can be found. Applying the Fourier transform to the heat equation gives  $\partial \hat{u}(\omega; \tilde{t}) / \partial \tilde{t} = -d\omega^2 \hat{u}(\omega; \tilde{t})$  with solution

$$\hat{u}(\omega; \tilde{t}) = \exp(-d\omega^2 \tilde{t}) \hat{u}(\omega; 0), \quad (4.30)$$

where  $\hat{u}(\omega; 0)$  is the Fourier transform of the initial data  $u(\tilde{x}, 0)$ . Inserting  $\hat{u}(\omega; \tilde{t})$  in the inverse Fourier transform  $u(\tilde{x})$  of  $\hat{u}(\omega)$  the solution reads after some simplification

$$u(\tilde{x}, \tilde{t}) = \frac{1}{2\sqrt{\pi d \tilde{t}}} \int_{-\infty}^{+\infty} u(\tilde{x}^*, 0) \exp\left(-\frac{(\tilde{x} - \tilde{x}^*)^2}{4 d \tilde{t}}\right) d\tilde{x}^*. \quad (4.31)$$

Hence, shifting back to the coordinates  $x$  and  $t$ , the general solution of the linear advection-diffusion equation depending on the initial condition  $u(x, 0)$  becomes

$$u(x, t) = \frac{1}{2\sqrt{\pi d t}} \int_{-\infty}^{+\infty} u(\tilde{x}^*, 0) \exp\left(-\frac{(x - a t - \tilde{x}^*)^2}{4 d t}\right) d\tilde{x}^*. \quad (4.32)$$

Common examples are the solutions for a single unit jump in the initial function

$$u_{\text{jump}}(x, 0) = \begin{cases} 0 & : x < 0 \\ 1 & : x \geq 0 \end{cases}, \quad (4.33)$$

$$u_{\text{jump}}(x, t) = \frac{1}{2} \left[ 1 + \operatorname{erf} \left( \frac{x - a t}{2\sqrt{d t}} \right) \right], \quad (4.34)$$

and the solution for an initial function having the shape of a Gaussian distribution

$$u_{\text{hump}}(x, 0) = \exp\left(-\frac{1}{2} \frac{x^2}{\sigma^2}\right), \quad (4.35)$$

$$u_{\text{hump}}(x, t) = \frac{1}{\sqrt{1 + 2 dt/\sigma^2}} \exp\left(-\frac{(x - at)^2}{2\sigma^2 + 4 dt}\right), \quad (4.36)$$

where the standard deviation  $\sigma$  is a measure for the width of the curve  $u_{\text{hump}}(x, 0)$ . The solution  $u_{\text{jump}}(x, t)$  is monotonic, while  $u_{\text{hump}}(x, t)$  is a non-monotonic example. In general it can be concluded, that the solutions  $u(x, t)$  of the linear advection-diffusion equation will stay monotonic for all  $t > 0$ , if the initial function  $u(x, 0)$  is monotonic.

A local approximation for the jump solution at the point  $x = at$ , with the value and the slope of the solution  $u(x, t)$ , reads

$$u_{\text{jump}}(at, t) \approx \frac{1}{2} + \frac{x - at}{\sqrt{4\pi dt}}, \quad (4.37)$$

where  $\delta = \sqrt{4\pi dt}$  can be seen as the thickness of the boundary layer separating the constant solution parts  $u(-\infty, t) = 0$  and  $u(\infty, t) = 1$ . As can be observed in Figure 4.1, the diffusion  $d$  more and more smears out the discontinuous initial function with increasing time  $t$ . In case of the hump-solution, the diffusion leads to a decreasing maximum  $\max(u_{\text{hump}}(x, t)) = u_{\text{hump}}(at, t) = 1/\sqrt{1 + 2 dt/\sigma^2}$  as time  $t$  grows.

It can be concluded, that the linear advection-diffusion equation cannot produce discontinuous solutions from continuous initial conditions. If the initial function includes a discontinuity, e.g. the function  $u_{\text{jump}}(x, 0)$ , it will immediately disappear due to the presence of diffusion. However, in the case of vanishing diffusion  $d = 0$ , the discontinuity will remain for  $t > 0$ .

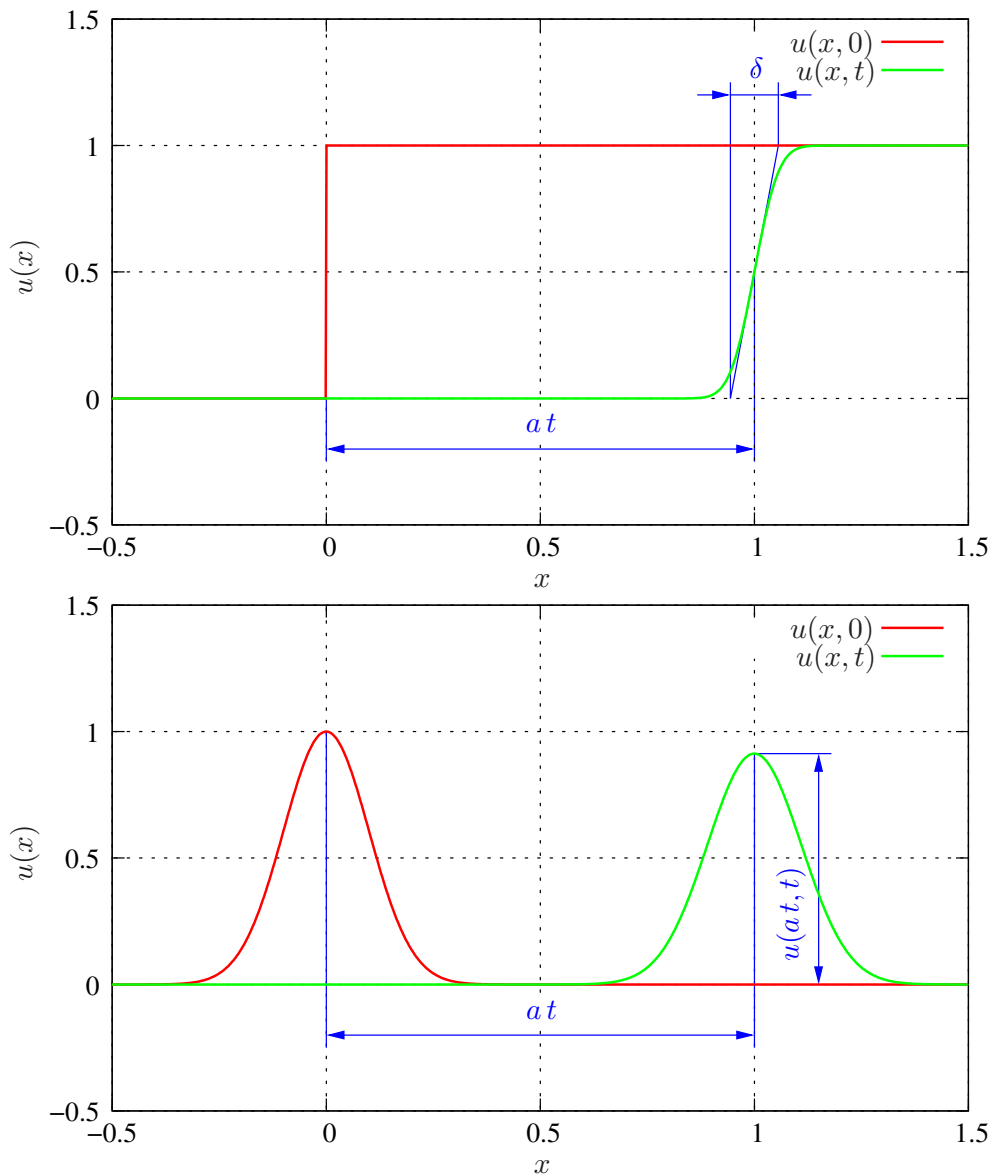


Figure 4.1: Jump (top) and hump (bottom) solution of the linear advection-diffusion equation  $u_t + a u_x = d u_{xx}$  with  $a = 1$ ,  $d = 0.001$  at time  $t = 0$  and  $t = 1$

#### 4.4.2 Total Variation

An important measure for the behavior of solutions is the total variation of a function

$$TV(t) = \int_{-\infty}^{+\infty} \left| \frac{\partial u(x, t)}{\partial x} \right| dx, \quad (4.38)$$

If the solution  $u(x, t)$  is monotonic, e.g.  $\partial u / \partial x \geq 0$  or  $\partial u / \partial x \leq 0$  for all  $-\infty < x < \infty$  and all  $t > 0$ , the absolute value  $|\partial u / \partial x|$  can be substituted by the derivative

$\partial u/\partial x$  or by  $-\partial u/\partial x$ , respectively. In the first case, the total variation becomes  $TV = u(\infty, t) - u(-\infty, t)$ , while the second case gives  $TV = u(-\infty, t) - u(\infty, t)$ . However, if the solution is monotonic, the total variation equals its initial value  $TV(t) = TV(0)$ . Evaluating the total variation for the jump and the hump examples gives

$$TV_{\text{jump}}(t) = 1, \quad (4.39)$$

$$TV_{\text{hump}}(t) = \frac{2}{\sqrt{1 + 2dt/\sigma^2}}. \quad (4.40)$$

The initial value for the hump function gives  $TV_{\text{hump}}(0) = 2$ . Hence, in this non-monotonic situation it is obvious to see that  $TV(t) \leq TV(0)$  for  $t \geq 0$ . In the diffusion-free limit  $d = 0$  the total variation becomes  $TV(t) = TV(0)$  for  $t \geq 0$ . Based on the results of these simple examples, it can be concluded, that on unbounded domains in space the total variation keeps its initial value  $TV(0)$  if no diffusion is present (propagation of a solitary wave), or if in case  $d > 0$  the initial condition is a monotonic function.

The discrete version of the total variation definition can be used for the design of numerical methods. If a numerical scheme finds solutions of the linear advection equation  $\partial u/\partial t + a\partial u/\partial x = 0$  where  $TV(t) > TV(0)$ , the method is physically incorrect. If, in contrast, the numerical solution of the linear advection equation gives  $TV(t) < TV(0)$ , this scheme produces numerical diffusion that mimics a physical correct diffusion coefficient  $d > 0$ . Hence, the goal is to find a numerical method that is total variation non-increasing (TVNI).

## 4.5 Non-Linear Scalar Advection Equation

The non-linear scalar advection equation

$$\frac{\partial}{\partial t}u(x, t) + \frac{\partial}{\partial x}f(u(x, t)) = 0, \quad (4.41)$$

where the flux-function  $f(u(x, t))$  depends non-linear on  $u$ , is a prototype equation to discuss the non-linear effects on the solution, in contrast to the solutions of linear flux functions. The most simple example of a linear flux function is  $f(u(x, t) = au(x, t)$ , where the constant  $a$  represents the propagation speed of advective waves. The most prominent example of a non-linear flux functions  $f(u) = u^2/2$  leads to the inviscid Burgers equation

$$\frac{\partial}{\partial t}u + \frac{\partial}{\partial x}\left(\frac{u^2}{2}\right) = 0. \quad (4.42)$$

Even if the initial function  $u(x, 0)$  and its space-derivative  $\frac{\partial}{\partial x}u(x, 0)$  are continuous, the solution of the Burgers equation can produce discontinuities at  $t > 0$ . The reason for this phenomenon is the solution-dependent speed of the propagating waves. Hence, the Burgers equation is frequently used to test methods developed for equations including non-linearities, that lead to steepening of solutions or to discontinuities, e.g. the Euler equations.

# Chapter 5

## Numerical Methods

### 5.1 Introduction in Numerics

In this chapter the most common methods to solve the flow of fluids are briefly discussed. Although only the method presented in Chapter 6 is used for the self-coded solver of reciprocating compressor flow, the overview of other methods provides the arguments for the choice of the selected method. Furthermore, the discussion allows to demonstrate the state-of-the-art and possible further development. The basic concepts of approximation methods are presented, and the common expressions are explained. Since finding an approximate solution usually requires to store numbers in the memory of a computer, this field is also called numerics. Approximation methods are necessary for situations, where an analytical result to a mathematical problem is not known, or it is too cumbersome to find. Finding a solution can be difficult due to initial or boundary conditions, e.g. on complex geometries, or due to non-linearity of the field equations that model the physics. For almost all of the non-linear equations, the superposition of elementary solutions does not seem to be easy, although examples exist, e.g. the Burgers equation, where a transformation to a linear equation makes superposition possible. However, sometimes the superposition principle is not used, even if the field equation allows its application. One example is the linear heat equation solved with the finite element method (FEM) instead of a boundary element method (BEM), that just needs to combine a large number of elementary field solutions to approximately fulfill certain boundary conditions.

### 5.2 Approximation Methods

A lot of different approximation methods exist for different types of mathematical and physical models. The most common methods for ordinary differential equations (ODEs) and partial differential equations (PDEs) are

- Finite Difference Methods (FDM),
- Finite Volume Methods (FVM),
- Finite Element Methods (FEM),



where the methods FVM and FEM can be seen as weighted residual methods (WRM). The weighted residual method consists of approximation functions to the differential equation operator, and test functions that can be different in general. The product of approximated differential equation and test function is then integrated over the domain or sub-domains. The unknown coefficients of the approximation function, the weights, are chosen to minimize the residual of the volume integral. Therefore, the methods are called WRM.

If the test function related to each sub-domain has the constant value 1 inside the sub-domain and 0 outside, this is a finite volume method. Hence, a FVM is the integral of an approximated differential equation over the volume of a sub-domain, usually called a cell. For test functions that differ from a constant, the most common choice for a test function used for the FEM is the approximation function. Applying the same function set to test functions and approximation functions is called a Galerkin method. The residual is then the integral of squared deviations to the exact solution.

If the solution is expected to be discontinuous, a FDM can not be used, because the method directly approximates derivatives, that do not exist then. Finite volume methods, and some finite element methods, e.g the discontinuous Galerkin method (DGM), are capable to handle discontinuities. While the reconstruction process of FVM usually assumes a discontinuity at every boundary of a cell, the discontinuous Galerkin version of FEM assumes the discontinuity only at boundaries of every element, and continuous functions inside the element. Elements are also sub-domains, but they consist of more nodes inside the element, that store the unknowns and build the approximation to the solution. Placing the nodes on certain positions helps to find interpolation functions from the values stored in the nodes. A cell used in FVM has exactly one unknown for every variable, which is usually the cell average. The cell average is the unknown integrated over the cell domain, divided by the cell volume.

The reconstruction of discontinuities at cell boundaries or element boundaries, requires a special routine of solving the jumps in the solutions, which are called Riemann problems. If the so-called Riemann flux, related to each sub-domain boundary, is used to find the unknowns inside the cell or element, the method is called to be conservative. This means, that if the flow of a variable is zero on all boundaries of a sub-domain, the variable value related to the sub-domain will remain unchanged, or in other words, is conserved. While the FVM is conservative by construction, the residual minimization of DGM leads to non-conservative methods.

A special finite element method is the so-called spectral element method (SEM). The whole domain is then approximated by a single element, that uses a very accurate approximation function inside this spectral element. If a FEM uses just a few elements for the domain decomposition, but with highly accurate approximation functions inside the element, this method is said to have quasi-spectral properties.

During the last decade, conservative methods have been developed, that are somehow in-between the classical methods. The spectral volume method (SVM) uses elements, that are again sub-divided in smaller sub-domains, the cells. Every cell stores a single value of the unknown variable, while the number of unknowns stored in an element correlates with the number of cells the element contains. A continuous approximation to a solution inside the element can then be found using the volume averages of all the cells related to that element. The solution of the unknown cell averages is found using continuous fluxes derived from the in-element reconstructions, and with discontinuous fluxes at element boundaries computed with Riemann solvers. Since a flux is computed for every cell boundary, the SVM is conservative. This technique can again become cumbersome, if too many cells are used for reconstruction. However, this is the quasi-spectral idea behind the SVM.

Recently, another method has gained popularity, with the goal of reducing the complexity of SVM. The so-called spectral difference method (SDM) uses nodes inside the elements instead of cells. Hence, the method is highly related to the DGM, because the in-element node interpolation is continuous, while a discontinuous (numerical) flux is computed at element boundaries. With numerical fluxes computed with a Riemann solver at element boundary nodes and the flux values at nodes inside the SD-element, an accurate continuous reconstruction of a space-dependent flux function related to every element can be found. The space derivatives of these flux functions evaluated at element nodes can then directly be used to evolve the unknowns in time based on the original partial differential equation (PDE), instead of integrating the PDE over a volume and minimizing a residual. If the flux reconstruction procedure does only depend on numerical fluxes computed at element boundaries, SDM becomes a conservative finite difference method. Although some SDM-implementations in academic software exist, the stability of these methods is still part of investigation. Especially the way how the flux is reconstructed or interpolated inside the element seems to be crucial for the behavior in terms of stability and the appearance of oscillating solutions.

### 5.2.1 Point Values and Mean Values

The result of numerical approximation methods has to be stored as numerical values. This can be done by storing the solution data at specific points in space, or the mean values of intervals. In Figure 5.1, a function  $u(x)$  is shown in a one-dimensional domain  $x$ . Let's assume  $u(x)$  is a given function, e.g. the initial condition  $u(x, 0)$  of a time-space-dependent solution  $u(x, t)$ , where  $t$  is the time. As sketched in Figure 5.1, the  $x$ -axis is sub-divided into intervals, shown in blue color, using the list of coordinates

$$\dots, x_{i-5/2}, x_{i-3/2}, x_{i-1/2}, x_{i+1/2}, x_{i+3/2}, \dots \quad (5.1)$$

where the index  $i$  can be any integer number, that allows to shift to another position in the list.

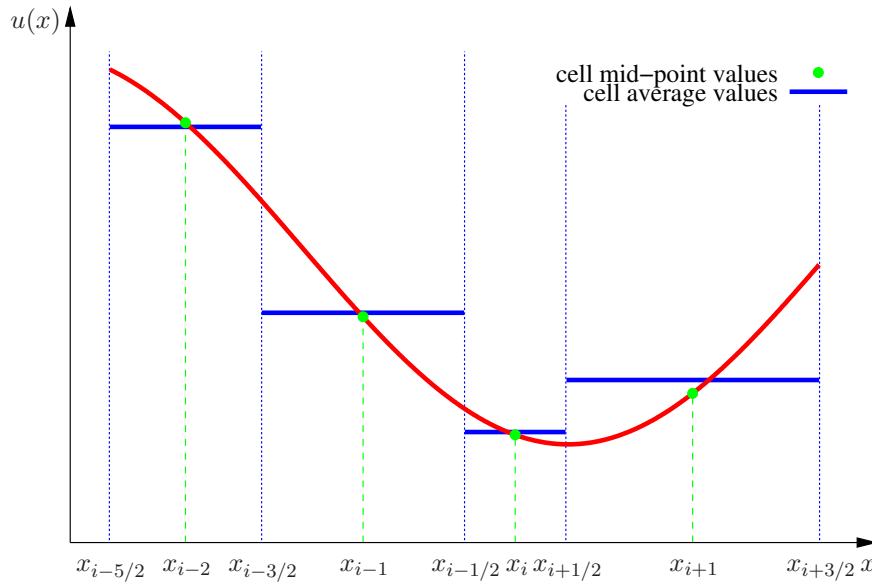


Figure 5.1: Function  $u(x)$  and space  $x$ , subdivided in intervals (cells)

The intervals

$$\begin{aligned}
 & \dots \\
 & x_{i-5/2} < x < x_{i-3/2}, \\
 & x_{i-3/2} < x < x_{i-1/2}, \\
 & x_{i-1/2} < x < x_{i+1/2}, \\
 & x_{i+1/2} < x < x_{i+3/2}, \\
 & \dots
 \end{aligned}$$

are called the cells  $\dots, \mathcal{C}_{i-2}, \mathcal{C}_{i-1}, \mathcal{C}_i, \mathcal{C}_{i+1}, \dots$ , where each cell boundary in Equation (5.1) has exactly two cell neighbors. The cell  $\mathcal{C}_i$  has a length  $\Delta x_i = x_{i+1/2} - x_{i-1/2}$  and a mid-point position  $x_i = (x_{i+1/2} - x_{i-1/2})/2$ , where shifting the index  $i$  defines the length of the other cells  $\Delta x_{i-5/2}, \Delta x_{i-3/2}, \Delta x_{i-1/2}, \Delta x_{i+1/2}$  and their mid-point positions  $x_{i-2}, x_{i-1}, x_i, x_{i+1}$ . The values of the function  $u(x)$  evaluated at the cell mid-point positions  $\dots, u(x_{i-2}), u(x_{i-1}), u(x_i), u(x_{i+1}), \dots$  built the list of cell mid-point values  $\dots, u_{i-2}, u_{i-1}, u_i, u_{i+1}, \dots$ . If a point-wise numerical procedure is used, the positions  $x_i$  and the values  $u_i$  are stored for  $0 \leq i \leq i_{\max} - 1$ , where  $i_{\max}$  is the number of points. Depending on the information required for the numerical method, this can be done with or without storing the cell boundary coordinates.

Another possibility is to store the cell average values  $U_i$ , these are the mean value of every cell

$$U_i = \frac{1}{\Delta x_i} \int_{x_{i-1/2}}^{x_{i+1/2}} u(x) dx. \quad (5.2)$$

As can be seen in Figure 5.1, the cell average values  $U_i$ , shown in blue color for every cell, deviate a little bit from the the cell mid-point values  $u_i$ , shown in green. Applying a Taylor series expansion for the function  $u(x)$  around the cell mid-point position

$$U_i = \frac{1}{\Delta x_i} \int_{x_{i-1/2}}^{x_{i+1/2}} \left[ u_i + u'(x_i) \cdot (x - x_i) + \frac{1}{2} u''(x_i) \cdot (x - x_i)^2 + \dots \right] dx, \quad (5.3)$$

$$U_i = \frac{1}{\Delta x_i} \int_{-\Delta x_i/2}^{\Delta x_i/2} \left[ u_i + u'(x_i) \cdot \tilde{x} + \frac{1}{2} u''(x_i) \cdot \tilde{x}^2 + \dots \right] d\tilde{x}, \quad (5.4)$$

$$U_i = u_i + \frac{1}{24} u''(x_i) \cdot \Delta x_i^2 + \dots, \quad (5.5)$$

shows, that the size of the deviation ( $U_i - u_i$ ) becomes smaller as the cell size  $\Delta x_i$  decreases. However, a numerical method produces an approximation error of maybe comparable size. Therefore, it is important to make a difference between  $u_i$  and  $U_i$ .

## 5.2.2 Interpolation and Reconstruction

### 5.2.2.1 Local Interpolation Trough Points

The simplest way how to find interpolation functions is to use so-called shape functions. These are special functions, with the property of having a value of one in a certain point with index  $i$ , and a value of zero in all the other points  $j$  used for the shape function interpolation. For a local polynomial interpolation function  $u(x)$  using  $(n + 1)$  points, this can be done with the Lagrange polynomials basis polynomials

$$X_i(x) = \prod_{j=0, j \neq i}^n \frac{x - x_j}{x_i - x_j}, \quad (5.6)$$

$$u(x) = \sum_{i=0}^n u_i X_i(x), \quad (5.7)$$

where  $u_i$  are the function values in points  $x_i$ . The condition  $j \neq i$  avoids the division by zero. A simple example is used here to demonstrate the procedure. Using four points  $x_{i-2}, x_{i-1}, x_i, x_{i+1}$  with four function values  $u_{i-2}, u_{i-1}, u_i, u_{i+1}$ , as shown in Figure 5.1, a cubic polynomial is obtained, that is a local approximation to the

function  $u(x)$

$$X_{i-2}(x) = \frac{x - x_{i-1}}{x_{i-2} - x_{i-1}} \frac{x - x_i}{x_{i-2} - x_i} \frac{x - x_{i+1}}{x_{i-2} - x_{i+1}}, \quad (5.8)$$

$$X_{i-1}(x) = \frac{x - x_{i-2}}{x_{i-1} - x_{i-2}} \frac{x - x_i}{x_{i-1} - x_i} \frac{x - x_{i+1}}{x_{i-1} - x_{i+1}}, \quad (5.9)$$

$$X_i(x) = \frac{x - x_{i-2}}{x_i - x_{i-2}} \frac{x - x_{i-1}}{x_i - x_{i-1}} \frac{x - x_{i+1}}{x_i - x_{i+1}}, \quad (5.10)$$

$$X_{i+1}(x) = \frac{x - x_{i-2}}{x_{i+1} - x_{i-2}} \frac{x - x_{i-1}}{x_{i+1} - x_{i-1}} \frac{x - x_i}{x_{i+1} - x_i}, \quad (5.11)$$

$$u(x) = u_{i-2} X_{i-2}(x) + u_{i-1} X_{i-1}(x) + u_i X_i(x) + u_{i+1} X_{i+1}(x). \quad (5.12)$$

In two or three dimensions, it is much more complicated to find the Lagrange polynomials. Usually complete polynomials are required to achieve the same approximation accuracy as in the one-dimensional case. For the 2d case a complete linear, quadratic or cubic polynomial requires 3, 6 or 10 points, respectively. In 3d, the required point number raises to 4, 10 and 20 for a complete linear, quadratic and cubic polynomial. It may happen, that the location of the points in 2d and 3d space is in such a way, that the determination of the polynomial coefficients fails. This cannot happen in the 1d case, as long as all points have a different location. However, even if a complete polynomial interpolation exists in 2d or 3d, it is usually very hard to find for general point positions.

### 5.2.2.2 Local Reconstruction Of Mean Values

A local reconstruction function  $u_i(x)$  is a function designed in such a way, that given cell average values  $\dots, U_{i-1}, U_i, U_{i+1}, \dots$  of selected cells are obtained, when building the mean of this function for the selected cells  $\dots, \mathcal{C}_{i-1}, \mathcal{C}_i, \mathcal{C}_{i+1}, \dots$ , according to Equation (5.2). The most simple local reconstruction is a constant value inside of each cell shown in Figure 5.1. With the piecewise constant reconstruction for every cell

$$u_i(x) = U_i, \quad (5.13)$$

the given cell average values of the cells are automatically obtained, when building the mean. In general, the piecewise constant reconstruction function is discontinuous at the cell boundaries. A reconstruction function  $u(x)$  that gives the cell average  $U_i$  and that of the neighbor cell  $U_{i+1}$  when building the mean, is the linear function

$$u_i(x) = U_i + (U_{i+1} - U_i) \frac{x - x_i}{x_{i+1} - x_i}, \quad (5.14)$$

where  $x_i = (x_{i+1/2} - x_{i-1/2})/2$  and  $x_{i+1} = (x_{i+3/2} - x_{i+1/2})/2$  are the cell mid-point positions. The linear function also has the properties  $u_i(x_i) = U_i$  and  $u_i(x_{i+1}) = U_{i+1}$ . Hence, the value of the linear reconstruction function in the cell-mid point is the cell average value of the local cell. A piecewise quadratic reconstruction  $u_i(x)$  that has the same mean values as the given cell averages  $U_{i-1}, U_i, U_{i+1}$  is more difficult to find. One systematic way is to use shape functions for the integral function

$U(x) := \int u(x) dx$  of  $u(x)$ , and to find  $u(x)$  afterwards, building the derivative. For the quadratic reconstruction, three shape functions  $X_{i-1/2}(x)$ ,  $X_{i+1/2}(x)$ ,  $X_{i+3/2}(x)$  are used to build  $U(x)$

$$X_{i-1/2}(x) = \frac{x - x_{i-3/2}}{x_{i-1/2} - x_{i-3/2}} \frac{x - x_{i+1/2}}{x_{i-1/2} - x_{i+1/2}} \frac{x - x_{i+3/2}}{x_{i-1/2} - x_{i+3/2}}, \quad (5.15)$$

$$X_{i+1/2}(x) = \frac{x - x_{i-3/2}}{x_{i+1/2} - x_{i-3/2}} \frac{x - x_{i-1/2}}{x_{i+1/2} - x_{i-1/2}} \frac{x - x_{i+3/2}}{x_{i+1/2} - x_{i+3/2}}, \quad (5.16)$$

$$X_{i+3/2}(x) = \frac{x - x_{i-3/2}}{x_{i+3/2} - x_{i-3/2}} \frac{x - x_{i-1/2}}{x_{i+3/2} - x_{i-1/2}} \frac{x - x_{i+1/2}}{x_{i+3/2} - x_{i+1/2}}, \quad (5.17)$$

$$U(x) = U_{i-1} X_{i-1/2}(x) + U_i X_{i+1/2}(x) + U_{i+1} X_{i+3/2}(x). \quad (5.18)$$

All shape functions have a value of one at their related cell boundary  $X_{i-1/2}(x_{i-1/2}) = X_{i+1/2}(x_{i+1/2}) = X_{i+3/2}(x_{i+3/2}) = 1$ , but a value of zero at all other cell boundaries. Hence, the function  $U(x)$  has the value of the given cell averages at cell boundaries  $x_{i-1/2}$ ,  $x_{i+1/2}$ ,  $x_{i+3/2}$ , but a zero value  $U(x_{i-3/2}) = 0$  in the most left cell boundary. The derivative  $u(x) = dU/dx$  gives the piecewise quadratic reconstruction

$$u(x) = U_{i-1} \frac{d}{dx} X_{i-1/2}(x) + U_i \frac{d}{dx} X_{i+1/2}(x) + U_{i+1} \frac{d}{dx} X_{i+3/2}(x). \quad (5.19)$$

The mean values of the function  $u(x)$  for the cells  $\mathcal{C}_{i-1}$ ,  $\mathcal{C}_i$ ,  $\mathcal{C}_{i+1}$  are the given cell averages  $U_{i-1}$ ,  $U_i$ ,  $U_{i+1}$ . If all cells have the same size  $\Delta x = (x_{i+3/2} - x_{i+1/2}) = (x_{i+1/2} - x_{i-1/2}) = (x_{i-1/2} - x_{i-3/2})$ , the quadratic reconstruction function becomes more simple

$$u(x) = \frac{1}{6}(2U_{i+1} + 5U_i - U_{i-1}) + (U_{i+1} - U_i) \left( \frac{x - x_{i+1/2}}{\Delta x} \right) + \frac{1}{2}(U_{i+1} - 2U_i + U_{i-1}) \left( \frac{x - x_{i+1/2}}{\Delta x} \right)^2. \quad (5.20)$$

### 5.2.3 Approximation Accuracy

The accuracy of an approximation is found, comparing the deviation of a function to its approximation function in the limit  $\Delta x \rightarrow 0$  for spatial discretizations, or  $\Delta t \rightarrow 0$  for temporal discretization. If polynomial approximations are used, the Taylor series expansion is a convenient tool for deriving the accuracy depending on the order of the deviation error  $\mathcal{O}(\Delta x^p)$ , where  $p$  is some integer number. If the function is not continuous, the Taylor series expansion is not helpful to measure the accuracy. Integral conditions have to be applied to measure the error close to the discontinuities.

## 5.3 Linear Scalar Advection Equation

The time and space dependent linear scalar advection equation  $\partial u / \partial t + a \partial u / \partial x = 0$  with constant wave propagation speed  $a$ , is a simple model equation for a scalar  $u(x, t)$ , to discuss numerical methods for hyperbolic problems. Using the indices  $()_t$  and  $()_x$  for the time and space derivatives, the equation reads

$$u_t + a u_x = 0. \quad (5.21)$$

### 5.3.1 Cauchy Kowalewski Procedure

If the solution  $u(x, t_n)$  of Equation (5.21) is known at time  $t_n$ , it may be interesting to have a simple procedure to find an approximate solution to Equation (5.21) at time  $t_{n+1} = t_n + \Delta t$ , where  $\Delta t$  is a small time step. The Cauchy Kowalewski procedure uses a Taylor series in time, and substitutes all the time derivatives by space derivatives, based on the original differential Equation (5.21).

$$u(x, t_{n+1}) = u(x, t_n) + \Delta t u_t(x, t_n) + \frac{1}{2} \Delta t^2 u_{tt}(x, t_n) + \frac{1}{6} \Delta t^3 u_{ttt}(x, t_n) + \dots \quad (5.22)$$

$$u(x, t_{n+1}) = u(x, t_n) - \Delta t a u_x(x, t_n) + \frac{1}{2} \Delta t^2 a^2 u_{xx}(x, t_n) - \frac{1}{6} \Delta t^3 a^3 u_{xxx}(x, t_n) + \dots \quad (5.23)$$

Hence, depending on where the Taylor series is truncated, the method produces a certain time discretization error  $(\Delta t)^{p+1}$ , where  $p$  is the order of the scheme with respect to time. If the data is stored in space points  $\dots, x_{i-1}, x_i, x_{i+1}, \dots$ , the value  $u(x_i, t_{n+1})$  at point  $x_i$  can be computed, if approximations to  $u_x(x_i, t_n)$ ,  $u_{xx}(x_i, t_n)$ ,  $\dots$  are available. Accurate approximations to the space-derivatives can be found, using a Taylor series in space. This leads to a finite difference method having a certain order of accuracy with respect to time and space, depending on the space-discretization.

### 5.3.2 Finite Difference Methods

#### 5.3.2.1 First Order Upwind Scheme

The analytical solution  $u(x, t) = u(x - at)$  of the linear advection equation indicates, that the result at time  $t_{n+1} = t_n + \Delta t$  should only depend on values that will propagate through the space point  $x_i$ , when time evolves from  $t_n$  to  $t_{n+1}$ . Hence, for a wave speed  $a > 0$ , only values in upwind-directed points  $x_i, x_{i-1}, x_{i-2}, \dots$  shall be used to approximate the space derivatives at point  $x_i$ . For the first order upwind scheme, the Taylor series

$$u(x_{i-1}, t_n) = u(x_i, t_n) - \Delta x u_x(x_i, t_n) + \frac{1}{2} \Delta x^2 u_{xx}(x_i, t_n) + \dots, \quad (5.24)$$

$$u_x(x_i, t_n) = \frac{u(x_i, t_n) - u(x_{i-1}, t_n)}{\Delta x} + \frac{1}{2} \Delta x u_{xx}(x_i, t_n) + \dots, \quad (5.25)$$

gives the approximation for  $u_x(x_i, t_n)$ , where  $\Delta x = x_i - x_{i-1}$  is the grid spacing. Evaluating Equation (5.23) at  $x_i$  and substituting the first space derivative gives

$$u_i^{n+1} = u_i^n - \Delta t a \left[ \frac{u_i^n - u_{i-1}^n}{\Delta x} + \frac{1}{2} \Delta x u_{xx}(x_i, t_n) + \dots \right] + \frac{1}{2} \Delta t^2 a^2 u_{xx}(x_i, t_n) + \dots, \quad (5.26)$$

where  $u_i^{n+1} = u(x_i, t_{n+1})$ ,  $u_i^n = u(x_i, t_n)$ ,  $u_{i-1}^n = u(x_{i-1}, t_n)$  was used. Hence, the first order upwind method for the linear advection equation reads

$$u_i^{n+1} = u_i^n - \frac{a \Delta t}{\Delta x} [u_i^n - u_{i-1}^n], \quad (5.27)$$

with leading order error estimates  $\mathcal{O}(\Delta x \Delta t)$  and  $\mathcal{O}(\Delta t^2)$  for the solution expression  $u_i^{n+1}$ . Both error terms appearing in Equation (5.26),  $-\frac{1}{2} \left(\frac{a \Delta t}{\Delta x}\right) \Delta x^2 u_{xx}(x_i, t_n)$  and  $\frac{1}{2} \left(\frac{a \Delta t}{\Delta x}\right)^2 \Delta x^2 u_{xx}(x_i, t_n)$ , are of comparable size  $\mathcal{O}(\Delta x^2)$ , if the Courant number

$$C = \frac{a \Delta t}{\Delta x} \quad (5.28)$$

is an order one term  $C = \mathcal{O}(1)$ . The von Neumann stability analysis in Section 5.3.5 will demonstrate, that the maximum allowable value of the Courant number for stability of the first order upwind scheme is  $C_{max} = 1$ . For  $a < 0$  the upwinding gives  $u_i^{n+1} = u_i^n - C [u_{i+1}^n - u_i^n]$ . Hence, the direction of spatial discretization changes with the sign of the wave speed  $a$ .

### 5.3.2.2 Second Order Central Scheme

The second order central scheme presented here, is the Lax-Wendroff [49] finite difference scheme. Central means, that the values at points  $x_{i-1}, x_i, x_{i+1}$  are used to find the approximation of the space derivatives  $u_x, u_{xx}$  in point  $x_i$ . Hence, this discretization is not following the philosophy of pure upwinding, because it also uses the point  $x_{i+1}$  on the downwind side of wave propagation, if  $a$  is assumed to be positive. With  $\Delta x_R = x_{i+1} - x_i$ ,  $\Delta x_L = x_i - x_{i-1}$  and  $u_x = u_x(x_i, t_n)$ ,  $u_{xx} = u_{xx}(x_i, t_n)$ ,  $u_{xxx} = u_{xxx}(x_i, t_n)$ , the Taylor series expansions

$$u_{i+1}^n = u_i^n + \Delta x_R u_x + \frac{1}{2} \Delta x_R^2 u_{xx} + \frac{1}{6} \Delta x_R^3 u_{xxx} + \dots, \quad (5.29)$$

$$u_{i-1}^n = u_i^n - \Delta x_L u_x + \frac{1}{2} \Delta x_L^2 u_{xx} - \frac{1}{6} \Delta x_L^3 u_{xxx} + \dots, \quad (5.30)$$

gives approximations for the space derivatives

$$u_x = \frac{\Delta x_L^2 u_{i+1}^n + (\Delta x_R^2 - \Delta x_L^2) u_i^n - \Delta x_R^2 u_{i-1}^n}{\Delta x_R \Delta x_L (\Delta x_R + \Delta x_L)} - \frac{1}{6} \Delta x_R \Delta x_L u_{xxx} + \dots, \quad (5.31)$$

$$u_{xx} = 2 \frac{\Delta x_L u_{i+1}^n - (\Delta x_R + \Delta x_L) u_i^n + \Delta x_R u_{i-1}^n}{\Delta x_R \Delta x_L (\Delta x_R + \Delta x_L)} - \frac{1}{3} (\Delta x_R - \Delta x_L) u_{xxx} + \dots \quad (5.32)$$



Introducing the grid-size ratio  $\chi = \Delta x_R / \Delta x_L$  and the average grid-spacing  $\Delta x = \frac{1}{2}(\Delta x_R + \Delta x_L)$  the derivatives simplify to

$$u_x = \frac{u_{i+1}^n + (\chi^2 - 1)u_i^n - \chi^2 u_{i-1}^n}{2\chi\Delta x} - \frac{2}{3} \frac{\chi}{(1+\chi)^2} \Delta x^2 u_{xxx} + \dots, \quad (5.33)$$

$$u_{xx} = \frac{(1+\chi)(u_{i+1}^n - (1+\chi)u_i^n + \chi u_{i-1}^n)}{2\chi\Delta x^2} + \frac{2}{3} \frac{1-\chi}{1+\chi} \Delta x u_{xxx} + \dots. \quad (5.34)$$

Hence, if  $\chi = \mathcal{O}(1)$ , the approximation error of  $u_x$  is  $\mathcal{O}(\Delta x^2)$ , while the error of  $u_{xx}$  is  $\mathcal{O}(\Delta x)$ . Using the Courant number  $C = a\Delta t / \Delta x$  built with the average grid-spacing  $\Delta x = \frac{1}{2}(\Delta x_R + \Delta x_L)$  in Equation (5.23), and substituted the spatial derivatives  $u_x$  and  $u_{xx}$

$$u_i^{n+1} = u_i^n - C u_x \Delta x + \frac{1}{2} C^2 u_{xx} \Delta x^2 - \frac{1}{6} C^3 u_{xxx} \Delta x^3 + \dots, \quad (5.35)$$

$$u_i^{n+1} \approx u_i^n - C \frac{u_{i+1}^n + (\chi^2 - 1)u_i^n - \chi^2 u_{i-1}^n}{2\chi} + \frac{1}{2} C^2 \frac{u_{i+1}^n - (1+\chi)u_i^n + \chi u_{i-1}^n}{2\chi/(1+\chi)}, \quad (5.36)$$

shows that the error of  $u_i^{n+1}$  in Equation (5.36) is  $\mathcal{O}(\Delta x^3)$ , because  $u_x \Delta x$  and  $u_{xx} \Delta x^2$  appear in the numerical scheme. If in general, schemes with approximation error  $(\Delta x)^{p+1}$  are said to have order  $p$ , this is a scheme of order 2, or in other words a second order scheme. The stability limit of the scheme is expected to depend on  $C$  and  $\chi$ . However, the stability analysis in Section 5.3.5 will only be applied to an equi-sized grid, where  $\Delta x = \Delta x_R = \Delta x_L$ . Hence, for  $\chi = \Delta x_R / \Delta x_L = 1$ , the finite difference Lax-Wendroff scheme simplifies to

$$u_i^{n+1} = u_i^n - \frac{1}{2} C (u_{i+1}^n - u_{i-1}^n) + \frac{1}{2} C^2 (u_{i+1}^n - 2u_i^n + u_{i-1}^n). \quad (5.37)$$

This is the classical method presented by Lax and Wendroff [49]. Since a Taylor series is equivalent to a polynomial up to a certain degree, the spatial derivatives for the second order scheme can also be obtained using a local quadratic interpolation function at time  $t_n$

$$X_{i-1}(x) = \frac{x - x_i}{x_{i-1} - x_i} \frac{x - x_{i+1}}{x_{i-1} - x_{i+1}}, \quad (5.38)$$

$$X_i(x) = \frac{x - x_{i-1}}{x_i - x_{i-1}} \frac{x - x_{i+1}}{x_i - x_{i+1}}, \quad (5.39)$$

$$X_{i+1}(x) = \frac{x - x_{i-1}}{x_{i+1} - x_{i-1}} \frac{x - x_i}{x_{i+1} - x_i}, \quad (5.40)$$

$$u(x, t_n) = u_{i-1}^n X_{i-1}(x) + u_i^n X_i(x) + u_{i+1}^n X_{i+1}(x), \quad (5.41)$$

where the first derivative  $u_x(x_i, t_n) = u_{i-1}^n \frac{\partial}{\partial x} X_{i-1}(x_i) + u_i^n \frac{\partial}{\partial x} X_i(x_i) + u_{i+1}^n \frac{\partial}{\partial x} X_{i+1}(x_i)$  and the second derivative  $u_{xx}(x_i, t_n) = u_{i-1}^n \frac{\partial^2}{\partial x^2} X_{i-1}(x_i) + u_i^n \frac{\partial^2}{\partial x^2} X_i(x_i) + u_{i+1}^n \frac{\partial^2}{\partial x^2} X_{i+1}(x_i)$  can be obtained from the function  $u(x, t_n)$ , evaluated at position  $x_i$ . This method gives the same result and accuracy for the approximations of  $u_x$  and  $u_{xx}$  used within the Cauch Kowalewski procedure, but it is maybe more convenient for higher order approximations, then the Taylor series expansion.

### 5.3.2.3 Third Order Upwind-Biased Scheme

The local cubic polynomial interpolation of Equations (5.8), (5.9), (5.10), (5.11), (5.12), using four points, can be used to derive a third order upwind-biased scheme. The scheme computes the value  $u_i^{n+1} = u(x_i, t_{n+1})$  based on data  $u_{i-2}^n, u_{i-1}^n, u_i^n, u_{i+1}^n$ . Assuming a positive wave speed  $a$ , the points  $x_{i-1}$  and  $x_{i-2}$  are upwind and far-upwind of the point  $x_i$ , while  $x_{i+1}$  is a downwind point. The stencil is said to be upwind-biased, because two points in upwind-direction are used, and only one point in downwind-direction. For simplicity, only the case with equi-sized point distances  $\Delta x = (x_{i+1} - x_i) = (x_i - x_{i-1}) = (x_{i-1} - x_{i-2})$  is discussed. The spatial derivatives

$$u_x = \frac{2u_{i+1}^n + 3u_i^n - 6u_{i-1}^n + u_{i-2}^n}{6\Delta x} - \frac{1}{12}u_{xxxx}\Delta x^3 + \dots, \quad (5.42)$$

$$u_{xx} = \frac{u_{i+1}^n - 2u_i^n + u_{i-1}^n}{\Delta x^2} - \frac{1}{12}u_{xxxx}\Delta x^2 + \dots, \quad (5.43)$$

$$u_{xxx} = \frac{u_{i+1}^n - 3u_i^n + 3u_{i-1}^n - u_{i-2}^n}{\Delta x^3} + \frac{1}{2}u_{xxxx}\Delta x + \dots, \quad (5.44)$$

inserted in the Cauchy Kowalewski procedure of Equation (5.23) gives the third order upwind-biased finite difference scheme for the linear advection equation with positive wave speed  $a$

$$u_i^{n+1} = \frac{1}{6}(-2C + 3C^2 - C^3)u_{i+1}^n + \frac{1}{6}(6 - 3C - 6C^2 + 3C^3)u_i^n + \frac{1}{6}(6C + 3C^2 - 3C^3)u_{i-1}^n + \frac{1}{6}(-C + C^3)u_{i-2}^n. \quad (5.45)$$

The leading order approximation error of  $u_i^{n+1}$  is  $\mathcal{O}(\Delta x^4)$ .

### 5.3.3 Finite Volume Methods

In contrast to finite difference methods, finite volume methods usually store cell average values according to Equation (5.2), instead of values in points. The basic idea behind the finite volume method (FVM) is to find approximate solution  $\mathbf{U}(\mathbf{x}, t)$  in an integral sense to a system of partial differential equation, e.g. the one-dimensional equation

$$\frac{\partial}{\partial t}\mathbf{U}(x, t) + \frac{\partial}{\partial x}\mathbf{f}(\mathbf{U}(x, t)) = \mathbf{0}. \quad (5.46)$$

Therefore, the equations are integrated in space over the volume of a cell, and integrated in time over the actual size of the time step  $\Delta t = t_{n+1} - t_n$ . Assume that a cell  $\mathcal{C}_i$  shown in Figure 5.1 is a three-dimensional object with length  $\Delta x = x_{i+1/2} - x_{i-1/2}$ , constant height  $\Delta y$  and constant width  $\Delta z$ . Then, integration over the cell volume  $\Delta x \Delta y \Delta z$  of Equation (5.46) yields

$$\Delta y \Delta z \frac{d}{dt} \int_{x_{i-1/2}}^{x_{i+1/2}} \mathbf{U}(x, t) dx = \Delta y \Delta z [\mathbf{f}(\mathbf{U}(x_{i-1/2}, t)) - \mathbf{f}(\mathbf{U}(x_{i+1/2}, t))], \quad (5.47)$$

where dividing Equation (5.47) by the constants  $\Delta y$  and  $\Delta z$  and integration from time  $t_n$  to  $t_{n+1}$  yields

$$\underbrace{\int_{x_{i-\frac{1}{2}}}^{x_{i+\frac{1}{2}}} \mathbf{U}(x, t_{n+1}) dx}_{\mathbf{U}_i^{n+1} \Delta x} = \underbrace{\int_{x_{i-\frac{1}{2}}}^{x_{i+\frac{1}{2}}} \mathbf{U}(x, t_n) dx}_{\mathbf{U}_i^n \Delta x} + \underbrace{\int_{t_n}^{t_{n+1}} \mathbf{f}(\mathbf{U}(x_{i-1/2}, t)) dt}_{\mathbf{F}_{i-1/2}^n \Delta t} - \underbrace{\int_{t_n}^{t_{n+1}} \mathbf{f}(\mathbf{U}(x_{i+1/2}, t)) dt}_{\mathbf{F}_{i+1/2}^n \Delta t}. \quad (5.48)$$

With the average cell values  $\mathbf{U}_i^{n+1}$ ,  $\mathbf{U}_i^n$  and the time-averaged flux integrals  $\mathbf{F}_{i+1/2}^n$ ,  $\mathbf{F}_{i-1/2}^n$ , the short form of the conservation law reads

$$\mathbf{U}_i^{n+1} = \mathbf{U}_i^n - \frac{\Delta t}{\Delta x} (\mathbf{F}_{i+1/2}^n - \mathbf{F}_{i-1/2}^n). \quad (5.49)$$

The time-averaged fluxes  $\mathbf{F}_{i+1/2}^n$ ,  $\mathbf{F}_{i-1/2}^n$  appearing in Equation (5.49) are sometimes called numerical fluxes. However, since no approximation had been made in the derivation, Equation (5.49) is an exact solution of Equation (5.46). The reason why  $\mathbf{F}_{i+1/2}^n$  and  $\mathbf{F}_{i-1/2}^n$  become numerical fluxes, is that the integrands  $\mathbf{f}(\mathbf{U}(x_{i-1/2}, t))$  and  $\mathbf{f}(\mathbf{U}(x_{i+1/2}, t))$  are not known exactly for any time  $t$ , if only the cell average values  $\mathbf{U}_{i-1}^n$ ,  $\mathbf{U}_i^n$ ,  $\mathbf{U}_{i+1}^n$  at time  $t_n$  are stored. Hence, the approximation of the integrand with respect to time lets  $\mathbf{F}_{i+1/2}^n$  become a numerical flux

$$\mathbf{F}_{i+1/2}^n = \frac{1}{\Delta t} \int_{t_n}^{t_{n+1}} [\mathbf{f}(\mathbf{U}(x_{i+1/2}, t_n)) + \mathbf{f}_t(\mathbf{U}(x_{i+1/2}, t_n)) \cdot (t - t_n) + \dots] dt, \quad (5.50)$$

where  $\mathbf{f}(\mathbf{U}(x_{i+1/2}, t_n))$  and  $\mathbf{f}_t(\mathbf{U}(x_{i+1/2}, t_n)) = -\mathbf{f}_{\mathbf{U}}(\mathbf{U}(x_{i+1/2}, t_n)) \mathbf{f}_x(\mathbf{U}(x_{i+1/2}, t_n))$  are derived using the differential equation  $\mathbf{U}_t = -\mathbf{f}_x$  and a spatial approximation based on the cell average values at time  $t_n$ , that determines  $\mathbf{U}(x_{i+1/2}, t_n)$ . Hence, only the spatio-temporal approximation of the flux integrands  $\mathbf{f}(\mathbf{U}(x_{i+1/2}, t))$ ,  $\mathbf{f}(\mathbf{U}(x_{i-1/2}, t))$  determines the behavior and results of Equation (5.49).

For the linear advection equation  $u_t + a u_x = 0$ , given in Equation (5.21), the flux function  $f(u(x, t)) = a u(x, t)$  can be used together with the differential equation to find the time derivatives  $f_t = a u_t = -a^2 u_x$ ,  $f_{tt} = a u_{tt} = a^3 u_{xx}$ , ... for the approximation of the scalar numerical flux

$$F_{i+1/2}^n = a u(x_{i+1/2}, t_n) - \frac{1}{2} a^2 \Delta t u_x(x_{i+1/2}, t_n) + \frac{1}{2} a^3 \Delta t^2 u_{xx}(x_{i+1/2}, t_n) + \dots \quad (5.51)$$

### 5.3.3.1 First Order Upwind Scheme

The finite volume version of the first order upwind scheme uses only the first term of Equation (5.51) and applies the piecewise constant reconstruction in Equation (5.13) to substitute  $u(x_{i+1/2}, t_n)$  with the cell average value  $U_i^n$  in upwind direction

$$F_{i+1/2}^n = a U_i^n, \quad (5.52)$$

where  $a$  was assumed to be positive. For  $a < 0$  the numerical first order upwind flux at the cell boundary  $x_{i+1/2}$  becomes  $F_{i+1/2}^n = a U_{i+1}^n$ . Hence, the direction of spatial discretization depends on the local value of the wave speed  $a$  at the cell boundary. Assuming  $a > 0$  at  $x_{i-1/2}$  gives for the numerical flux  $F_{i-1/2}^n = a U_{i-1}^n$ . Inserting  $F_{i+1/2}^n$  and  $F_{i-1/2}^n$  in the conservation law  $U_i^{n+1} = U_i^n - \frac{\Delta t}{\Delta x} (F_{i+1/2}^n - F_{i-1/2}^n)$  of Equation (5.49) and using the Courant number  $C$  of Equation (5.28) gives

$$U_i^{n+1} = U_i^n - C (U_i^n - U_{i-1}^n). \quad (5.53)$$

Hence, the finite volume first order upwind scheme becomes similar to the finite difference first order upwind scheme of Equation (5.27) if  $a$  is positive at  $x_{i+1/2}$  and  $x_{i-1/2}$ . However, the cell average values  $U_i^n$ ,  $U_{i-1}^n$  are used instead of the points values  $u_i^n$ ,  $u_{i-1}^n$ .

### 5.3.3.2 Second Order Central Scheme

For the second order central scheme, the first and the second term of Equation (5.51) are used. The linear reconstruction of Equation (5.14) can be used to find  $u(x_{i+1/2}, t_n) = U_i^n + (U_{i+1}^n - U_i^n)(x_{i+1/2} - x_i)/(x_{i+1} - x_i)$  for the value at the cell boundary  $x_{i+1/2}$ , and  $u_x(x_{i+1/2}, t_n) = (U_{i+1}^n - U_i^n)/(x_{i+1} - x_i)$  for the space derivative. Similar approximations  $u(x_{i-1/2}, t_n)$  and  $u_x(x_{i-1/2}, t_n)$  can be used to find for the central numerical fluxes

$$F_{i+1/2}^n = a \left( U_i^n + (U_{i+1}^n - U_i^n) \frac{x_{i+1/2} - x_i}{x_{i+1} - x_i} \right) - \frac{1}{2} a^2 \Delta t \frac{U_{i+1}^n - U_i^n}{x_{i+1} - x_i}, \quad (5.54)$$

$$F_{i-1/2}^n = a \left( U_{i-1}^n + (U_i^n - U_{i-1}^n) \frac{x_{i-1/2} - x_{i-1}}{x_i - x_{i-1}} \right) - \frac{1}{2} a^2 \Delta t \frac{U_i^n - U_{i-1}^n}{x_i - x_{i-1}}. \quad (5.55)$$

The neighbors  $U_i^n$ ,  $U_{i+1}^n$  of the cell boundary  $x_{i+1/2}$ , and the neighbors  $U_{i-1}^n$ ,  $U_i^n$  of the cell boundary  $x_{i-1/2}$ , are used independently of the wave speed sign. With the cell size  $\Delta x = (x_{i+1/2} - x_{i-1/2})$  and the cell size ratios  $\chi_R = (x_{i+3/2} - x_{i+1/2})/\Delta x$ ,  $\chi_L = (x_{i+1/2} - x_{i-1/2})/\Delta x$ , the conservation law of Equation (5.49) becomes

$$U_i^{n+1} = U_i^n - C \left[ \frac{(1 - C) U_{i+1} + (\chi_R + C) U_i}{1 + \chi_R} - \frac{(1 - C) U_i + (\chi_L + C) U_{i-1}}{1 + \chi_L} \right], \quad (5.56)$$

where  $C = a \Delta t / \Delta x$  is the Courant number. For equi-sized grid  $\chi_R = \chi_L = 1$ , this becomes the finite volume Lax-Wendroff scheme

$$U_i^{n+1} = U_i^n - \frac{1}{2} C (U_{i+1}^n - U_{i-1}^n) + \frac{1}{2} C^2 (U_{i+1}^n - 2 U_i^n + U_{i-1}^n). \quad (5.57)$$

Hence, for equi-sized grid the finite volume method is identical with the finite difference method of Equation (5.37), but uses the cell average values instead of point values.

### 5.3.3.3 Third Order Upwind-Biased Scheme

In order to derive a third order scheme, all term shown in Equation (5.51) are used. The approximations of  $u(x_{i+1/2}, t_n)$ ,  $u_x(x_{i+1/2}, t_n)$ ,  $u_{xx}(x_{i+1/2}, t_n)$  are derived from Equation (5.20) for a quadratic reconstruction function on equi-sized grid

$$u(x_{i+1/2}, t_n) = \frac{1}{6}(2U_{i+1}^n + 5U_i^n - U_{i-1}^n), \quad (5.58)$$

$$u_x(x_{i+1/2}, t_n) = \frac{1}{\Delta x}(U_{i+1}^n - U_i^n), \quad (5.59)$$

$$u_{xx}(x_{i+1/2}, t_n) = \frac{1}{\Delta x^2}(U_{i+1} - 2U_i + U_{i-1}). \quad (5.60)$$

With the Courant number  $C = a \Delta t / \Delta x$  the numerical flux divided by the wave speed reads

$$\frac{F_{i+1/2}^n}{a} = \frac{1}{6}(2U_{i+1}^n + 5U_i^n - U_{i-1}^n) - \frac{C}{2}(U_{i+1}^n - U_i^n) + \frac{C^2}{2}(U_{i+1} - 2U_i + U_{i-1}). \quad (5.61)$$

Using a comparable equation for  $F_{i-1/2}^n$  gives for the conservation law

$$\begin{aligned} U_i^{n+1} = & \frac{1}{6}(-2C + 3C^2 - C^3)U_{i+1}^n + \frac{1}{6}(6 - 3C - 6C^2 + 3C^3)U_i^n + \\ & \frac{1}{6}(6C + 3C^2 - 3C^3)U_{i-1}^n + \frac{1}{6}(-C + C^3)U_{i-2}^n. \end{aligned} \quad (5.62)$$

This is the same form as it was obtained for the third order finite differenc scheme in Equation (5.45), although volume averages are used here instead of point values. This result is quite estonishing, because the errors of  $u_i^{n+1}$  computed by Equation (5.45) and of  $U_i^{n+1}$  computed by Equation (5.62) are  $\mathcal{O}(\Delta x^4)$ , while according to Equation (5.5), the difference of  $U_i^{n+1}$  to  $u_i^{n+1}$  is  $\mathcal{O}(\Delta x^2)$ . Hence, the difference of a volume average to a point value can be larger, than the discretization error of an accurate numerical scheme.

### 5.3.3.4 High Resolution Scheme

The idea of high resolutions schemes is to combine a low order method with a high order method. Usually, the first order upwind flux is used together with the second order central flux of Lax-Wendroff. Near discontinuities, the solution of the second order central flux tends to overshoots and oscilations, while the first order upwind scheme does not show this phenomenon. In contrast, the first order scheme does not only advect discontinuities, as it would be expected by the analytic solution, but also smears out the jumps as it is done by physical models that include diffusion. However, the high numerical diffusion of the first order scheme makes it sometimes inappropriate for finding smooth solutions. Hence, the basic concept of high resolution schemes is to find a clever switch between an accurate but oscilating high order flux  $F_{i+1/2}^H$ , and an in-accurate but non-oscilating low order flux  $F_{i+1/2}^L$ . The Lax-Wendroff flux on equi-sized grid  $F_{i+1/2}^H = a [U_i^n + \frac{1}{2}(1 - C)(U_{i+1}^n - U_i^n)]$  from

Equation (5.54) is usually combined with the first order upwind flux  $F_{i+1/2}^L = a U_i^n$  from Equation (5.52), to give for the numerical high resolution flux

$$F_{i+1/2}^n = F_{i+1/2}^L + (F_{i+1/2}^H - F_{i+1/2}^L) \phi_{i+1/2}(\theta_i), \quad (5.63)$$

$$\frac{1}{a} F_{i+1/2}^n = U_i^n + \frac{1}{2}(1 - C)(U_{i+1}^n - U_i^n) \phi_{i+1/2}(\theta_i), \quad (5.64)$$

where  $\phi_{i+1/2}(\theta_i)$  is the flux-limiter function, giving the first order upwind scheme for  $\phi_{i+1/2} = 0$ , and the second order central scheme for  $\phi_{i+1/2} = 1$ . The ratio of consecutive gradients

$$\theta_i = \frac{U_i^n - U_{i-1}^n}{U_{i+1}^n - U_i^n} \quad (5.65)$$

is a measure for the smoothness of the solution, and uses the difference of upwind and far-upwind values ( $U_i^n - U_{i-1}^n$ ), and the difference of downwind and upwind value  $U_{i+1}^n - U_i^n$ , respectively. Rewriting gives  $\theta_i = 1 - \frac{U_{i+1}^n - 2U_i^n + U_{i-1}^n}{U_{i+1}^n - U_i^n}$ , where the term  $(U_{i+1}^n - 2U_i^n + U_{i-1}^n) = \Delta x^2 u_{xx}(x_{i+1/2}) - \frac{1}{2} \Delta x^3 u_{xxx}(x_{i+1/2}) + \dots$  is a measure for the curvature and  $(U_{i+1}^n - U_i^n) = \Delta x u_x(x_{i+1/2}) + \frac{1}{24} \Delta x^3 u_{xxx}(x_{i+1/2}) + \dots$  measures the slope at position  $x_{i+1/2}$ . Hence,  $\theta_i \approx 1 - \Delta x \frac{u_{xx}(x_{i+1/2})}{u_x(x_{i+1/2})}$  equals approximately one, if the smoothness criterion  $\Delta x \frac{u_{xx}(x_{i+1/2})}{u_x(x_{i+1/2})} \ll 1$  is fulfilled. It can be expected that  $\phi_{i+1/2}$  should have a value between zero and one, depending on the danger for oscillatory solutions. However, it turns out, that the third order numerical flux obtained in Equation (5.61) gives the Courant-number dependent limiter function

$$\phi_{i+1/2}^{\mathcal{O}(3)}(\theta_i, C) = 1 + \frac{1 + C}{3}(\theta_i - 1), \quad (5.66)$$

with a value of one at  $\theta_i = 1$ , and a slope  $\frac{1+C}{3}$ . In the  $(\theta_i, \phi_{i+1/2})$ -diagram all second order schemes pass the point (1, 1). Hence, the slope must depend on the Courant number to reach third order accuracy. Based on von Neumann and TVD stability analysis, the maximal time step  $C_{max}$  for these methods can be found. Furthermore, the TVD stability criterion allows to find flux limiter function better suited for discontinuities, while the limiter  $\phi_{i+1/2}^{\mathcal{O}(3)}$  is the optimal choice for smooth solutions.

### 5.3.4 Numerical Diffusion

The numerical diffusion of the first order upwind scheme used for the linear advection equation is discussed. The first order scheme can be interpreted as a second order scheme with additional diffusion. In order to find this diffusive expression, the first order scheme is compared with a second order discretization of the advection diffusion equation

$$u_t + a u_x = d u_{xx}. \quad (5.67)$$

The Cauchy Kowalewski time-discretization procedure for the advection diffusion equation substitutes the time derivatives by space derivatives. The advective and

the diffusive Courant number

$$C = \frac{a \Delta t}{\Delta x}, \quad D = \frac{d \Delta t}{\Delta x^2}, \quad (5.68)$$

are used in combination with the first and the second time derivative

$$u_t = -a u_x + d u_{xx}, \quad u_{tt} = a^2 u_{xx} - 2 a d u_{xxx} + d^2 u_{xxxx}, \quad (5.69)$$

to derive for the Taylor series in time  $u_i^{n+1} = u_i^n + u_t \Delta t + \frac{1}{2} u_{tt} \Delta t^2 + \dots$

$$u_i^{n+1} = u_i^n - C \Delta x u_x + \left( \frac{C^2}{2} \Delta x^2 + D \Delta x^2 \right) u_{xx} - C D \Delta x^3 u_{xxx} + \frac{D^2}{2} \Delta x^4 u_{xxxx} + \dots \quad (5.70)$$

For a second order scheme the terms  $\mathcal{O}(\Delta x^3)$  and  $\mathcal{O}(\Delta x^4)$  can be neglected. Applying a second order central discretization gives

$$u_i^{n+1} = u_i^n - C (u_{i+1}^n - u_{i-1}^n) + \frac{C^2}{2} (u_{i+1}^n - 2u_i^n + u_{i-1}^n) + D (u_{i+1}^n - 2u_i^n + u_{i-1}^n), \quad (5.71)$$

where compared to the second order scheme for the advection equation, only the last term stems from the diffusion. The first order upwind scheme  $u_i^{n+1} = u_i^n - C (u_i^n - u_{i-1}^n)$  applied to the advection equation  $u_t + a u_x = 0$  with positive wave speed  $a > 0$ , can also be written as

$$u_i^{n+1} = u_i^n - \frac{C}{2} (u_{i+1}^n - u_{i-1}^n) + \frac{C^2}{2} (u_{i+1}^n - 2u_i^n + u_{i-1}^n) + \frac{C}{2} (1 - C) (u_{i+1}^n - 2u_i^n + u_{i-1}^n), \quad (5.72)$$

where the first three terms are identical with the second order discretization, and the last term is called the numerical diffusion of the first order scheme. Hence, comparing the additional term with the second order advection diffusion approximation, gives  $D = \frac{1}{2} C (1 - C)$  or for the diffusion coefficient

$$d = \frac{1}{2} \frac{\Delta x^2}{\Delta t} \frac{a \Delta t}{\Delta x} \left( 1 - \frac{a \Delta t}{\Delta x} \right). \quad (5.73)$$

Hence, if the advective Courant number  $C = a \Delta t / \Delta x$  fulfills  $0 < C < 1$ , the coefficient of numerical diffusion is always positive for the first order upwind scheme. The diffusive Courant number  $D = \frac{1}{2} C (1 - C)$  reaches its maximum  $D_{max} = 1/8$  at  $C = 1/2$ .

### 5.3.5 Von Neumann Stability

The von Neumann stability analysis discusses how some deviation of the initial data evolves with respect to time. Basically, the analysis only works for linear equations, because then, the difference of the approximated result to the analytic solution can easily be obtained. As a consequence, the time evolution of the approximation error is derived with the same numerical scheme as that for the discussed equation. Applying a spatial wave ansatz for the initial disturbance  $u_\Omega(x) = e^{i\Omega x}$  and the

time-evolution ansatz  $u_\Omega(x, t) = e^{i\Omega x + \beta t}$ , gives for the values in the cell-mid point of an equi-sized grid with distance  $\Delta x$  at time 0 and  $\Delta t$

$$u_{i+1}^n = u_i^n e^{i\omega}, \quad (5.74)$$

$$u_{i-1}^n = u_i^n e^{-i\omega}, \quad (5.75)$$

$$u_{i-2}^n = u_i^n e^{-i2\omega}, \quad (5.76)$$

$$u_i^{n+1} = u_i^n e^{\beta \Delta t}, \quad (5.77)$$

where  $\omega = \Omega \Delta x$  and  $G = e^{\beta \Delta t}$  is the amplification factor.

### 5.3.5.1 First Order Upwind Scheme

Inserting the wave ansatz in the cell mid-point values of the first order upwind scheme for the linear advection equation  $u_i^{n+1} = u_i^n - C(u_i^n - u_{i-1}^n)$  with positive wave speed  $a > 0$ , Equation (5.27) divided by  $u_i^n$  becomes

$$G = 1 - C(1 - e^{-i\omega}) = (1 - C + C \cos \omega) - iC \sin \omega. \quad (5.78)$$

Stability requires that no waves of any length in the initial error will grow with respect to time. Hence, the growth coefficient  $\beta$  must be non-positive or the modulus of the amplification factor  $G$  is not larger than one  $|G| \leq 1$ . The square of the modulus  $|G|^2 = G \cdot G^*$  fulfills the equation  $|G|^2 \leq 1$  if  $|G| \leq 1$  is fulfilled. For the first order upwind scheme  $|G|^2$  becomes

$$|G|^2 = (1 - C + C \cos \omega)^2 + C^2 \sin^2 \omega = 1 + 2C(1 - C)(\cos \omega - 1). \quad (5.79)$$

Because  $-1 \leq \cos \omega \leq 1$  is fulfilled for any value of  $\omega$ , the last bracket is non-positive  $(\cos \omega - 1) \leq 0$ . Hence, the stability condition  $|G|^2 \leq 1$  requires that  $C(1 - C) \geq 0$ , or

$$0 \leq C \leq 1 \quad (5.80)$$

for the first order upwind scheme. Since the time step is limited  $\Delta t \leq \Delta x C_{max}/a$  by the maximal Courant number  $C_{max} = 1$ , the first order upwind scheme is said to be conditionally stable under the condition in Equation (5.80). The stability analysis for the first order upwind finite volume scheme follows the same pattern, but uses volume averages instead of point values. However, the same result is obtained for the time step restriction as for the finite difference scheme.

### 5.3.5.2 Second Order Central Scheme

The Lax-Wendroff or second order central scheme shown in Equation (5.37) for the linear advection equation  $u_i^{n+1} = u_i^n - \frac{1}{2}C(u_{i+1}^n - u_{i-1}^n) + \frac{1}{2}C^2(u_{i+1}^n - 2u_i^n + u_{i-1}^n)$  written with cell mid-point values, gives after inserting the wave ansatz and division by  $u_i^n$  for the amplification factor and its squared modulus

$$G = 1 - \frac{1}{2}C \underbrace{(e^{i\omega} - e^{-i\omega})}_{i 2 \sin \omega} + \frac{1}{2}C^2 \underbrace{(e^{i\omega} - 2 + e^{-i\omega})}_{2 \cos \omega - 2} = 1 + C^2(\cos \omega - 1) - iC \sin \omega, \quad (5.81)$$



$$|G|^2 = [1 + C^2(\cos \omega - 1)]^2 + C^2 \sin^2 \omega, \quad (5.82)$$

$$|G|^2 = 1 + C^2(C^2 - 1)(\cos \omega - 1)^2. \quad (5.83)$$

Since  $C^2(\cos \omega - 1)^2$  is always positive for any  $\omega$  or Courant number  $C$ , the stability condition  $|G|^2 \leq 1$  requires that  $(C^2 - 1) \leq 0$  or

$$0 \leq C \leq 1, \quad (5.84)$$

if  $C$  is assumed to be non-negative. Hence, the second order central scheme has the same maximal Courant number  $C_{max}$  as the first order upwind scheme. The second order central scheme is conditionally stable under the time step restriction  $\Delta t \leq \Delta x C_{max}/a$ . For the finite volume central scheme the same condition  $C_{max} = 1$  is valid.

### 5.3.5.3 Third Order Upwind-Biased Scheme

The von Neumann stability analysis for the third order upwind-biased finite difference scheme in Equation (5.45) or the equivalent third order upwind-biased finite volume scheme in Equation (5.62) is a little more tedious. After some simplification the squared modulus of the amplification factor reads

$$|G|^2 = 1 - \frac{4}{9}C(2 - C - 2C^2 + C^3)[3 + 2C - 2C^2 - 2(1 - C)C \cos \omega] \sin^4(\omega/2). \quad (5.85)$$

The expression  $\sin^4(\omega/2)$  is non-negative for all  $\omega$ . For  $\omega = \pi$  the maximum value  $\sin^4(\pi/2) = 1$  is found. In the limit  $\omega \rightarrow \pi$  the relevant term  $|G|^2$  becomes  $\lim_{\omega \rightarrow \pi} |G|^2 = 1 + \frac{8}{9}C(C + 1)(C + 1/2)(C - 1)(C - 2)(C - 3/2)$ . The function  $C(C + 1)(C + 1/2)(C - 1)(C - 2)(C - 3/2)$  is non-positive in the range

$$0 \leq C \leq 1, \quad (5.86)$$

and turns positive at  $C > 1$ . With Equation (5.86) the stability limit  $|G|^2 \leq 1$  is fulfilled for all values of  $\omega$ . Hence, the third order upwind-biased scheme has the same stability restriction as the first order upwind scheme and the second order central scheme.

### 5.3.6 TVD Stability

The Total Variation Diminishing (TVD) property of Harten [36] gives a condition for the TVD-stability of a combined space-time-discretization with a three-point stencil

$$U_i^{n+1} = U_i^n - c_{i-1/2}(U_i^n - U_{i-1}^n) + d_{i+1/2}(U_{i+1}^n - U_i^n), \quad (5.87)$$

where  $c_{i-1/2}$  and  $d_{i+1/2}$  can depend on the  $U^n$  values. Therefore, methods based on Equation (5.87) are said to be in general non-linear. If the coefficients fulfill the conditions

$$c_{i-1/2} \geq 0 \quad \forall i, \quad (5.88)$$

$$d_{i+1/2} \geq 0 \quad \forall i, \quad (5.89)$$

$$c_{i-1/2} + d_{i+1/2} \leq 1 \quad \forall i, \quad (5.90)$$

the scheme is said to be TVD stable. In his original text Harten [36] uses TVNI (Total Variation Non Increasing) instead of TVD. This terminology is technically correct, because a TVD stable scheme does not exceed the total variation of its initial function. Indeed, a good numerical method applied to the linear advection equation should conserve the initial total variation instead of diminishing it with respect to time. Instead of the total variation defined in Equation (4.38), in TVD schemes the discrete total variation

$$TV = \sum_{i=-\infty}^{+\infty} |u_{i+1} - u_i| \quad (5.91)$$

is non-increasing compared to its initial value. In contrast to the von Neumann stability analysis, the TVD stability criterion is also applicable to non-linear schemes and non-linear partial differential equations. Furthermore, TVD schemes are strictly non-oscillating, and the results will always stay positive if the initial function is positive as well.

### 5.3.7 TVD Flux Limiter

Due to the enormous importance of the TVD condition on the development of numerical schemes, the consequences of this stability criterion on the flux limiter functions  $\phi_{i+1/2}(\theta_i)$  used for the fluxes in Equation (5.64) of high resolution schemes presented in section 5.3.3.4 are briefly discussed. Using  $\theta_i = (U_i^n - U_{i-1}^n)/(U_{i+1}^n - U_i^n)$  and  $\theta_{i-1} = (U_{i-1}^n - U_{i-2}^n)/(U_i^n - U_{i-1}^n)$  the high resolution fluxes located at  $x_{i+1/2}$  and  $x_{i-1/2}$  for the linear advection equation read

$$F_{i+1/2}^n = a U_i^n + \frac{a}{2}(1 - C)(U_{i+1}^n - U_i^n) \phi_{i+1/2}(\theta_i), \quad (5.92)$$

$$F_{i-1/2}^n = a U_{i-1}^n + \frac{a}{2}(1 - C)(U_i^n - U_{i-1}^n) \phi_{i-1/2}(\theta_{i-1}). \quad (5.93)$$

Inserting these into the conservation law  $U_i^{n+1} = U_i^n - \frac{\Delta t}{\Delta x}(F_{i+1/2}^n - F_{i-1/2}^n)$  of a finite volume scheme gives with  $C = a \Delta t / \Delta x$

$$U_i^{n+1} = U_i^n - C \left[ 1 - \frac{1}{2}(1 - C) \phi_{i-1/2} + \frac{1}{2}(1 - C) \phi_{i+1/2} \frac{U_{i+1}^n - U_i^n}{U_i^n - U_{i-1}^n} \right] (U_i^n - U_{i-1}^n). \quad (5.94)$$

Comparison with Harten's three-point stencil in Equation (5.87) shows  $d_{i+1/2} = 0$ . Hence, the condition of Equation (5.89) is fulfilled. The conditions of Equation (5.88) and Equation (5.90) are fulfilled if

$$0 \leq C + \frac{1}{2}C(1 - C) \left( \frac{\phi_{i+1/2}(\theta_i)}{\theta_i} - \phi_{i-1/2}(\theta_{i-1}) \right) \leq 1, \quad (5.95)$$

$$-C \leq \frac{1}{2}C(1 - C) \left( \frac{\phi_{i+1/2}(\theta_i)}{\theta_i} - \phi_{i-1/2}(\theta_{i-1}) \right) \leq 1 - C, \quad (5.96)$$

$$-\frac{2}{1 - C} \leq \frac{\phi_{i+1/2}(\theta_i)}{\theta_i} - \phi_{i-1/2}(\theta_{i-1}) \leq \frac{2}{C}. \quad (5.97)$$

It has to be mentioned, that this is not the only possible choice. Subtracting other values from Equation (5.95) instead of  $C$  is also possible, and leads to other conditions for  $\phi_{i+1/2}(\theta_i)/\theta_i - \phi_{i-1/2}(\theta_{i-1})$ . However, this is the most common procedure to derive TVD flux limiter functions. Furthermore, setting  $\phi_{i+1/2}(\theta_i) = 0$  if  $\theta_i \leq 0$  leads to  $\phi_{i-1/2}(\theta_{i-1}) \leq 2/(1-C)$ , while setting  $\phi_{i-1/2}(\theta_{i-1}) = 0$  if  $\theta_{i-1} \leq 0$  gives  $\phi_{i+1/2}(\theta_i) \leq 2\theta_i/C$ . Since the functions  $\phi_{i+1/2}(\theta_i)$  and  $\phi_{i-1/2}(\theta_{i-1})$  are exchangeable, a flux limiter function has to fulfill the restrictions of both functions. A limiter function that fulfills all the TVD conditions, is the upper bound limiter

$$\phi_{i+1/2}^{\text{UB}}(\theta_i) = \max \left\{ 0, \min \left\{ \frac{2}{C}\theta_i, \frac{2}{1-C} \right\} \right\} = \begin{cases} 0 & : \theta_i < 0 \\ 2\theta_i/C & : 0 \leq \theta_i < C/(1-C) \\ 2/(1-C) & : C/(1-C) \leq \theta_i \end{cases} . \quad (5.98)$$

The upper bound limiter is used to define the TVD-region. Limiter functions that fulfill  $\phi_{i+1/2}(\theta_i) = 0$  for  $\theta_i \leq 0$ , and  $0 \leq \phi_{i+1/2}(\theta_i) \leq \phi_{i+1/2}^{\text{UB}}(\theta_i)$  for  $\theta_i > 0$ , are said to lie inside the Courant number dependent TVD-region, and fulfill the TVD stability criterion. The TVD-region can be used to restrict other numerical schemes, that are not TVD stable. The third order upwind biased limiter function  $\phi_{i+1/2}^{\text{O}(3)}(\theta_i, C)$  of Equation (5.66) intersects with  $2\theta_i/C$  at  $\theta_i = C/(3+C)$  and with  $2/(1-C)$  at  $\theta_i = (4-C)/(1-C)$ . If the upper bound limiter  $\phi_{i+1/2}^{\text{UB}}(\theta_i)$  is used for  $\theta_i \leq C/(3+C)$  and for  $\theta_i \geq (4-C)/(1-C)$ , and the third order limiter  $\phi_{i+1/2}^{\text{O}(3)}(\theta_i, C)$  is used in the range  $C/(3+C) < \theta_i < (4-C)/(1-C)$ , the so-called Arora-Roe limiter [8] is obtained

$$\phi_{i+1/2}^{\text{AR}}(\theta_i, C) = \max \left\{ 0, \min \left\{ \phi_{i+1/2}^{\text{O}(3)}(\theta_i, C), \phi_{i+1/2}^{\text{UB}}(\theta_i, C) \right\} \right\} . \quad (5.99)$$

The idea of using the upper bound limiter to restrict other methods was first presented by Roe and Baines [73]. The Arora-Roe limiter is locally third order accurate near  $\theta_i = 1$ , and it is limited where the TVD stability would be violated. A detailed description of the limiter function  $\phi_{i+1/2}^{\text{AR}}(\theta_i, C)$  is found in Jeng and Payne [41]. Numerical results for the Arora-Roe flux limiter and for the first order upwind scheme are shown in Figure 5.2 for an initial function having a jump at  $x = 0.09$ , and for a initial hump function  $u(x, 0) = \cos^2((x - 0.18)/0.2)$ . The smearing effects of the first order upwind scheme are caused by numerical diffusion, comparable to physical diffusion appearing in the results of Figure 4.1 for the advection-diffusion equation. The Arora-Roe limiter gives much better results. It is only locally third order accurate, but fulfills the requirements of TVD-stability. Outside the third order accurate range for  $\theta_i$  the limiter function falls back to the first order accurate upper bound limiter. As can be seen in investigations by Kemm [42], the Arora-Roe limiter shows the so-called clipping phenomenon. At local extrema, where  $\theta_i \approx -1$  or  $(U_{i+1} - U_i) \approx -(U_i - U_{i-1})$ , the use of the first order upwind scheme  $\phi_{i+1/2} = 0$  leads to a decrease of extrema due to the numerical diffusion. This effect can be seen for all limiter functions where  $\phi_{i+1/2} = 0$  for negative  $\theta_i$ . Non-clipping TVD flux limiters described by Cada and Torrilhon [16] avoid the use of the first order upwind scheme for  $\theta_i < 0$ , and apply a more accurate method near  $\theta_i = -1$ . Skipping the condition  $\phi_{i+1/2} = 0$  for  $\theta_i < 0$  allows to find modified TVD conditions,

where the upper bound value  $2/(1 - C)$  can not be reached with the non-clipping limiters. Numerical tests show, that these limiters slightly improve the behavior near extrema, but decrease the solution quality near discontinuities.

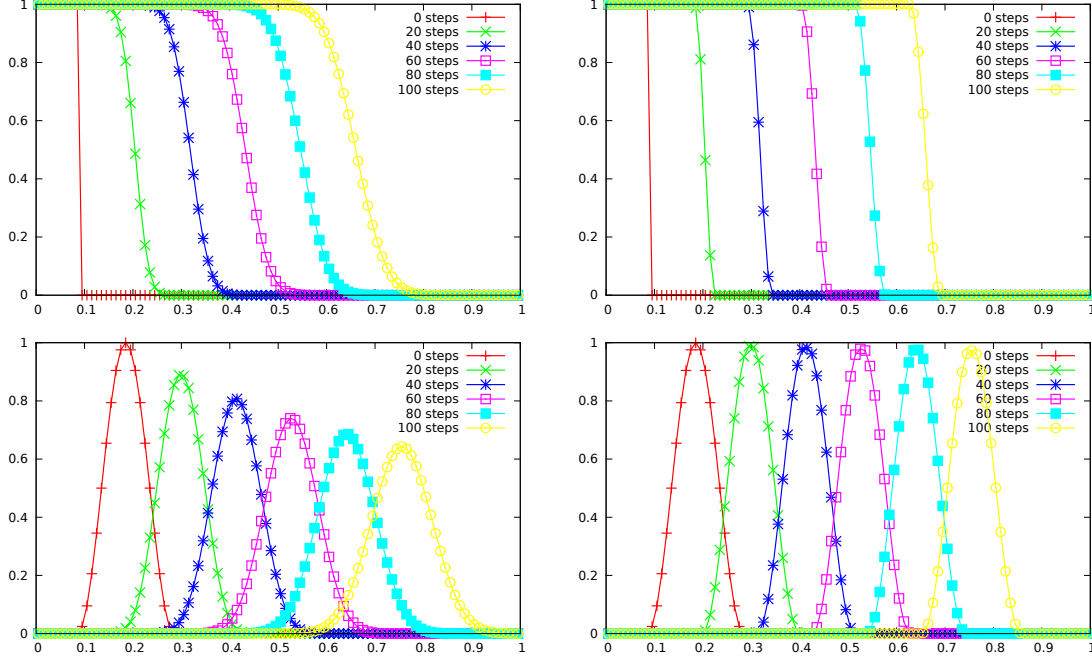


Figure 5.2: Jump (top) and hump (bottom) solution of the linear advection equation  $u_t + a u_x = 0$  solved with the first order upwind scheme (left) and the Arora-Roe flux limiter (right) on a domain with length  $1 m$ . Numerical results are shown after 0 (red), 20 (green), 40 (blue), 60 (magenta), 80 (cyan) and 100 (yellow) timesteps with size  $\Delta t = 1.2 \cdot 10^{-5} s$ . The wave speed  $a = 475 m/s$  and the cell size  $\Delta x = 0.01 m$  give the Courant number  $C = 0.57$ .

Since the TVD-region has been derived with pure mathematical manipulations, the question arises what the upper bound limiter means in terms of numerics, and why it makes sense to stick to that special complicated-looking first order method. While for smooth functions higher order methods improve the results taking more values of the neighborhood into account, this is not the case for discontinuous functions. Avoiding oscillations of higher order schemes near discontinuities is the reason why the TVD stability criterion is preferable to other stability measures.

Indeed, Després and Lagoutière [21] showed, that the upper bound limiter function is optimal for piecewise constant data. Furthermore, it can be shown, that  $\phi_{i+1/2}^{UB}(\theta_i, C)$  gives the optimal numerical flux for the propagation of a single jump in the initial data. This means, that the numerical results of the upper bound limiter for a single jump, will only have one value in-between the upper constant value and the lower constant value of the jump for any time  $t > 0$ . Assume the initial function jumps from  $U_{-\infty}$  for  $x < x^*$  to  $U_{+\infty}$  for  $x > x^*$ . Since a finite volume method only

stores cell average values  $U_i$  of cells with length  $\Delta x$ , the position  $x^*$  of the jump is not stored, as it would be done in a discontinuity tracking method. However, the cell  $\mathcal{C}_i$  where the jump is located, will have some intermediate value  $U_i$  between  $U_{-\infty}$  and  $U_{+\infty}$ , directly related to the jump position.

All the other cell averages left of the cell  $\mathcal{C}_i$  have the constant value  $U_{-\infty}$ , while the cells right of the cell  $\mathcal{C}_i$  have the value  $U_{+\infty}$ . Hence, if the value  $U_i$  is known, the information of the neighbor cells can be used to define the position of the jump  $x^*$  inside the cell. Once this reconstruction with three cell averages is done for every cell, the single discontinuity can be advected according to the analytic solution of the linear advection equation. If the solutions is transformed into a numerical flux, this gives exactly the upper bound limiter function. The re-interpretation of the TVD-region shows, that in contrast to many texts found in the literature, the optimal scheme for a single jump is not the first order upwind scheme. A detailed investigation yields, that the function  $\phi_{i+1/2} = 2\theta_i/C$  is a numerical flux limiter representation of a single jump propagating inside a cell, while the constant  $\phi_{i+1/2} = 2/(1-C)$  gives exactly the downwind flux, avoiding overshoots of the solution. Hence, TVD-fluxes are chosen in-between the upwind flux and the downwind flux. As a consequence, Drikakis et.al.[24] states

- All monotone algorithms are TVD,
- All TVD schemes are monotonicity preserving.

From a philosophical point of view, a shock tracking method computing the position of a jump, is transferred into a shock capturing method computing a numerical flux. Since in the last three decades it was not possible to find a mathematically strict proof for TVD stability in two or three space dimensions, it is maybe possible to find some technique for the reconstruction of discontinuities inside cells based on neighbor values. The numerical fluxes derived from that procedure can then be used to limit the fluxes of any high order method. Similar considerations have recently been developed in the extended finite element method (XFEM), where discontinuities inside an element are allowed, and the smooth functions on both sides of the discontinuity are coupled via jump conditions. The methods have originally been developed for gas dynamics where shocks are expected. However, they can be applied e.g. to Stefan problems, where the position of the discontinuity is part of the solution.

The result found by Goodman and LeVeque [31], that TVD-schemes in two space dimensions are at most first order accurate expect for trivial cases, is not very encouraging. It can not be expected to derive accurate results, if a very sophisticated TVD-scheme developed for one-space dimension is applied to a complex three dimensional flow situation. Therefore, the additional accuracy of three dimensional TVD-like schemes must be questioned, compared to the much more simpler first order upwind schemes. In Chapter 6, where solvers for the three dimensional Euler equations are presented, the discussion is focused on the properties of first order

methods. Although these methods are not that accurate as higher order methods, the numerical diffusion increases the robustness of the schemes, especially for complex flow situations. However, even the solutions of some first order upwind schemes can lead to unphysical results. The reason is the flexibility of choosing the strength of numerical diffusion in different space directions. Some aspects of the so-called multidimensional Riemann-Solver debate are highlighted in Chapter 6.

# Chapter 6

## Numerical Euler-Equation Solver

For the Euler equations in three space dimensions derived in section 3.2.2, special numerical methods exist, that consider the hyperbolic character of the equations, and some of them allow to solve discontinuous solutions, that may appear at high Mach number flows. An overview of methods used for the computation of gas dynamics is given in Laney [48]. Denoted in cartesian coordinates  $x, y, z$ , the differential form of the transport equations for mass, momentum and energy reads

$$\frac{\partial}{\partial t} \mathbf{U} + \frac{\partial}{\partial x} \mathbf{f}^{(x)}(\mathbf{U}) + \frac{\partial}{\partial y} \mathbf{f}^{(y)}(\mathbf{U}) + \frac{\partial}{\partial z} \mathbf{f}^{(z)}(\mathbf{U}) = \mathbf{0}, \quad (6.1)$$

where the flux vectors  $\mathbf{f}^{(x)}$ ,  $\mathbf{f}^{(y)}$ ,  $\mathbf{f}^{(z)}$  in different space directions

$$\mathbf{U} = \begin{bmatrix} \rho \\ \rho u \\ \rho v \\ \rho w \\ E \end{bmatrix}, \quad \mathbf{f}^{(x)} = \begin{bmatrix} \rho u \\ \rho u^2 + p \\ \rho u v \\ \rho u w \\ (E + p) u \end{bmatrix}, \quad \mathbf{f}^{(y)} = \begin{bmatrix} \rho v \\ \rho u v \\ \rho v^2 + p \\ \rho v w \\ (E + p) v \end{bmatrix}, \quad \mathbf{f}^{(z)} = \begin{bmatrix} \rho w \\ \rho u w \\ \rho v w \\ \rho w^2 + p \\ (E + p) w \end{bmatrix}. \quad (6.2)$$

depend on the state-variables  $\rho$ ,  $U = \rho u$ ,  $V = \rho v$ ,  $W = \rho w$ ,  $E = \rho [e + (u^2 + v^2 + w^2)/2]$  collected in the state vector  $\mathbf{U}$ , and the thermodynamic pressure  $p$ . In order to close the system of equations, a material equation describing the dependency of the pressure  $p = p(\rho, e)$  on the density  $\rho$  and the specific inner energy  $e$  is required. For ideal gas with constant specific heats ( $e = c_v T$ ) the equation of state given in Equation (3.12) can then be expressed in terms of the state vector components

$$p = \frac{\mathcal{R}}{\mathcal{M}} \rho T = \frac{\mathcal{R}}{\mathcal{M} c_v} \rho e = (\gamma - 1) \left[ E - \frac{1}{2} \rho^{-1} (U^2 + V^2 + W^2) \right]. \quad (6.3)$$

and the ratio of heat capacities  $\gamma = c_p/c_v$ . Hence, the flux function in  $x$ -direction denoted in state-variables reads

$$\mathbf{f}^{(x)} = \begin{bmatrix} U \\ \frac{1}{2}(3 - \gamma)\rho^{-1}U^2 - \frac{1}{2}(\gamma - 1)\rho^{-1}(V^2 + W^2) + (\gamma - 1)E \\ \rho^{-1}UV \\ \rho^{-1}UW \\ -\frac{1}{2}(\gamma - 1)\rho^{-2}(U^3 + UV^2 + UW^2) + \gamma\rho^{-1}UE \end{bmatrix}. \quad (6.4)$$

Similar expression can be found for the fluxes  $\mathbf{f}^{(y)}$  and  $\mathbf{f}^{(z)}$  using the rotational invariance theorem presented in section 4.2.1. Since Equation (4.7) is fulfilled for the Euler equations, the fluxes in any direction can be derived based on the flux vector  $\mathbf{f}^{(x)}$  and the direction vector  $\mathbf{n}$ .

## 6.1 Godunov Method

A successful method to find approximate solutions to the Euler equations that also can tackle the difficulties with discontinuities was presented by Godunov [30]. The fundamental idea is to use a piecewise constant reconstruction of the cell average values, demonstrated for a one-dimensional situation in Figure 5.1. In general, cells are subdivisions of space, and the cell boundary of a certain cell is partitioned in so-called faces. Every face of the cell boundary has contact to two neighbor cells. After cell average reconstruction, the two neighbor cells to a cell face have different constant values of their unknown variables, that jump at the cell boundary. This discontinuous situation is referred to as Riemann problem. Depending on the values of density, velocity and pressure in both neighbor cells, the Riemann problem for the Euler equations can have different solutions. Usually a Riemann problem creates discontinuous solutions like shocks and contact discontinuities described by the Rankine-Hugoniot conditions of Equation (3.26), and continuous solutions with constant entropy, that are called rarefaction waves. Finding the exact solution for the Riemann problem of the Euler equations requires an iterative procedure, that can be computationally time consuming. Therefore, the exact Riemann solver proposed by Godunov [30], may be substituted by an approximate Riemann solver. Methods that do not solve the Riemann problem exactly are called approximate Riemann solvers, or Godunov-Type methods. They are commonly preferred if the flow is purely subsonic and no discontinuity is expected. Approximate Riemann solvers also work very well if the flow is mainly subsonic, and the shocks in the supersonic zones are weak. However, if contact discontinuities are expected, e.g. at the phase changing zone in multiphase flows, some approximate Riemann solvers may be to inaccurate.

## 6.2 Godunov-Type Methods

Godunov-type Methods use the same in-cell reconstruction methodology as the Godunov method, but solve the Riemann problem at the cell boundaries approximately. An overview of different methods is given in Toro [81]. Basically, two different concepts for approximate Riemann solver can be defined

- Flux Vector Splitting (FVS),
- Flux Difference Splitting (FDS).

An explanation of the flux vector splitting method developed by van Leer [83] can be found in Hirsch [38], [39]. The flux difference splitting method developed by Roe



[70], [71], [72] usually gives better results as the FVS method, but it is a little bit more expensive. Since the Roe method is used within the present work to solve the flow inside a reciprocating compressor, its derivation is discussed in more detail. The Roe method is based on a wave decomposition of locally linearized Euler equations.

It may be worth to mention, that simpler numerical schemes can be derived from the Roe method. A method that considers only the largest eigenvalues of the linearized system was presented by Rusanov [76]. The Rusanov method, nowadays referred to as a local Lax Friedrichs scheme, had been developed a long time before Roe came up with his idea. A scheme that used two eigenvalues of the Roe method is the Harten-Lax-van Leer (HLL) Riemann solver [37]. The scheme neglects the contact discontinuity and substitutes the rarefaction wave by a shock wave. The HLLC Riemann solver (C stands for contact discontinuity) developed by Toro et al. [82] also considers the contact discontinuity. If contact discontinuities are expected, e.g. in multi-phase flows, the HLLC solver gives much better results as the HLL method. However, the numerical diffusion of HLLC is still larger than that of the Roe method.

Although the Roe scheme is said to be the most accurate approximate Riemann solver, it can not be recommended for any situation without care. Quirk [65] demonstrates, how Godunov-type schemes can fail quite spectacularly on occasions, although they are often held up to be models of robustness. Some of the presented failures in [65] are expansion shocks, negative internal energies, slowly moving shocks, the carbuncle phenomenon when the grid is aligned with shocks, kinked Mach stems and odd-even decoupling. To overcome such failings Quirk [65] proposes to employ the HLLE Riemann solver of Einfeldt et al. [26], or an adaptive Riemann solver, being some combination of two methods. The HLLE scheme of Einfeldt [25] preserves the positivity of the scheme near low densities, and can be used for waves propagating into almost vacuum. However, the HLLE solver as a stand alone will not have the same accuracy as the Roe scheme. A class of rotated-hybrid Riemann solvers had been presented by Nishikawa and Kitamura [61]. Recently, Ren [67] has demonstrated how a 2-dimensional Roe Riemann solver can avoid many of the shortcomings mentioned above, if the direction of the wave decomposition is based on local flow properties. Since solution-aligned rotated Riemann solver are more cumbersome and not well understood in 3-dimensions, the implementation in the present code follows the concept of the so-called grid-aligned rotated Riemann solver.

### 6.3 Roe Method

The Roe method for computing the numerical fluxes at cell boundaries is used for arbitrary shaped cells with boundaries that are allowed to move. As shown in Equation (4.3), a finite volume method uses the projection of the flux tensor onto the normal  $\mathbf{n}$  of the surface to compute the numerical flux through the boundary of the control volume based on the state-vectors of the cell neighbors. In case of a one-dimensional situation all cell boundary normal vectors  $\mathbf{n}$  can be thought

co-linear with the direction vector  $\mathbf{x}$  of the coordinate  $x$ . Figure 6.1 illustrates a one-dimensional situation, where the left cell with state vector  $\mathbf{U}_L$  and the right cell with state vector  $\mathbf{U}_R$  share a boundary perpendicular to the  $x$ -direction that is allowed to move with the grid velocity  $\dot{x}$  in  $x$ -direction. For the three-dimensional case the face normal vector  $\mathbf{n}$  at every cell boundary is used instead of the  $x$ -direction.

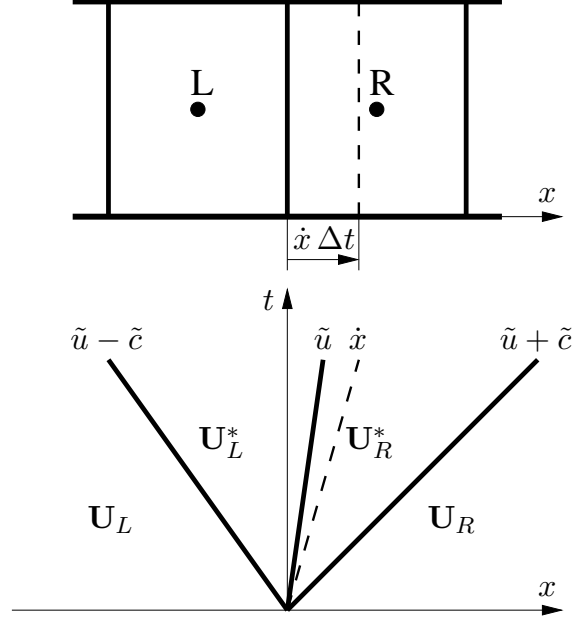


Figure 6.1: Two cells with state vectors  $\mathbf{U}_L$ ,  $\mathbf{U}_R$  sharing a cell boundary that moves with speed  $\dot{x}$  in its normal direction. The Roe method uses a wave decomposition to compute the intermediate state vectors  $\mathbf{U}_L^*$ ,  $\mathbf{U}_R^*$  and the numerical flux through the moving cell boundary.

A grid-aligned rotated Riemann solver rotates the neighbor cell average values in the direction  $\mathbf{n}$  of the shared face, before it is used to compute the numerical fluxes. According to Equation (4.7), a rotation of the state vector  $\mathbf{T}\mathbf{U}$  based on the transformation matrix  $\mathbf{T}$  given in Equation (4.6) can be applied to find the flux vector  $\mathbf{f}$  in the direction  $\mathbf{n}$  using  $\mathbf{f}^{(x)}$ . If the cell boundary moves with speed  $\dot{x}$  in the direction of its normal, the numerical flux scheme has to consider the motion additionally to the non-moving numerical flux. This Arbitrary Lagrangian Eulerian (ALE) approach derived in Equation (3.8) allows more flexibility in the choice of mesh motion. It can be expected, that the approximate solution of the Riemann problem, producing the intermediate states  $\mathbf{U}_L^*$  and  $\mathbf{U}_R^*$ , is not effected by the motion of the boundary moving with speed  $\dot{x}$ . Therefore, the first step is to solve the Riemann problem in the same way as it is done for a non-moving case. The mesh motion  $\dot{x}$  then adds some extra terms depending on the local solution as described in section 6.3.1. In order to find an approximate solution of the non-moving Riemann problem, the Roe flux vector difference method is applied in the direction of the face normal

$$\mathbf{f}_R - \mathbf{f}_L = \mathbf{A}(\tilde{\mathbf{U}}) \cdot (\mathbf{U}_R - \mathbf{U}_L) \quad (6.5)$$

where  $\mathbf{U}_L$ ,  $\mathbf{U}_R$  and  $\mathbf{f}_L$ ,  $\mathbf{f}_R$  are rotated state and flux vectors, and  $\mathbf{A}(\tilde{\mathbf{U}}) = \partial \mathbf{f}(\tilde{\mathbf{U}}) / \partial \mathbf{U}$  is the Jacobi matrix of the so-called Roe-averaged state vector  $\tilde{\mathbf{U}}$ . Equation (6.5) is used to determine  $\mathbf{A}(\tilde{\mathbf{U}})$ . A detailed description how Equation (6.5) is derived and how it is solved for the Euler equations can be found in appendix A.

The Roe method selects the numerical flux  $\mathbf{F}_{\text{nonmoving}}$  in the direction of the face normal  $\mathbf{n}$  for a non-moving grid

$$\mathbf{F}_{\text{nonmoving}} = \begin{cases} \mathbf{f}_L & : (\tilde{u} - \tilde{c}) > 0 \\ \mathbf{f}_L + \mathbf{A}(\tilde{\mathbf{U}}) \cdot (\mathbf{U}_L^* - \mathbf{U}_L) & : \tilde{u} > 0 \\ \mathbf{f}_L + \mathbf{A}(\tilde{\mathbf{U}}) \cdot (\mathbf{U}_R^* - \mathbf{U}_L) & : \tilde{u} < 0 \\ \mathbf{f}_R & : (\tilde{u} + \tilde{c}) < 0 \end{cases} \quad (6.6)$$

depending on the size of the eigenvalues  $(\tilde{u} - \tilde{c})$ ,  $\tilde{u}$ ,  $(\tilde{u} + \tilde{c})$  of the Jacobi matrix. In appendix A.4 the intermediate state vectors  $\mathbf{U}_L^*$  and  $\mathbf{U}_R^*$  are derived, based on the eigenvector decomposition.

### 6.3.1 Numerical Flux on Moving Meshes

In order to consider the effects of a moving mesh, the numerical flux for a non-moving mesh  $\mathbf{F}_{\text{nonmoving}}$  must be modified, following the idea of the Arbitrary Lagrangian Eulerian (ALE) approach derived in Equation (3.8). According to the local circumstances at a cell boundary shown in Figure 6.1, the ALE numerical flux  $\mathbf{F}$  at a cell face becomes

$$\mathbf{F} = \begin{cases} \mathbf{F}_{\text{nonmoving}} - \dot{x} \mathbf{U}_L & : \dot{x} < (\tilde{u} - \tilde{c}) \\ \mathbf{F}_{\text{nonmoving}} - \dot{x} \mathbf{U}_L^* & : \dot{x} \leq \tilde{u} \\ \mathbf{F}_{\text{nonmoving}} - \dot{x} \mathbf{U}_R^* & : \dot{x} > \tilde{u} \\ \mathbf{F}_{\text{nonmoving}} - \dot{x} \mathbf{U}_R & : \dot{x} > (\tilde{u} + \tilde{c}) \end{cases} \quad (6.7)$$

where  $\dot{x} = \dot{\mathbf{x}} \cdot \mathbf{n}$  is the velocity of the moving cell boundary in the direction of its normal. Hence, the additional term depending on the mesh motion allows to move the mesh in an arbitrary way, without losing the advantage of a numerical flux and the idea of conservation within a finite volume method. It may be noticed, that the ALE flux formulation, although demonstrated herein only for the Roe method, can be used in the same way for any kind of approximative Riemann solver as well.

This concept is very useful especially for the mesh inside the cylinder domain of a reciprocating compressor. The speed of the piston can be used as a reference speed for the mesh. Right at the piston, the mesh velocity has to be identical with the time-dependent piston velocity, while it may decrease linearly with increasing distance to the piston, and finally becomes zero at the non-moving cylinder head. As a consequence, it is possible to use cells having equal height along the cylinder axis. Hence, cells with very small size can be avoided, and the timestep size for an explicit time integration scheme may be chosen in a reasonable manner.

## 6.4 Mesh Strategy

### 6.4.1 Moving Structured Cylinder Mesh

The cylinder geometry, sketched in Figure 2.2, consists of a circular cylinder with diameter  $d_P$  and height  $z_{min} + z_P(\varphi)$ , where  $z_P(\varphi)$  given in Equation (1.1) is a time-dependent function, representing the piston motion. Basically, the mesh on the cylinder geometry is structured, i.e. every mesh node position can be accessed by indices  $i, j, k$ . The mesh node distribution is based on the mesh of a cuboid, that is deformed to give the mesh of a circular cylinder. The parameter  $n_1$  controls how many cells are used along the piston radius  $r_P = d_P/2$ , while the parameter  $n_3$  controls the number of cells in axial direction for  $z_P(\varphi) = 0$ . The parameter  $n_2$  allows to eventually control the number of cells on a piston rod with radius  $r_R = d_R/2$ . However, the ability for considering a general piston rod is not fully implemented in the code yet. In Figure 6.2 the cut through the cylinder mesh is sketched, showing the piston together with a piston rod and the mesh inside the cylinder. While  $n_3$  cells are used in axial direction when the cylinder height is  $z_{min}$ , the number of cells in  $z$ -direction increases until the height reaches the value  $z_{min} + 2r$ , where  $r$  is the crank radius. In the same fashion, the number of cells reduces to  $n_3$ , if the cylinder height reaches the value  $z_{min}$  again. Because the height of the cylinder changes dramatically with respect of time, a special routine is necessary to handle the mesh in axial direction. In order to reduce the complexity of this routine, all cells in  $z$ -direction have the same height, based on the optimal cell height  $\Delta z_{opt} = \Delta z_{opt}(\Delta z_{init}, \bar{\rho})$ , that is determined by the initial cell height  $\Delta z_{init} = z_{min}/n_3$ , and is slightly modified during run by a function depending on the average density  $\bar{\rho} = m/V$  inside the compressor, where  $m$  is the mass contained in the compressor, and  $V$  is the volume of the complete domain, including cylinder and valve pockets. The  $\bar{\rho}$ -dependency of the function  $\Delta z_{opt}$  allows to avoid the appearance of too many cells in axial direction when the cylinder has its maximal extension in  $z$ -direction.

Furtunately, the cylinder mesh in the  $x, y$ -plane needs no modification with respect to time. Therefore, it makes sense to create a non-uniform mesh distribution in the piston plane, allowing cells of different size. Usually, the cell size measure  $r_P/n_1$  is larger than the initial cell height  $z_{min}/n_3$  in axial direction. Since the valve pockets are located near the cylinder circumferential walls, the cell size there can be reduced using so-called cell size grading. The mesh refinement by grading allows a better resolution of the connection to the meshes of the valve pockets, see e.g. Figure 6.4. In the implemented code, a parameter  $0 \leq \text{grading}_P \leq 1$  allows to modify the cell size near the diameter  $d_P$ , where a value 0 would result in an equi-distant mesh node distribution along the cylinder radius, and a value 1 would give a cell size of zero close to the circumferential cylinder walls. For  $n_1 = 15$ , setting  $\text{grading}_P = 0.99$  is not problematic. Anyway, in cases where  $n_1 \gg 15$  it is recommended to reduce the value of  $\text{grading}_P$  slightly.

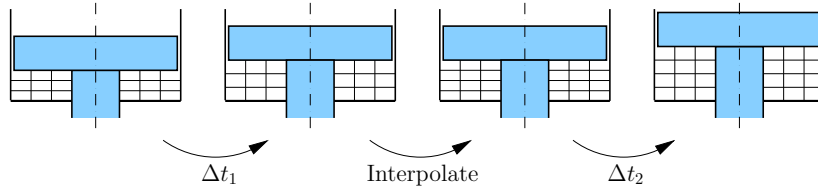


Figure 6.2: Mesh strategy for the moving cylinder mesh: three cells in axial direction at time  $t$  (left), three stretched cells in axial direction after solving the flow with timestep size  $\Delta t_1$  (mid-left), interpolation of the flow solution at time  $t + \Delta t_1$  onto a mesh with four cells in axial direction without solving the flow (mid-right), four stretched cells in axial direction after solving the flow with timestep size  $\Delta t_2$  (right).

In Figure 6.2 the mesh strategy is illustrated for the moving cylinder mesh. Starting at time  $t$ , a mesh with a certain number of cells in axial direction (e.g. three) is shown. If the cell heights in axial direction at time  $t$  are not too large compared to the optimal cell height  $\Delta z_{opt}$ , the cells are simply stretched according to a spring-model during a run of the flow solver with timestep size  $\Delta t_1$ . This is possible, because the ALE technique allows to include the velocity of the cell boundaries  $\dot{x}$  at time  $t$ . This mesh velocity is zero at the cylinder head, and increases linearly in axial direction to the instantaneous piston velocity  $v_P(\varphi)$  at position  $z_{min} + z_P(\varphi)$ . After that, the flow solution and the mesh node positions are given at time  $t + \Delta t_1$ . Note, that the linearly distributed mesh velocity lets all mesh nodes arrive on equi-distant positions again.

At this point in time it is checked, if it is possible to increase the cell number in axial direction, without violating the optimal cell size criterion. If the number of cells in axial direction can be increased (e.g. to four), an interpolation routine maps the solution at time  $t + \Delta t_1$  onto a mesh with more cells, without moving the mesh or running the flow solver. In order to have a conservative interpolation method, a piecewise constant reconstruction of cell average values as shown in Figure 5.1 is applied on the mesh with the original number of cells (e.g. three). After that, all the piecewise constant functions in  $z$ -direction are re-sampled onto the new mesh consisting of more cells, by building the cell averages within the cell boundaries of the new mesh. At the end of this process, the cell average values at time  $t + \Delta t_1$  are given on a mesh with one more cell in axial direction.

Now that all the required data is given to perform a new time step, the flow solver can run a timestep with size  $\Delta t_2$ , and the procedure described herein can start again. Note, that in general the interpolation routine allows to map on any new mesh, independent of the number of cells in axial direction before and after the interpolation. Therefore, the same strategy can be used to decrease the number of cells, if the cylinder height is reducing. Finally it can be stated, that the requirement of increasing or reducing the number of cells in  $z$ -direction is the main reason for choosing a structured mesh inside the cylinder.

### 6.4.2 Non-Moving Unstructured Valve Pocket Mesh

The complex geometric shape of the valve pockets consisting of a cone cut by a cylinder, does not allow to easily use a structured mesh. Therefore, an unstructured tetrahedral mesh is preferred for the pockets. One advantage of the valve pocket mesh is that it is not moving. As a consequence, no re-meshing is required, and the determination of the connectivity of mesh nodes, faces and volumes only needs to be done once. Based on some classical tetrahedral meshing tool (e.g. NETGEN), the additional required connectivity information necessary for the application of the finite volume method is stored in a self-developed file format with extension .msh. This file format also stores different types of boundaries, that represent the functionality of the valve pockets surface mesh, shown in Figure 6.3.

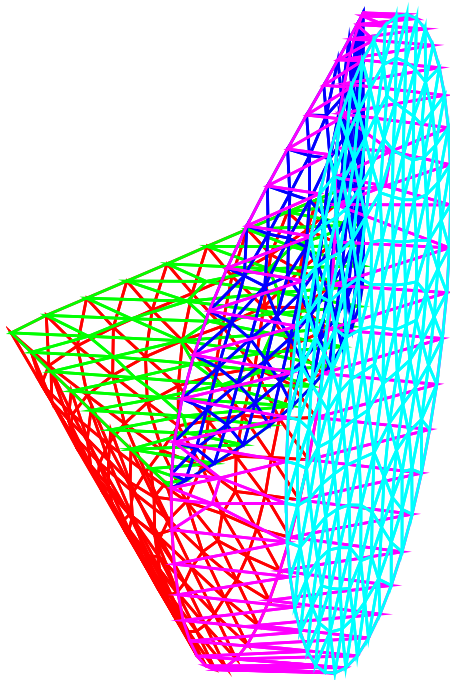


Figure 6.3: Typical surface mesh of the non-moving valve pocket with different types of faces: wall of the cone shaped scallop (red), interface to the cylinder domain at head (green), interface to the cylinder circumferential face (blue), wall of the cylindrical pocket part (magenta), connection to the valve (cyan).

For the surface mesh of the valve pocket illustrated in Figure 6.3, four distinct types of boundary conditions are available:

- wall
- connection to a suction valve or a discharge valve
- interface to the cylinder head
- interface to the cylinder circumferential surface

The boundary condition on the wall is comparable to that on the cylinder mesh, and does not allow any flow of mass through the surfaces declared as walls. Of course, for non-moving walls, the flow of energy through the wall is also zero, while a force acting on the walls is allowed.

The boundary condition that connects the surface mesh to a suction valve or discharge valves is described in detail in section 6.6. Basically, a local mass flow through every triangular face with boundary condition valve is computed based on Equation (3.37), where the effective flow cross section  $\phi_2$  in this formula depends on the valve plate lift, see Equation (2.6). However, finding numerical boundary conditions at valve-boundaries for the flow of momentum and the flow of energy is not trivial. Simple methods that just extrapolate the solution inside the domain to the boundary, as described in Hirsch [39], do not seem to work in some situations. Anyway, it was not possible to detect a specific reason for the dysfunction of that concept. On the other hand, Hirsch [39] also proposes a more complex boundary condition treatment based on a decomposition in characteristics, if problems are to be expected with the extrapolation technique. Therefore, in section 6.6 a numerical boundary treatment based on the Godunov method is presented. While for the suction valve described in section 6.6.1, this still results in an iterative procedure that also requires an initial guess, for a discharge valve an analytic solution to the appearing system of Rankine-Hugoniot conditions can be found using the solutions of cubic equations, see section 6.6.2.

The boundary types having either an interface to the cylinder head or to the cylinder circumferential surface, are the most sophisticated ones. While the interface connection to the cylinder head has to deal with a distorted quadrilateral mesh, the connection to the cylinder circumferential surface is curved, and the intersection of triangular and quadrilateral meshes needs to be computed in every timestep. Therefore, it is required to implement a procedure that is computationally efficient. The interface coupling method is described in section 6.4.3.

### 6.4.3 Interface Coupling Method

The conservative interface coupling is a convenient way to directly use the finite volume method for two non-conforming meshes, that geometrically share an area in space. In case of the reciprocating compressor, the tetrahedral mesh for the valve pockets needs to be connected to the hexahedral mesh of the cylinder. Hence, on the cylinder head and on the cylinder circumferential surface, the surface triangles of the valve pocket meshes have contact to the surface quadrilaterals of the cylinder mesh. Figure 6.4 shows the cylinder head ( $z = 0$ ), having a planar interface zone shared by two surface meshes made of quadrilateral and triangles, respectively.

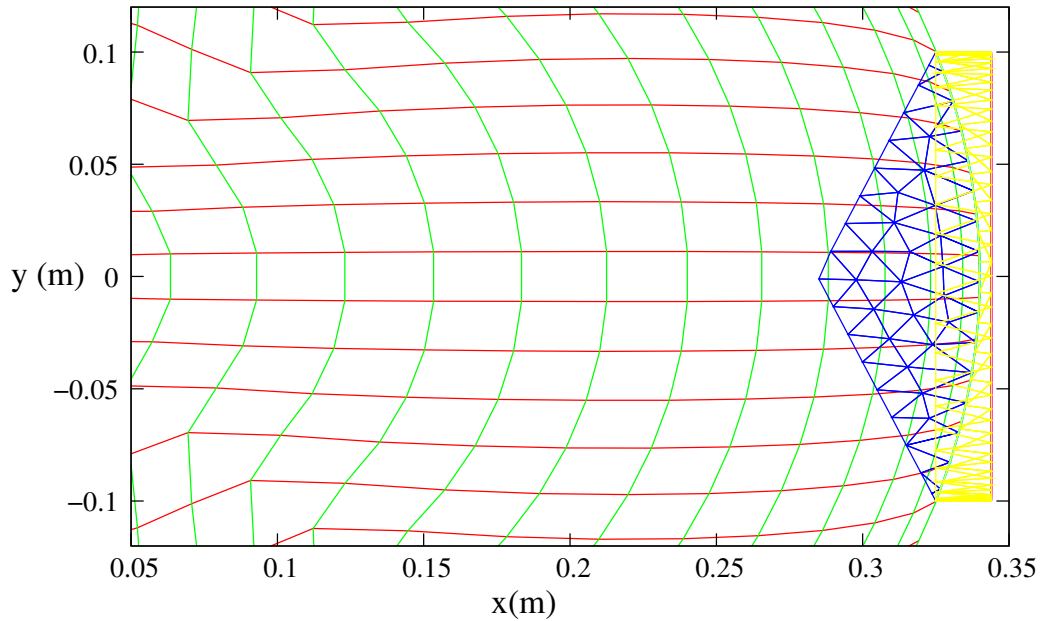


Figure 6.4: Interface coupling at the cylinder head: valve pocket surface triangles (blue) used for the head-interface, and cylinder quadrilaterals made of red and green lines.

In the situation shown in Figure 6.4, some parts of the cylinder head area that originally have a wall boundary condition, will automatically change the boundary condition to internal, where the interface routine detects intersection with the surface mesh of the valve pocket. For the cylinder head interface the triangular surface mesh will always be an internal zone, whereelse at the cylinder circumferential zone the interface connection can bring up internal and wall boundary conditions, due to the moving piston.

In order to derive a conservative method, the numerical fluxes of mass, momentum and energy leaving the cylinder mesh, have to enter the connected valve pocket mesh with the same strength. This property can be achieved, if a numerical flux entering a face of a cell at the interface zone, is the sum of single numerical fluxes through partitions of the face, called fluxes through facets. The time-evolution of mass, momentum and energy of the cells adjacent to the interface is then accomplished by the numerical fluxes through faces that are not part of the interface (internal faces), and by numerical fluxes through one or more facets that are part of the interface. Hence, it can be expected, that the sum of facet fluxes entering or leaving every interface neighbor cell, has the same accuracy as the flux through a single face would have.

In other words, before the finite volume methods and its numerical flux procedure can be applied, the intersection of the surface triangle mesh with the surface quadrilateral mesh needs to be computed. Hence, in order to derive the interface



facets, all the triangles of the valve pocket surface mesh and all the quadrilaterals of the cylinder surface mesh are decomposed into a a priori unknown number of polyhedra, beeing the result of that intersection. Every single polyhedron is then part of a triangle and a quadrilateral, respectively. Recently, Fahs [27] identified five possible configurations for the intersection of triangles with convex quadrilaterals, giving polyhedra with either three, four, five, six or seven edges. Once the number of edges and the positions of the intersection points of every polyhedron are known, the area of every polyhedron can be computed easily by decomposing it into single triangles. It is also not difficult to compute the bary-centers of the polyhedras, eventually required for a second order finite volume method. However, for a first order finite volume method, the numerical flux computation only requires the area and its unit normal vector, here taken in the area center.

At the cylinder head interface the zonal connection is a planar face. Hence, no problem occurs because of tolerance issues on eventually non-planar interfaces. However, at the cylinder circumferential zone, the interface has the shape of a circular cylinder. Since the interface procedure has to work for any position of the piston, and independent of the angular location of the valve pockets, it is recommended to project the nodes of both meshes related to the interface onto a local cylinder coordinate system, and run the intersection procedure in the axial and azimuthal coordinates. A transformation back in the original cartesian coordinate system is straight forward. The numerical flux computation can then be performed in the same fashion as it is done for internal faces of cells. Each polyhedral shaped facet of an interface exactly has one hexahedral neighbor cell, and one tetrahedral neighbor cell, used for piecewise constant reconstruction of cell data. From an code implementation point of view, finding the correct number of the adjacent cell on an unstructured grid is the most difficult part of the interface routine. In section 7.3.1 the mass conservation property of the method will be demonstrated in Figure 7.2.

## 6.5 Positivity Criterion

Some physical quantities, e.g. the density  $\rho$  or the temperature  $T$ , require to have a positive value. Therefore it makes sense to ask, if a numerical method guarantees that some quantities will stay positive after performing a small time step  $\Delta t$ , if their values have been non-negative before. Since the components of a velocity vector can have either positive or negative values, the momentum equations can not be used to find any restriction for the time step. But, for the equations of mass and energy transport the positivity requirement is an issue. Since the positivity of the energy equation is usually difficult to analyse, the continuity equation  $\rho + (\rho u)_x + (\rho v)_y + (\rho w)_z = 0$  is used to find a restriction for the time step size. Of course, this restriction depends on the grid and the discretization used to find an approximate solutions. For simplicity, the velocity vector is assumed to be constant  $\mathbf{u} = \text{const}$ . Then, the continuity equation reads

$$\rho + u \rho_x + v \rho_y + w \rho_z = 0. \quad (6.8)$$

The equation may be solved on a regular structured grid consisting of hexahedral cells with dimensions  $\Delta x$ ,  $\Delta y$ ,  $\Delta z$ . A cell with indices  $(i, j, k)$  shares six surfaces with six neighbor cells having the indices  $(i+1, j, k)$ ,  $(i-1, j, k)$ ,  $(i, j+1, k)$ ,  $(i, j-1, k)$ ,  $(i, j, k+1)$ ,  $(i, j, k-1)$ . In order to discuss the positivity of a numerical scheme, the density values of the neighbor cells at time  $t_n$  are set to  $\rho_{i+1}^n = \rho_{i-1}^n = \rho_{j+1}^n = \rho_{j-1}^n = \rho_{k+1}^n = \rho_{k-1}^n = 0$ , while the density of the cell  $(i, j, k)$  is  $\rho^n > 0$ . A finite volume discretization of the equation for the cell with volume  $V = \Delta x \Delta y \Delta z$  reads

$$V \frac{\rho^{n+1} - \rho^n}{\Delta t} = F_{i-\frac{1}{2}}^{(x)} A_{i-\frac{1}{2}} + F_{j-\frac{1}{2}}^{(y)} A_{j-\frac{1}{2}} + F_{k-\frac{1}{2}}^{(z)} A_{k-\frac{1}{2}} - F_{i+\frac{1}{2}}^{(x)} A_{i+\frac{1}{2}} - F_{j+\frac{1}{2}}^{(y)} A_{j+\frac{1}{2}} - F_{k+\frac{1}{2}}^{(z)} A_{k+\frac{1}{2}}, \quad (6.9)$$

where  $F_{i+\frac{1}{2}}^{(x)}$ ,  $F_{i-\frac{1}{2}}^{(x)}$ ,  $F_{j+\frac{1}{2}}^{(y)}$ ,  $F_{j-\frac{1}{2}}^{(y)}$ ,  $F_{k+\frac{1}{2}}^{(z)}$ ,  $F_{k-\frac{1}{2}}^{(z)}$  are the numerical fluxes at the cell boundaries, and  $A_{i+\frac{1}{2}} = A_{i-\frac{1}{2}} = \Delta y \Delta z$ ,  $A_{j+\frac{1}{2}} = A_{j-\frac{1}{2}} = \Delta z \Delta x$ ,  $A_{k+\frac{1}{2}} = A_{k-\frac{1}{2}} = \Delta x \Delta y$  are the areas of the boundary faces. Assuming  $u > 0$ ,  $v > 0$ ,  $w > 0$  and applying a first order upwind scheme for the numerical fluxes gives

$$\Delta x \Delta y \Delta z \frac{\rho^{n+1} - \rho^n}{\Delta t} = u \rho_{i-1}^n \Delta y \Delta z + v \rho_{j-1}^n \Delta z \Delta x + w \rho_{k-1}^n \Delta x \Delta y - u \rho^n \Delta y \Delta z - v \rho^n \Delta z \Delta x - w \rho^n \Delta x \Delta y. \quad (6.10)$$

For  $\rho_{i-1}^n = \rho_{j-1}^n = \rho_{k-1}^n = 0$  the numerical massflow into the cell is zero at three cell boundaries, but mass flows out of the cell at the three other cell boundaries. In order to guarantee that the density

$$\rho^{n+1} = \rho^n - \Delta t \rho^n [u/\Delta x + v/\Delta y + w/\Delta z] \quad (6.11)$$

at time  $t_{n+1} = t_n + \Delta t$  is positive, for any choice of  $u$ ,  $v$  and  $w$  the timestep has to fulfill the condition  $\Delta t < 1/(|u|/\Delta x + |v|/\Delta y + |w|/\Delta z)$ . Hence the sum of the directional Courant numbers  $C^{(x)} = |u| \Delta t / \Delta x$ ,  $C^{(y)} = |v| \Delta t / \Delta y$ ,  $C^{(z)} = |w| \Delta t / \Delta z$  has to be smaller than one. If the velocity vector is co-linear with the cell diagonal vector, all three directional Courant numbers have the same size  $C^{(x)} = C^{(y)} = C^{(z)}$  as the Courant number  $C = \|\mathbf{u}\| \Delta t / \Delta L$  built with the length of the diagonal  $\Delta L = \sqrt{\Delta x^2 + \Delta y^2 + \Delta z^2}$ . The time step restriction for that case is

$$\Delta t < \frac{1}{3} \Delta L / \|\mathbf{u}\|, \quad (6.12)$$

or in other words, the Courant number has to fulfill  $C < 1/3$ . This condition in combination with a safety factor for non-orthogonality is used by the Euler equation solver on grids with hexahedral cells, e.g. on the cylindrical domain of the reciprocating compressor. Numerical tests show that the von Neumann stability criterion requires a similar time step restriction, see e.g. Toro [81].

## 6.6 Numerical Boundary Conditions for Valves

For the numerical boundary conditions of valves the flows of mass, momentum and energy crossing the boundary are needed. According to Equation (3.37) the flow of mass  $|\dot{m}_2|$  is known depending on  $\rho_1, u_1, p_1, p_2$  shown in Figure 3.1. The flow of momentum and energy have to be determined. The method to determine these numerical boundary conditions are presented for the suction valve and the discharge valve.

### 6.6.1 Suction Valve

It is possible to use the Godunov scheme based on the Rankine-Hugoniot conditions to determine force and enthalpy flow. Figure 6.5 shows the characteristics occurring at the interface of a boundary cell on the computation domain (point 2) and a fictive ghost cell (point 1). In order to avoid confusion, it has to be mentioned, that the velocity  $u_2$  is related to the computation domain and is not identical with the velocity in the nozzle from Equation (3.36). Since the boundary condition is applied at  $x = 0$ , the nozzle of the valve can be thought to be represented by the variables  $\rho_1^*, u_1^*, p_1^*$  shown in Figure 6.5.

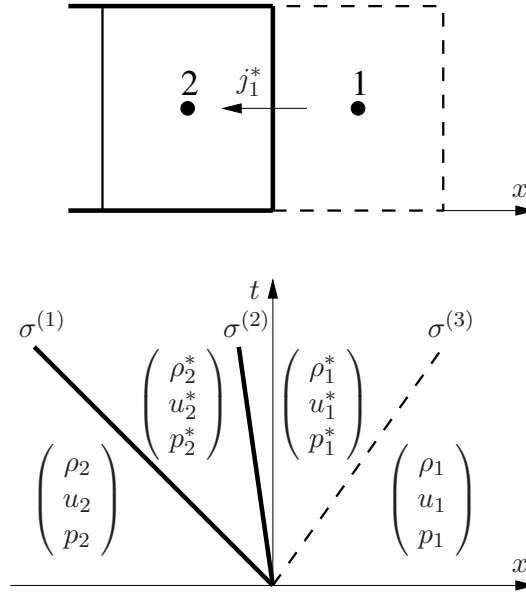


Figure 6.5: Cell and characteristics at suction valve boundaries

Assuming isentropic flow from point 1 to the intermediate state  $1^*$ , using Equation (3.18) gives  $\rho_1^* = \rho_1 (p_1^*/p_1)^{1/\gamma}$ . Inserting the relations for the contact discontinuity  $u_1^* = u_2^*$ ,  $p_1^* = p_2^*$  from Equation (3.30) in the shock condition from Equation (3.33) gives  $u_2^* = u_2 - c_2 (p_2^*/p_2 - 1) / \sqrt{\frac{\gamma}{2}(\gamma - 1) + \frac{\gamma}{2}(\gamma + 1) p_2^*/p_2}$ . With the mass flux  $j_1^* = -|\dot{m}_2|/A_2$  computed from the given mass flow  $|\dot{m}_2|$  in Equation (3.37), an

implicit equation for  $p_1^*$

$$j_1^* = \rho_1^* u_1^* = \rho_1 \left( \frac{p_1^*}{p_1} \right)^{1/\gamma} \left[ u_2 - c_2 \frac{p_1^*/p_2 - 1}{\sqrt{\frac{\gamma}{2}(\gamma - 1) + \frac{\gamma}{2}(\gamma + 1)p_1^*/p_2}} \right] \quad (6.13)$$

is obtained. Using the Mach number  $Ma_2 = u_2/c_2$ , this can be written as a nonlinear function for the unknown pressure ratio  $p_1^*/p_2$

$$f \left( \frac{p_1^*}{p_2} \right) = \left[ Ma_2 - \frac{j_1^*}{\rho_1 c_2} \left( \frac{p_1}{p_2} \right)^{1/\gamma} \left( \frac{p_1^*}{p_2} \right)^{-1/\gamma} \right] \sqrt{\frac{\gamma}{2}(\gamma - 1) + \frac{\gamma}{2}(\gamma + 1) \frac{p_1^*}{p_2}} - \frac{p_1^*}{p_2} + 1 = 0 \quad (6.14)$$

that has to be solved numerically. A good initial value for an iterative procedure is found making a Taylor series expansion for  $p_1^*/p_2 \approx 1$

$$\frac{p_1^*}{p_2} = 1 - \frac{\gamma(\tilde{j} - Ma_2)}{1 - (3 - \gamma)\tilde{j}/4 - (\gamma + 1)Ma_2/4} + \dots, \quad (6.15)$$

where  $\tilde{j} = (p_1/p_2)^{1/\gamma} j_1^*/(\rho_1 c_2)$  is a dimensionless mass flux, usually smaller than zero for the suction valve. With  $\tilde{p} = p_1^*/p_2$  an iterative routine to find  $\tilde{p}^*$  that fulfills  $f(\tilde{p}^*) = 0$  is the pseudo-code

$$\begin{aligned} \tilde{p}_1 &= \tilde{p}_0 \\ \tilde{p}_2 &= \tilde{p}_1 + \Delta\tilde{p}_0 \\ \text{while } (|f(\tilde{p}_2)| \leq \varepsilon) \{ \\ &\quad \tilde{p}^* = \tilde{p}_1 - f(\tilde{p}_1) \frac{\tilde{p}_2 - \tilde{p}_1}{f(\tilde{p}_2) - f(\tilde{p}_1)} \\ &\quad \tilde{p}_1 = \tilde{p}_2 \\ &\quad \tilde{p}_2 = \tilde{p}_1 + (\tilde{p}^* - \tilde{p}_1) \kappa \\ &\quad \} \end{aligned} \quad (6.16)$$

where  $\tilde{p}_0$  is the initial value taken from Equation (6.15),  $\Delta\tilde{p}_0$  is a small initial step size,  $\varepsilon$  is the accepted error and  $0 < \kappa \leq 1$  is the under-relaxation factor close to one for a Newton-Raphson solver. Hence, the numerical boundary condition applied to each cell of a suction valve boundary uses the following flow of mass, momentum and total enthalpy

$$\dot{m}^{(b)} = j_1^* A_2, \quad (6.17)$$

$$F^{(b)} = (j_1^{*2}/\rho_1^* + p_1^*) A_2, \quad (6.18)$$

$$\dot{H}_t^{(b)} = \left( \frac{\gamma}{\gamma - 1} \frac{p_1^*}{\rho_1^*} + \frac{1}{2} \frac{j_1^{*2}}{\rho_1^{*2}} \right) j_1^* A_2. \quad (6.19)$$

## 6.6.2 Discharge Valve

The Godunov scheme is also applied to discharge valve boundaries, in order to determine the numerical boundary conditions force and enthalpy flow. Figure 6.6 shows

the characteristics occurring at the interface of a boundary cell on the computation domain (point 1) with given data  $\rho_1, u_1, p_1$ , and a fictive ghost cell (point 2).

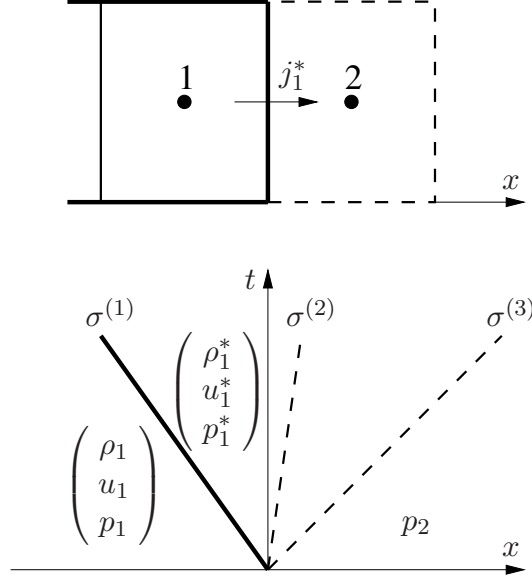


Figure 6.6: Cell and characteristics at discharge valve boundary

Two characteristics with speeds  $\sigma^{(2)}$  and  $\sigma^{(3)}$  leave the computation domain, while a single characteristic assumed as discontinuity propagates into the domain with speed  $\sigma^{(1)}$ . The intermediate variables  $\rho_1^*, u_1^*, p_1^*$  should occur in such a way, that the mass flux  $j_1^* = \rho_1^* u_1^*$  at the cell boundary during the time step becomes identical with  $|\dot{m}_2|/A_2$  obtained from the mass flow in Equation (3.37)

$$j_1^* = \rho_1 c_1 \frac{\phi_2}{A_2} \left( \frac{p_2}{p_1} \right)^{1/\gamma} \sqrt{Ma_1^2 + \frac{2}{\gamma-1} \left[ 1 - \left( \frac{p_2}{p_1} \right)^{1-1/\gamma} \right]}, \quad (6.20)$$

where  $c_1 = \sqrt{\gamma p_1/\rho_1}$  is the sound speed and  $Ma_1 = u_1/c_1$  is the Mach number in point 1. Using  $u_1^* = j_1^*/\rho_1^*$  the system of Rankine-Hugoniot conditions from Equations (3.27), (3.28), (3.29) to determine the unknowns  $\sigma^{(1)}, \rho_1^*, p_1^*$  reads

$$j_1^* - \rho_1 u_1 = \sigma^{(1)} (\rho_1^* - \rho_1), \quad (6.21)$$

$$\frac{j_1^{*2}}{\rho_1^*} - \rho_1 u_1^2 + p_1^* - p_1 = \sigma^{(1)} (j_1^* - \rho_1 u_1), \quad (6.22)$$

$$\frac{1}{2} \left( \frac{j_1^{*3}}{\rho_1^{*2}} - \rho_1 u_1^3 \right) + \frac{\gamma}{\gamma-1} \left( \frac{j_1^* p_1^*}{\rho_1^*} - u_1 p_1 \right) = \sigma^{(1)} \left[ \frac{1}{2} \left( \frac{j_1^{*2}}{\rho_1^*} - \rho_1 u_1^2 \right) + \frac{p_1^* - p_1}{\gamma-1} \right]. \quad (6.23)$$

The solution  $\sigma^{(1)} = u_1, \rho_1^* = \rho_1, p_1^* = p_1$  has to be excluded, because it describes the contact discontinuity denoted with  $\sigma^{(2)}$  in Figure 6.6. With the dimensionless quantities  $\tilde{\mu} = j_1^*/(\rho_1 c_1)$  and  $\tilde{\delta} = \frac{1}{2}[(\gamma+1) Ma_1 - (\gamma-1) \tilde{\mu}]$  the non-trivial solutions

for the propper characteristic

$$\sigma^{(1)} = u_1 + \left[ \frac{2}{3} \sqrt{3 + \tilde{\delta}^2} \cos \left( \frac{1}{3} \arccos \left( \frac{27 \tilde{\mu} - 9 \tilde{\delta} - 2 \tilde{\delta}^3}{2 (3 + \tilde{\delta}^2)^{3/2}} \right) - \frac{2 \pi k}{3} \right) - \frac{\tilde{\delta}}{3} \right] c_1, \quad (6.24)$$

$$\rho_1^* = \rho_1 + (j_1^* - \rho_1 u_1) / \sigma^{(1)}, \quad (6.25)$$

$$p_1^* = p_1 + \rho_1 (j_1^* - \rho_1 u_1) (\sigma^{(1)} - u_1)^2 / (j_1^* - \rho_1 u_1 + \rho_1 \sigma^{(1)}), \quad (6.26)$$

are the result of a cubic equation, where  $k = 0, 1, 2$  offers three possibilities. Depending on  $Ma_1$  and  $\tilde{\mu}$  the correct subsonic solution with  $\sigma^{(1)} \leq 0$  is extracted. The numerical boundary conditions for mass flow, force and total enthalpy flow applied to every discharge valve boundary are

$$\dot{m}^{(b)} = j_1^* A_2, \quad (6.27)$$

$$F^{(b)} = (j_1^{*2} / \rho_1^* + p_1^*) A_2, \quad (6.28)$$

$$\dot{H}_t^{(b)} = \left( \frac{\gamma}{\gamma - 1} \frac{p_1^*}{\rho_1^*} + \frac{1}{2} \frac{j_1^{*2}}{\rho_1^{*2}} \right) j_1^* A_2. \quad (6.29)$$

# Chapter 7

## Results

### 7.1 Results Overview

In this section, the results obtained with the flow solver are presented for reciprocating compressors with different size and different number of suction and discharge valves located at the cylinder circumferential surface in rather symmetrical arrangement. The influence of the valves mass-spring setting on the valve plate closing velocities is briefly discussed by varying the spring-stiffness. For the compressor with the largest piston diameter, the flow inside the working chamber is forced into the supersonic regime by applying a higher, but not unrealistic, rotational crank speed. In general, the results may be splitted in global flow properties, e.g. the time-dependend massflows entering or leaving the computation domain, and local flow properties like the pressure or the velocity field acting on the piston. The following quantities relevant for a reciprocating compressor are discussed:

- **MASS and MASSFLOWS:** In order to demonstrate the conservation ability of the finite volume method the working chamber mass is shown to be really a constant while the valves are closed during gas expansion and gas compression. The pulsative character of the massflows through suction valves and discharge valves is highlighted, especially for valves with non-optimal valve-spring-layout.
- **VALVE PLATE LIFTS:** The valve plate lifts of suction and discharge valves and the plate velocities are presented for different valve springs and maximal valve plate lifts.
- **PRESSURE:** The area-averaged pressure on the piston and on the valves is plotted over crank-angle and working chamber volume for comparison with the idealized process. In order to show the wave effects, the pressure distribution on the piston is shown at many different crank angles.
- **FLOW VELOCITIES:** The velocity field near the piston is sketched out during gas expansion. Since there is no flow passing the valves during expansion, the velocity magnitude slowly vanishes with respect to time.
- **MACH-NUMBERS:** The maximal Mach numbers occuring within a compressor period inside the cylinder and the valve pockets of suction and discharge valves are plotted over crank-angle. This illustrates, that subsonic and supersonic flows can be computed pretty well.

## 7.2 Investigated Cases

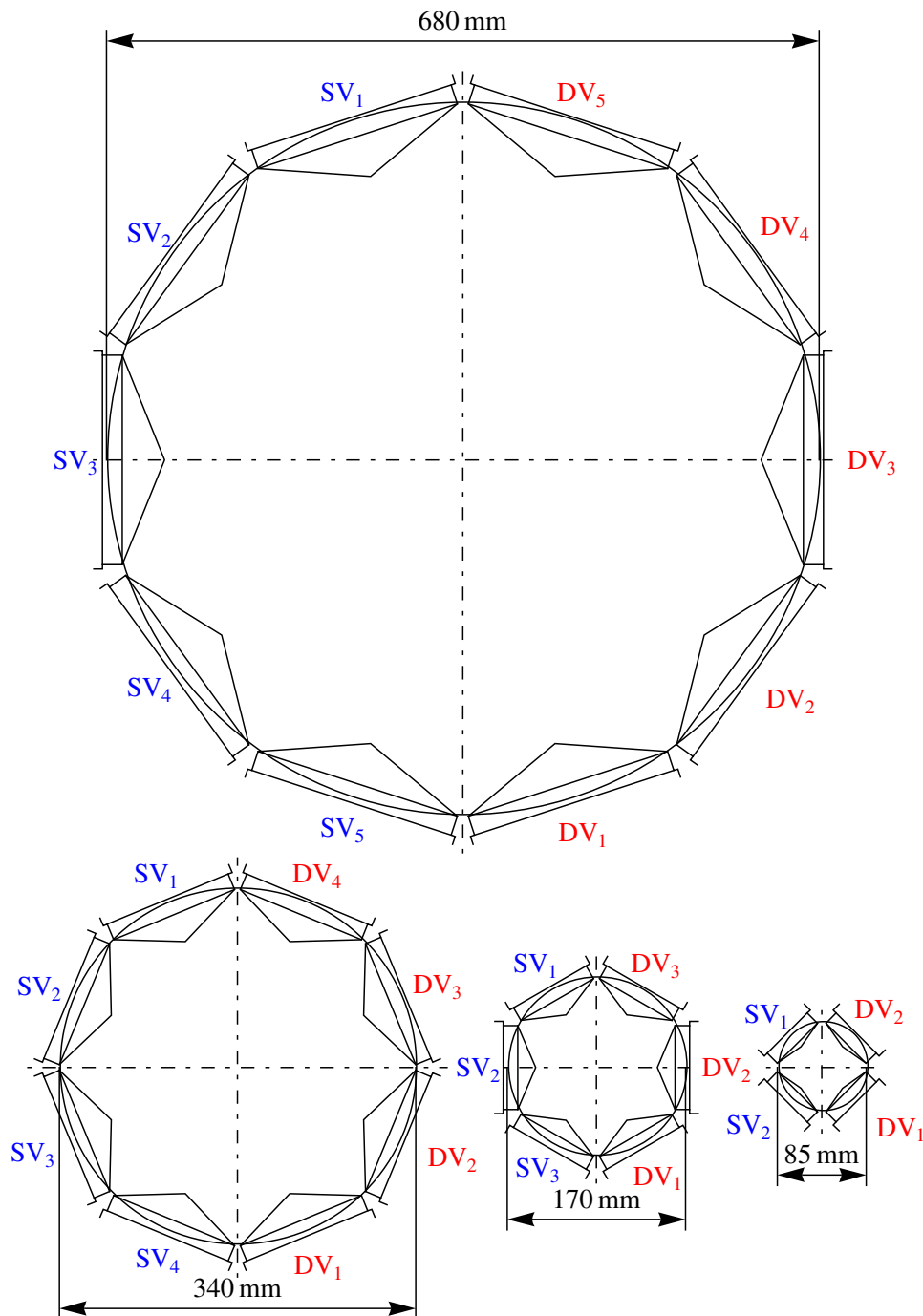


Figure 7.1: Top-view on four different reciprocating compressors with piston stroke  $2r = 150 \text{ mm}$  and different number of suction valves (SV) and discharge valves (DV): Large piston diameter  $d_P = 680 \text{ mm}$  with five suction and five discharge valves (top), mid-sized piston diameter  $d_P = 340 \text{ mm}$  with four suction and four discharge valves (bottom, left), small piston diameter  $d_P = 170 \text{ mm}$  with three suction and three discharge valves (bottom, middle), and very small piston diameter  $d_P = 85 \text{ mm}$  with two suction and two discharge valves (bottom, right)



In order to get an overview of the Euler-solver flexibility, four reciprocating compressors with totally different size, and number of suction and discharge valves are investigated. Figure 7.1 shows the top-view on the cylinder-head for a large, a mid-sized, a small and a very small cylinder diameter. As can be seen easily, the diameter is always half of the larger compressor. Therefore, the piston area of the compressor with the next smaller diameter is exactly a quarter of the previous one. Using the same crank-shaft with a crank radius  $r = 0.075\text{ m}$  for all four compressors will result in designs with the same piston stroke  $2r = 0.15\text{ m}$ . Hence, the volume inside the cylinder of the compressor with piston diameter  $d_P = 680\text{ mm}$  is four times the cylinder volume of the compressor with  $d_P = 340\text{ mm}$ .

In the shown cases in Figure 7.1 the valve pockets are designed according to the data given in Table 2.1. Based on this geometrical data, the sum volume of all valve pockets of each compressor is 12.6% of the swept plunger volume. If the shown compressors are operated with the data presented in Table 2.2, all four machines are comparable in terms of dimensionless quantities of Equation (3.39). Since according to Table 2.2, the suction density  $\rho_s$  of the next smaller compressor is four-times that of the larger one, it can be expected, that due to the decreased volume of the smaller compressor, the delivered mass per crank-rotation is nearly the same.

## 7.3 Global Flow Properties

### 7.3.1 Mass and Massflows

An important feature of the finite volume method, used herein for the numerical solution of the Euler-equations, is its conservation property. E.g. if the suction valves and the discharge valves of a reciprocating compressor are closed, no massflow can enter or leave the computation domain. Since all the other surfaces except the valve areas are walls, it is possible to check, that the mass inside the compressor remains constant during gas expansion and gas compression. In Figure 7.2 the mass and the boundary mass flow over the computation domain surface are plotted over crank-angle for four different compressors delivering the same mass per crank rotation.

Of course, the mass curve over crank angle slightly differs from the curve for the ideal process described in section 3.4. However, as a consequence of the used numerical method, the mass is really a constant for all four compressors, while the suction and discharge valves are closed.

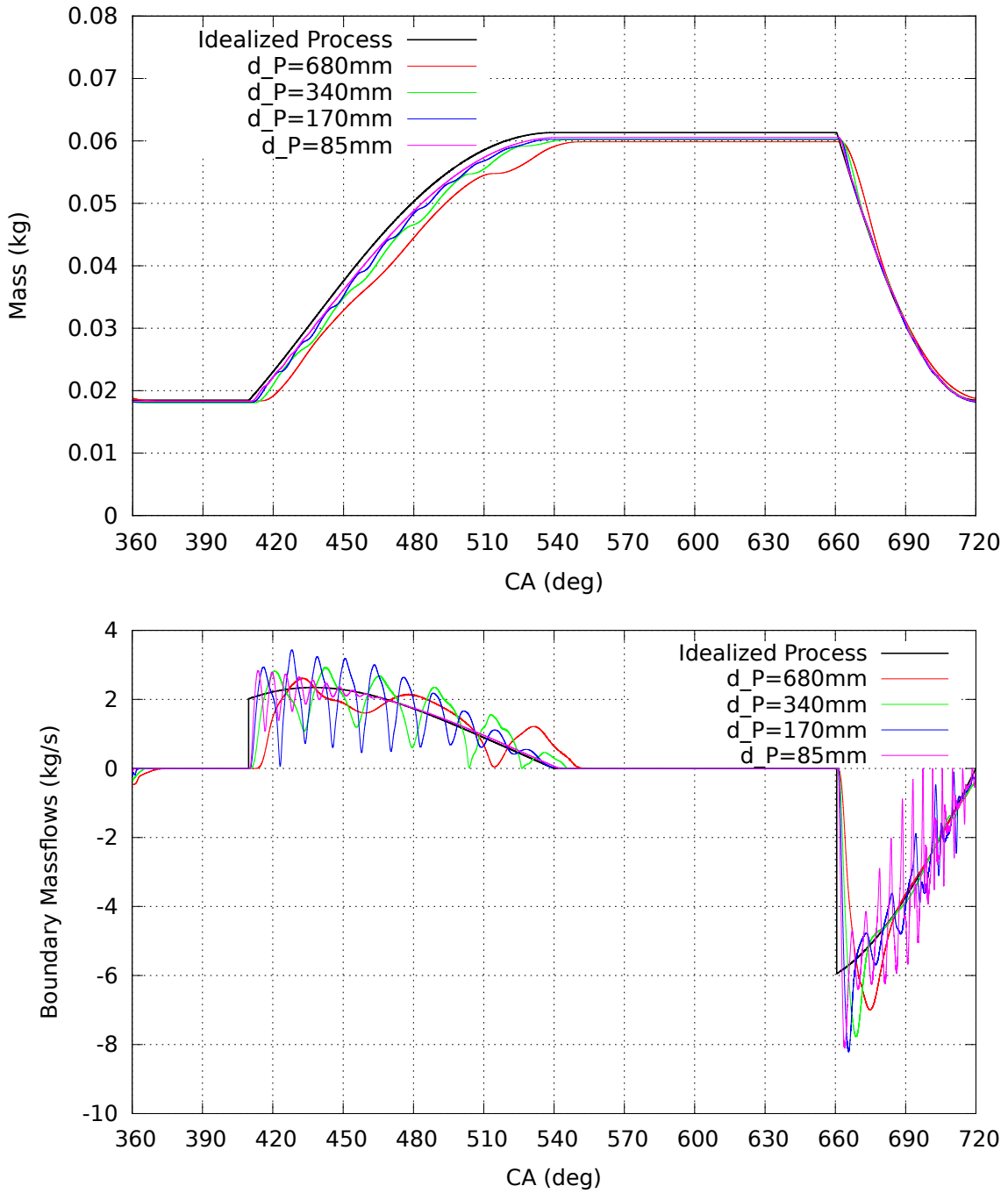


Figure 7.2: Includes gas mass (top) and mass flows at the boundaries (bottom) over crank angle, for the idealized cycle of a reciprocating compressor, and for four different compressors delivering almost the same mass per crank rotation.

## 7.3.2 Valve Plate Motion

### 7.3.2.1 Original Valve-Spring Data

Using the valve data given in Table 2.4 and Table 2.5, the valve plate lifts over crank-angle shown in Figure 7.3 are obtained for the compressors with piston diameters  $d_P = 680\text{ mm}$ ,  $d_P = 340\text{ mm}$ ,  $d_P = 170\text{ mm}$  and  $d_P = 85\text{ mm}$ .

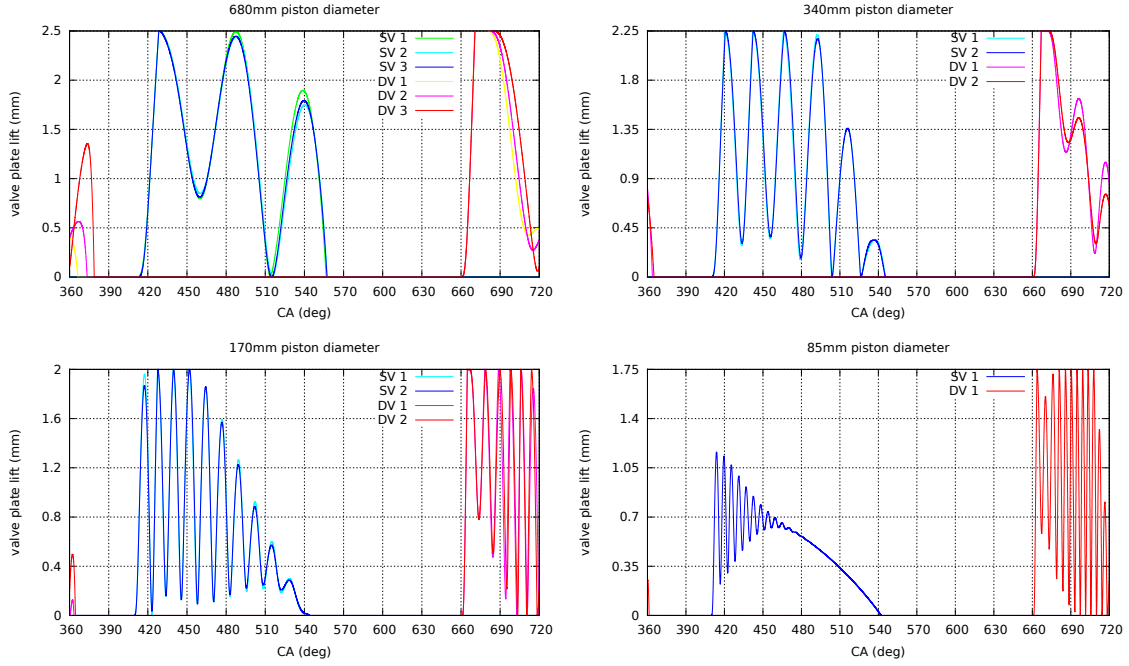


Figure 7.3: Valve plate motion over crank angle for four different compressor with piston diameters  $d_P = 680\text{ mm}$ ,  $d_P = 340\text{ mm}$ ,  $d_P = 170\text{ mm}$ ,  $d_P = 85\text{ mm}$  running with averaged piston speed  $\bar{v}_P = 4\text{ m/s}$ . The valve data is based on Table 2.4 and Table 2.5.

It turns out, that the suction valve  $SV_1$  of the compressor with piston diameter  $d_P = 85\text{ mm}$  does not reach the maximal valve plate lift  $x_{V,max} = 1.75\text{ mm}$ , and closes near the pistons bottom dead center at  $CA = 540^\circ$ . The same is true for the similar moving suction valve  $SV_2$ , not plotted in Figure 7.3. For the compressors with diameters  $d_P = 170\text{ mm}$  and  $d_P = 340\text{ mm}$ , it seems to be difficult for the suction valves  $SV_1$  and  $SV_2$  to stay open at  $x_{V,max} = 2.0\text{ mm}$  and  $x_{V,max} = 2.25\text{ mm}$ , respectively. This can also be observed for the discharge valves  $DV_1$  and  $DV_2$  of the compressor with piston diameter  $d_P = 170\text{ mm}$ .

In the original valve data given in Table 2.4, the maximal valve plate lift  $x_{V,max}$  was chosen in such a way, that for a maximal open valve, the geometric cross section of the valve plate seat passage  $f_e(x_{V,max})$  equals that of the valve ports  $f_{ports}$ , see for instance Equation (2.3). However, the question arises, if that large maximal valve plate lift is necessary for all compressors shown in Figure 7.1. Therefore, a

smaller maximal valve plate lift is considered for all cases 1, 2, 3 and 4.

Furthermore, for the compressors with smaller piston diameter, a high-frequency oscillation of the valve plate lifts can be observed after leaving the valve guards. The reason for that phenomenon might be a high valve spring force, trying to close the valve rapidly. If, as a first guess, the fluid force acting on the valve plate is assumed to be only a disturbance, the valve plate approximately oscillates with the eigenfrequency of the mass-spring-system. Since the maximal valve plate lift and the valve-plate motion-frequencies of the compressor with the diameter  $d_P = 680 \text{ mm}$  are not too bad, the value for  $x_{V,max}$  as well as the eigenfrequencies of the compressors with diameters  $d_P = 340 \text{ mm}$ ,  $d_P = 170 \text{ mm}$ ,  $d_P = 85 \text{ mm}$  are adapted according the data of case 1.

### 7.3.2.2 Smaller Valve-Spring Stiffness and Maximal Plate Lift

Since the original valve spring data presented in Table 2.5 results in high-frequently oscillating valve-plate lifts for the smaller piston diameter compressors, the eigenfrequency of the mass-spring-system

$$f_{MSS} = \frac{1}{2\pi} \sqrt{\frac{k_V}{m_V}} \quad (7.1)$$

from the compressor with piston diameter  $d_P = 680 \text{ mm}$  (case 1), is also used in the cases with piston diameters  $d_P = 340 \text{ mm}$  (case 2),  $d_P = 170 \text{ mm}$  (case 3), and  $d_P = 85 \text{ mm}$  (case 4). If the valve plate mass  $m_V$  is kept unchanged for all cases, the valve spring constants  $k_V = (2\pi f_{MSS})^2 m_V$  for the cases 2, 3 and 4 have to be adapted to obtain the eigenfrequency of case 1, namely  $53.52 \text{ Hz}$ . For comparison, the frequency of a compressor rotation with  $800 \text{ rpm}$  is  $13.33 \text{ Hz}$ . The force area  $A_f$  of the valve plates is also kept unchanged. Hence, in order to keep the pressure difference of the closed valved  $\Delta p_{closed} = k_V L_V / A_f$  on the same level, it is necessary to also adapt the length parameter  $L_V$ , representing the spring force of a closed valve. In Table 7.1 the modified mechanical valve parameters are listed.

Case	1	2	3	4
$A_f \text{ (m}^2\text{)}$	$1.781 \cdot 10^{-2}$	$6.769 \cdot 10^{-3}$	$2.654 \cdot 10^{-3}$	$1.168 \cdot 10^{-3}$
$m_V \text{ (kg)}$	$210 \cdot 10^{-3}$	$79.7 \cdot 10^{-3}$	$31.3 \cdot 10^{-3}$	$13.8 \cdot 10^{-3}$
$k_V \text{ (N m}^{-1}\text{)}$	23750	9014	3540	1516
$L_V \text{ (m)}$	$0.75 \cdot 10^{-3}$	$3.0 \cdot 10^{-3}$	$12.0 \cdot 10^{-3}$	$47.9 \cdot 10^{-3}$

Table 7.1: Modified mechanical valve parameters used for the simulations.

The maximal valve plate lift  $x_{V,max}$  may be chosen as a fraction of the valve diameter  $d_V$ . In order to test the influence of reducing the maximal valve plate lift, the values  $x_{V,max} = 0.0100 d_V$ ,  $x_{V,max} = 0.0125 d_V$  and  $x_{V,max} = 0.0150 d_V$  are considered. Table 7.2 lists the numerical values for  $x_{V,max}$ .

Case	1	2	3	4
$d_V (m)$	0.200	0.125	0.080	0.054
$0.0100 d_V (m)$	$2.0 \cdot 10^{-3}$	$1.25 \cdot 10^{-3}$	$0.8 \cdot 10^{-3}$	$0.54 \cdot 10^{-3}$
$0.0125 d_V (m)$	$2.5 \cdot 10^{-3}$	$1.5625 \cdot 10^{-3}$	$1.0 \cdot 10^{-3}$	$0.675 \cdot 10^{-3}$
$0.0150 d_V (m)$	$3.0 \cdot 10^{-3}$	$1.875 \cdot 10^{-3}$	$1.2 \cdot 10^{-3}$	$0.81 \cdot 10^{-3}$

Table 7.2: Smaller maximal valve plate lifts  $x_{V,max}$  depending on valve diameter  $d_V$ .

According to Equation (2.1), the maximal geometrical valve plate passage area is  $f_e(x_{V,max}) = f_{e1mm} x_{V,max}$ , where  $f_{e1mm}$  is defined in Equation (2.2). Given the maximal valve plate lifts  $x_{V,max}$  of Table 7.2, and the number of suction valves  $n_{SV}$  and discharge valves  $n_{DV}$  for the different cases 1, 2, 3 and 4, it may be interesting to know, how big the maximal valve plate geometrical passage area of all suction valves  $n_{SV} f_e(x_{SV,max})$  and all discharge valves  $n_{DV} f_e(x_{DV,max})$  is relative to the piston area  $A_P = \frac{\pi}{4} d_P^2$ . In the presented cases, the number of discharge valves equals the number of suction valves  $n_{DV} = n_{SV}$ , and the maximal valve plate lifts of suction valves and discharge valves are the same,  $x_{DV,max} = x_{SV,max}$ . Hence, the dimensionless quantities  $n_{SV} f_{e1mm} x_{SV,max} / (\frac{\pi}{4} d_P^2)$  and  $n_{DV} f_{e,1mm} x_{DV,max} / (\frac{\pi}{4} d_P^2)$  are identical as well. Therefore, in Table 7.3 only the area ratios of the suction valves are shown for  $x_{SV,max} = 0.0100 d_V$ ,  $x_{SV,max} = 0.0125 d_V$  and  $x_{SV,max} = 0.0150 d_V$ , respectively.

Case	1	2	3	4
$0.0100 n_{SV} f_{e,1mm} d_V / (\frac{\pi}{4} d_P^2)$	0.1635	0.1381	0.1169	0.1058
$0.0125 n_{SV} f_{e,1mm} d_V / (\frac{\pi}{4} d_P^2)$	0.2044	0.1726	0.1462	0.1323
$0.0150 n_{SV} f_{e,1mm} d_V / (\frac{\pi}{4} d_P^2)$	0.2453	0.2071	0.1754	0.1587

Table 7.3: Maximal geometrical valve plate passage area relative to the piston area for different maximal valve plate lifts:  $x_{V,max}/d_V = \{0.0100, 0.0125, 0.0150\}$ .

### 7.3.2.3 Valve Plate Lifts and Velocities

The valve plate lifts for suction valves  $x_{SV}$  and discharge valves  $x_{DV}$  are computed as function of the crank angle, for the cases 1, 2, 3 and 4. The maximal valve plate lifts  $x_{V,max}$  are taken according to Table 7.2. The suction valve plate velocities  $\dot{x}_{SV}$  and discharge valve plate velocities  $\dot{x}_{DV}$  are also presented. In Figure 7.4, Figure 7.5 and Figure 7.6, the valve plate lifts (left figure side) and the valve plate velocities (right figure side) are shown for all compressor cases and all suction and discharge valves, except the valves located symmetrically to that shown in the figures.

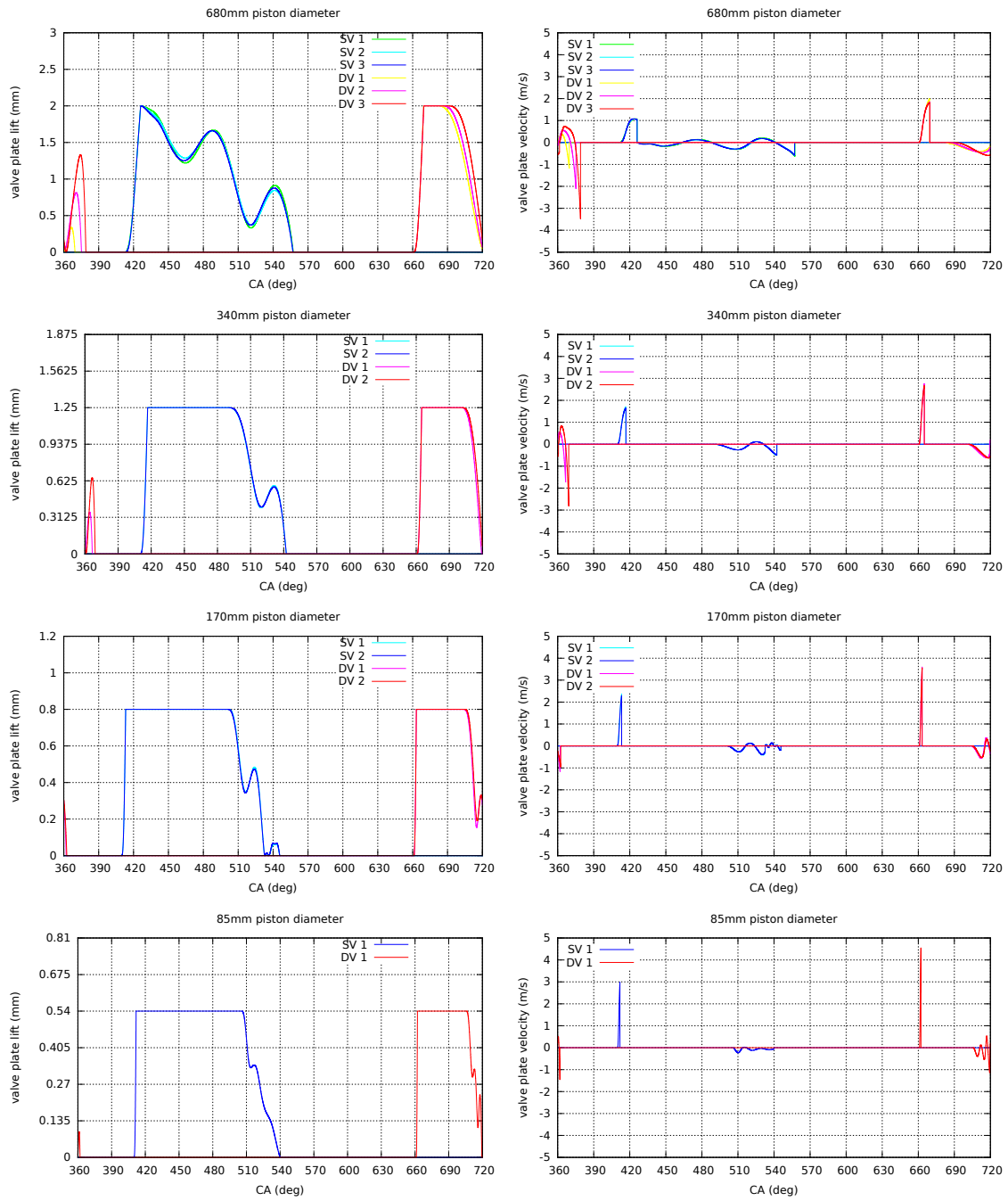


Figure 7.4: Valve plate lifts (left) and velocities (right) over crank angle for four compressor with piston diameters  $d_P = 680\text{ mm}$ ,  $d_P = 340\text{ mm}$ ,  $d_P = 170\text{ mm}$ ,  $d_P = 85\text{ mm}$  running with averaged piston speed  $\bar{v}_P = 4\text{ m/s}$ . The maximal valve plate lift is  $x_{V,max} = 0.01 d_V$ .

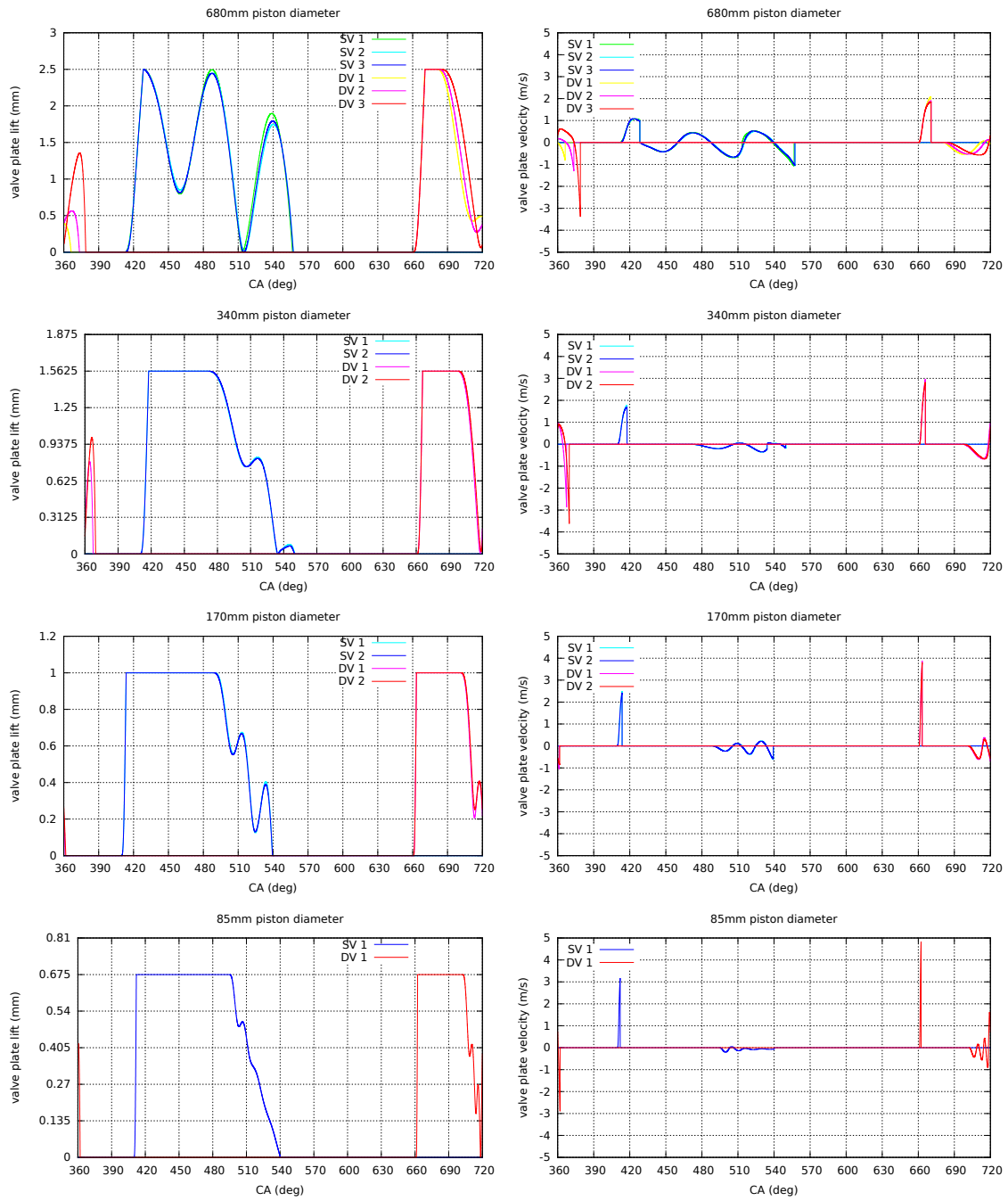


Figure 7.5: Valve plate lifts (left) and velocities (right) over crank angle for four compressor with piston diameters  $d_P = 680 \text{ mm}$ ,  $d_P = 340 \text{ mm}$ ,  $d_P = 170 \text{ mm}$ ,  $d_P = 85 \text{ mm}$  running with averaged piston speed  $\bar{v}_P = 4 \text{ m/s}$ . The maximal valve plate lift is  $x_{V,max} = 0.0125 d_V$ .

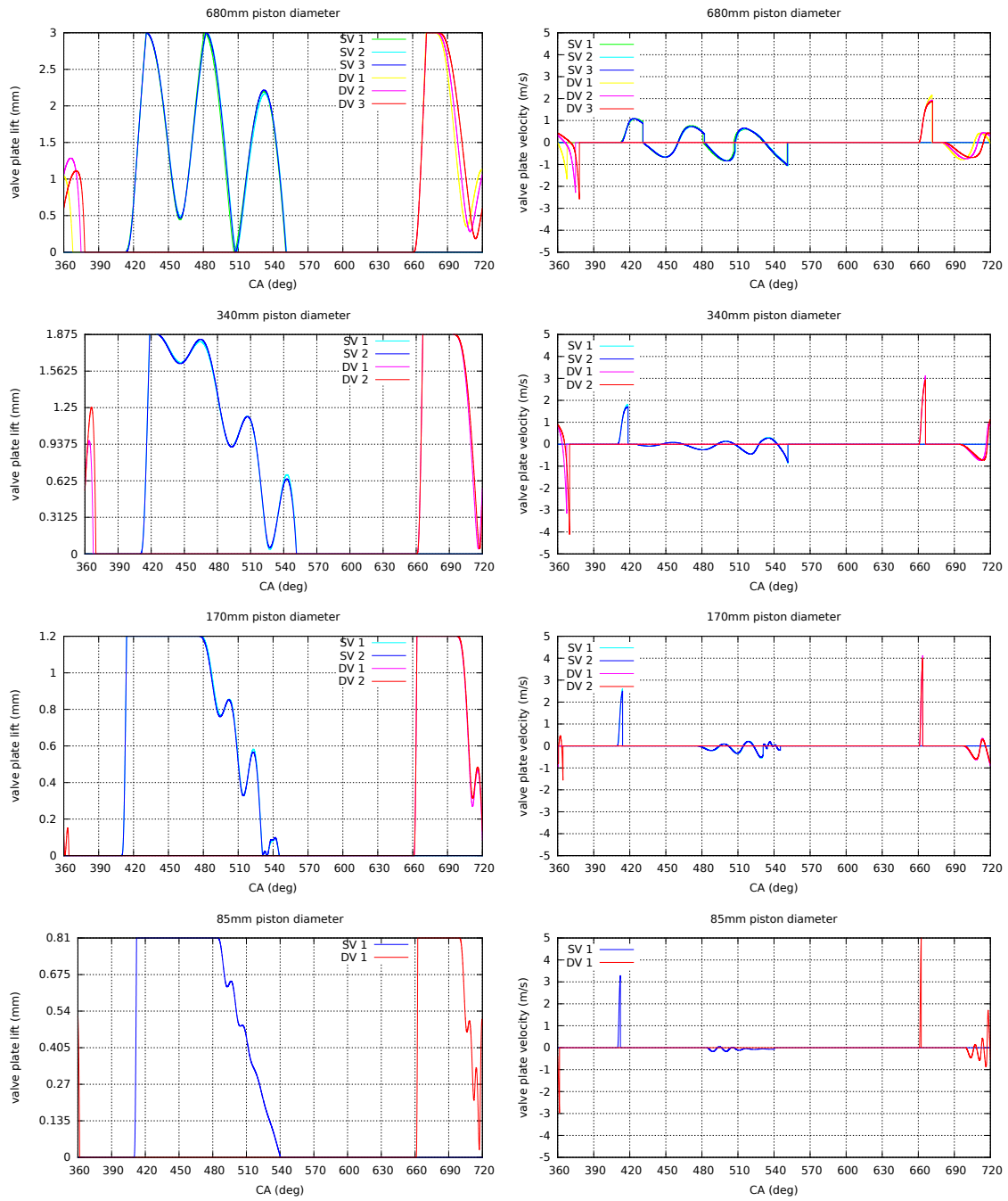


Figure 7.6: Valve plate lifts (left) and velocities (right) over crank angle for four compressor with piston diameters  $d_P = 680 \text{ mm}$ ,  $d_P = 340 \text{ mm}$ ,  $d_P = 170 \text{ mm}$ ,  $d_P = 85 \text{ mm}$  running with averaged piston speed  $\bar{v}_P = 4 \text{ m/s}$ . The maximal valve plate lift is  $x_{V,max} = 0.015 d_V$ .



For the valve life, the impact velocity of the valve plate on the valve guard and on the valve seat plays an important role. In the present valve model, the impact is modelled as completely inelastic. That means, that if the valve hits the guard at  $x_V = x_{V,max}$ , or comes back to the seat at  $x_V = 0$ , the valve plate velocity is set to zero, in both cases. Hence, it is implicitly assumed, that the kinetic energy of the valve plate motion is dissipated into heat, immediately. Four valve velocities can be evaluated:

- The valve plate impact velocity on the suction valve guard  $\dot{x}_{SV,guard}$ .
- The valve plate impact velocity on the suction valve seat  $\dot{x}_{SV,seat}$ .
- The valve plate impact velocity on the discharge valve guard  $\dot{x}_{DV,guard}$ .
- The valve plate impact velocity on the discharge valve seat  $\dot{x}_{DV,seat}$ .

Table 7.4 shows the valve plate impact velocities for all cases shown in Figure 7.4, Figure 7.5 and Figure 7.6. Only the valves with the largest velocity value are presented in the table.

	$\dot{x}_{SV,guard}$ (m/s)	$\dot{x}_{SV,seat}$ (m/s)	$\dot{x}_{DV,guard}$ (m/s)	$\dot{x}_{DV,seat}$ (m/s)
$\frac{x_{V,max}}{d_V} = 0.0100$	1.068 <sup>(1)</sup> (SV <sub>1</sub> )	-0.636 <sup>(1)</sup> (SV <sub>1</sub> )	1.995 <sup>(1)</sup> (DV <sub>1</sub> )	-3.487 <sup>(1)</sup> (DV <sub>3</sub> )
	1.706 <sup>(2)</sup> (SV <sub>1</sub> )	-0.513 <sup>(2)</sup> (SV <sub>1</sub> )	3.130 <sup>(2)</sup> (DV <sub>1</sub> )	-2.828 <sup>(2)</sup> (DV <sub>2</sub> )
	2.355 <sup>(3)</sup> (SV <sub>1</sub> )	-0.296 <sup>(3)</sup> (SV <sub>1</sub> )	3.608 <sup>(3)</sup> (DV <sub>1</sub> )	-1.173 <sup>(3)</sup> (DV <sub>1</sub> )
	2.991 <sup>(4)</sup> (SV <sub>1</sub> )	-0.004 <sup>(4)</sup> (SV <sub>1</sub> )	4.558 <sup>(4)</sup> (DV <sub>1</sub> )	-1.464 <sup>(4)</sup> (DV <sub>1</sub> )
$\frac{x_{V,max}}{d_V} = 0.0125$	1.020 <sup>(1)</sup> (SV <sub>1</sub> )	-1.070 <sup>(1)</sup> (SV <sub>1</sub> )	2.094 <sup>(1)</sup> (DV <sub>1</sub> )	-3.386 <sup>(1)</sup> (DV <sub>3</sub> )
	1.773 <sup>(2)</sup> (SV <sub>1</sub> )	-0.243 <sup>(2)</sup> (SV <sub>1</sub> )	2.968 <sup>(2)</sup> (DV <sub>1</sub> )	-3.624 <sup>(2)</sup> (DV <sub>2</sub> )
	2.504 <sup>(3)</sup> (SV <sub>1</sub> )	-0.615 <sup>(3)</sup> (SV <sub>1</sub> )	3.886 <sup>(3)</sup> (DV <sub>1</sub> )	-1.056 <sup>(3)</sup> (DV <sub>1</sub> )
	3.167 <sup>(4)</sup> (SV <sub>1</sub> )	-0.001 <sup>(4)</sup> (SV <sub>1</sub> )	4.839 <sup>(4)</sup> (DV <sub>1</sub> )	-2.897 <sup>(4)</sup> (DV <sub>1</sub> )
$\frac{x_{V,max}}{d_V} = 0.0150$	0.930 <sup>(1)</sup> (SV <sub>1</sub> )	-1.053 <sup>(1)</sup> (SV <sub>1</sub> )	2.158 <sup>(1)</sup> (DV <sub>1</sub> )	-2.591 <sup>(1)</sup> (DV <sub>3</sub> )
	1.811 <sup>(2)</sup> (SV <sub>1</sub> )	-0.883 <sup>(2)</sup> (SV <sub>1</sub> )	2.767 <sup>(2)</sup> (DV <sub>1</sub> )	-4.121 <sup>(2)</sup> (DV <sub>2</sub> )
	2.610 <sup>(3)</sup> (SV <sub>1</sub> )	-0.552 <sup>(3)</sup> (SV <sub>1</sub> )	4.130 <sup>(3)</sup> (DV <sub>1</sub> )	-1.568 <sup>(3)</sup> (DV <sub>2</sub> )
	3.298 <sup>(4)</sup> (SV <sub>1</sub> )	-0.001 <sup>(4)</sup> (SV <sub>1</sub> )	5.068 <sup>(4)</sup> (DV <sub>1</sub> )	-2.977 <sup>(4)</sup> (DV <sub>1</sub> )

Table 7.4: Valve plate impact velocities on the suction and discharge valve guards and seats for case 1:<sup>(1)</sup>, case 2:<sup>(2)</sup>, case3:<sup>(3)</sup>, and case 4:<sup>(4)</sup>.

It can be concluded, that a reduction of the maximal valve lift from  $x_{V,max} = 0.015 d_V$  to  $x_{V,max} = 0.01 d_V$  reduces the impact velocity on the valve guard from 3.298 m/s to 2.991 m/s for case 4, from 2.610 m/s to 2.355 m/s for case 3, and from 1.811 m/s to 1.706 m/s for case 2. Only for case 1, the impact velocity on the suction valve guard of suction valve 1 (SV<sub>1</sub>) is slightly increasing from 0.93 m/s to 1.068 m/s. However, impact velocities of about 1 m/s can be seen as relatively small anyway. In contrast, the data of the valve plate impact velocities on the valve seat of the suction valves is more scattered. The reason for that observation is, that the suction valve closing

motion is more sensitive than the motion of valve opening. The closing of the discharge valves also depends on the valve location. Especially for the compressor with piston diameter  $d_P = 680 \text{ mm}$  the discharge valve 3 ( $DV_3$ ) shows a much larger valve plate lift after the pistons top-dead-center (TDC), than it can be observed for the discharge valve 1 ( $DV_1$ ). For the compressor with piston diameter  $d_P = 340 \text{ mm}$  both plotted valves  $DV_1$ ,  $DV_2$  have somehow a re-opening after TDC. Hence, the impact velocities on the valve seats are very much different depending on the specific valve data and on the valve position. Regarding the impact velocities on the valve guards of the discharge valves, a maximal lift reduction from  $x_{V,max} = 0.015 d_V$  to  $x_{V,max} = 0.01 d_V$  decreases the maximal values from  $5.068 \text{ m/s}$  to  $4.558 \text{ m/s}$  for case 4, from  $4.130 \text{ m/s}$  to  $3.608 \text{ m/s}$  for case 3, and from  $2.158 \text{ m/s}$  to  $1.995 \text{ m/s}$  for case 1, while case 2 shows even growing velocities from  $2.767 \text{ m/s}$  to  $3.130 \text{ m/s}$ . Usually, a smaller maximal valve plate lift also reduces the time from the beginning of valve opening until the plate hits the guard. Since the pressure difference acting on the valve plate causes the body acceleration, a reduction of the opening time also hinders the plate to gain that much speed.

### 7.3.3 Valve Plate Forces and Piston Force

For an idealized compressor model, where the compressibility effects of the fluid during suction and discharge are neglected, the pressure inside the working chamber only depends on the crank-angle  $\varphi$ , see e.g. section 3.4. Such a thermodynamic model is also said to be zero-dimensional in space, because there is no space dependency of the quantities at all. However, in a three-dimensional CFD-model, where the wave dynamic due to compressibility is included, the pressure can be expected to be a function of space as well. In order to get an impression of the different results compared to the simple thermodynamic model plotted in Figure 3.3 and Figure 3.2, the area-averaged pressure on the piston and on the valves is plotted in Figure 7.7 over the crank-angle, and over the volume of the working chamber for the compressor with a piston diameter  $d_P = 680 \text{ mm}$ , having 5 suction valves and 5 discharge valves allowing a maximal valve plate lift of  $x_{V,max} = 2.5 \text{ mm}$ . Because the geometrical configuration of the valve pockets  $SV_5$  and  $SV_4$  is symmetrically to the pockets  $SV_1$  and  $SV_2$ , the average pressure curves over crank angle and volume are similar as well. The same is true for the symmetric location of the valve pockets  $DV_5$  and  $DV_4$  relative to the pockets  $DV_1$  and  $DV_2$ . Therefore, in Figure 3.3 and Figure 3.2. only the averaged pressure on the faces of the valve pockets  $SV_1$ ,  $SV_2$ ,  $SV_3$ ,  $DV_1$ ,  $DV_2$ ,  $DV_3$ , are shown.

Since the plotted pressure curves for the piston and the valves are derived from dividing the pressure force acting on the zone by the area of the zone, the time-oscillations of the pressure due to that filtering, are not that large as they are in a single point of the domain.

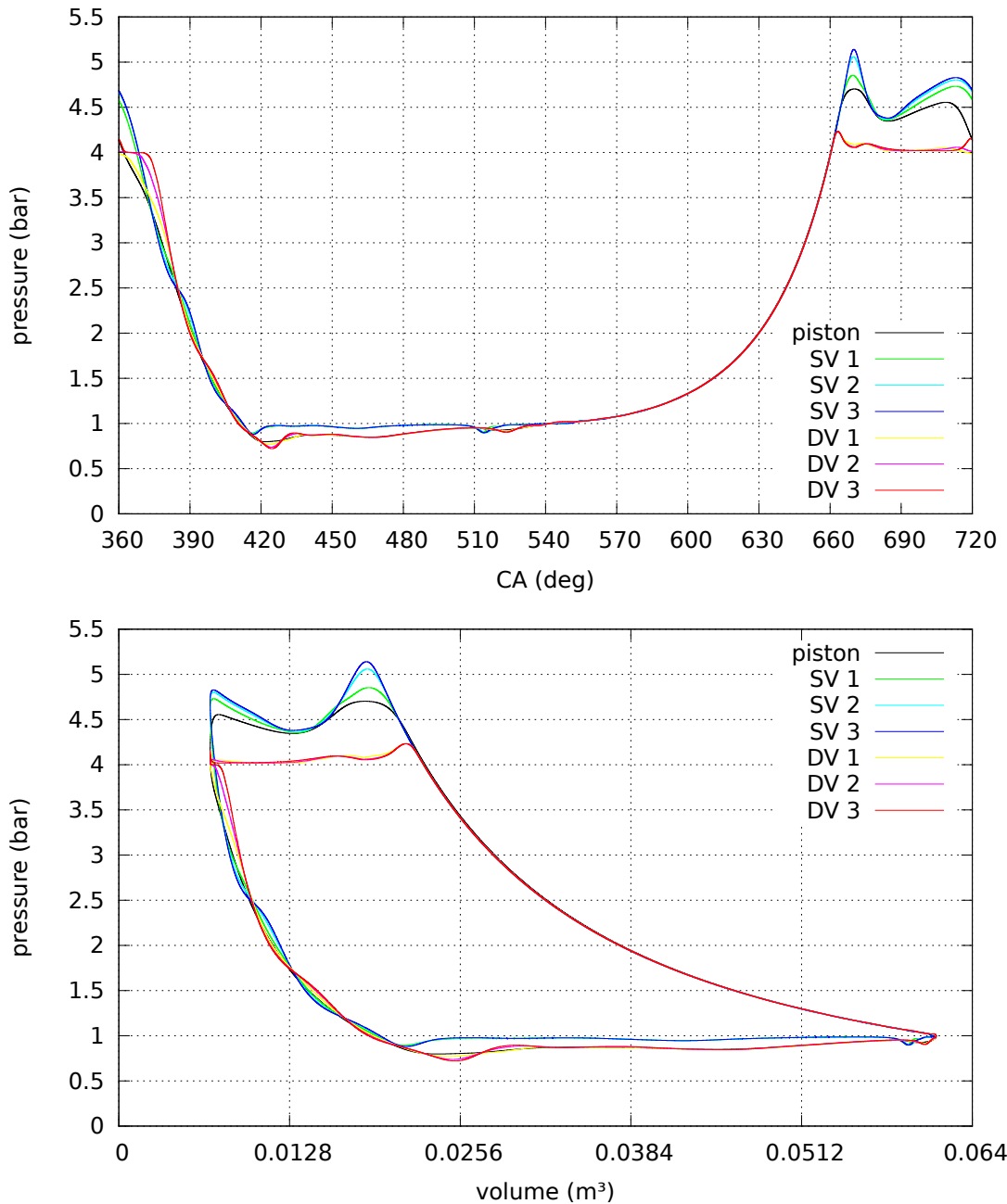


Figure 7.7: Area-averaged pressure on piston and valves over crank-angle (top) and volume (bottom) for a compressor with piston diameter  $d_P = 680 \text{ mm}$  running with averaged piston speed  $\bar{v}_P = 4 \text{ m/s}$ , having 5 suction valves and 5 discharge valves in symmetric configuration.

However, it can be observed, that during compression the average pressure acting on piston and valves pretty much follows the same curve, while during expansion especially the pressure at suction valve 3 ( $SV_3$ ) and the pressure at discharge valve 3 ( $DV_3$ ) are deviating from the pressure at the piston.

During suction and discharge the pressure curves differ even more from each other. In particular, the pressure acting on the suction valves during discharge is larger than that acting on the piston and on the discharge valves. Since the discharge valves open at the crank angle  $\varphi = 660.48^\circ$ , it seems that the compression still takes place near the suction valves, while near the discharge valves the compression has stopped due to the out-going discharge valve massflows. The only explanation for this phenomenon is, that near the suction valves the information of an open discharge valve has not arrived yet, due to the time it takes to transport the wave reflected on the open discharge valve with the speed of sound through the working chamber.

An estimate of the required time for a pressure wave to propagate through the working chamber with diameter  $d_P = 0.68\text{ m}$  gives  $t = 1.49 \cdot 10^{-3}\text{ s}$  based on the sound speed  $c = \sqrt{\gamma p/\rho} = 456\text{ m/s}$  derived from a pressure level of  $p = 4 \cdot 10^5\text{ Pa}$  and a density of approximately  $\rho = 2.692\text{ kg/m}^3$  at discharge for  $\gamma = 1.4$ . These values can simply be computed a priori based on the idealized pressure process described in section 3.4, without doing any CFD. Note, that with the CFD-results a sound speed of approximately  $c = 470 \pm 5\text{ m/s}$  can be found during discharge. Considering the rotational speed of the compressor  $\dot{\varphi} = \frac{\pi}{30}800\text{ rad/s}$ , the time-difference  $t = 1.49\text{ ms}$  can be transferred into a crank angle difference of  $\Delta\varphi = 7.16^\circ$ . In the CFD-results the wave propagation speed is maybe slightly faster, because the compression higher than discharge pressure also increases the sound speed. In Figure 7.7 it can be observed, that the peak averaged pressure  $\hat{p}_{DV_{1,2,3}} = 4.233 \cdot 10^5\text{ Pa}$  at the discharge valves  $DV_1$ ,  $DV_2$  and  $DV_3$  occurs at the crank angle  $\varphi_{DV_{1,2,3}} = 663.28^\circ$ , while the suction valves  $SV_1$ ,  $SV_2$  and  $SV_3$  have their peak averaged pressure values  $\hat{p}_{SV_1} = 4.854 \cdot 10^5\text{ Pa}$ ,  $\hat{p}_{SV_2} = 5.060 \cdot 10^5\text{ Pa}$  and  $\hat{p}_{SV_3} = 5.141 \cdot 10^5\text{ Pa}$  at the crank angle values  $\varphi_{SV_1} = 669.61^\circ$ ,  $\varphi_{SV_2} = 669.87^\circ$  and  $\varphi_{SV_3} = 670.04^\circ$ , respectively. The maximal pressure at the piston  $\hat{p}_P = 4.703 \cdot 10^5\text{ Pa}$  averaged over the piston area can be recognized at the crank angle  $\varphi_P = 670.33^\circ$ . Hence, there is really a crank angle delay of approximately  $\Delta\varphi \approx 7^\circ$  between the pressure peaks of the discharge valves and the suction valves.

In Figure 7.8 the averaged pressure acting on the piston and on the valves is shown for the compressors with piston diameters  $d_P = 340\text{ mm}$ ,  $d_P = 170\text{ mm}$  and  $d_P = 85\text{ mm}$ . It can be seen, that the pressure overshoots after discharge valve opening become smaller with decreasing piston diameters. The required time for waves to carry the information of an open discharge valve through the domain is directly proportional to the piston diameter, if the speed of sound is assumed to be the same. In case of a smaller distance between discharge valves and suction valves, the maximal compression pressure near the suction valves shown in Figure 7.8 can not reach such a high level as for the large diameter compressor shown in Figure 3.3 and Figure 3.2. As a consequence it can be concluded, that the additional piston driving power necessary to produce the pressure overshoots, is not purely caused by the losses of the flow through the discharge valves, but mainly comes from the dynamic effect of waves propagating through the fluid domain.

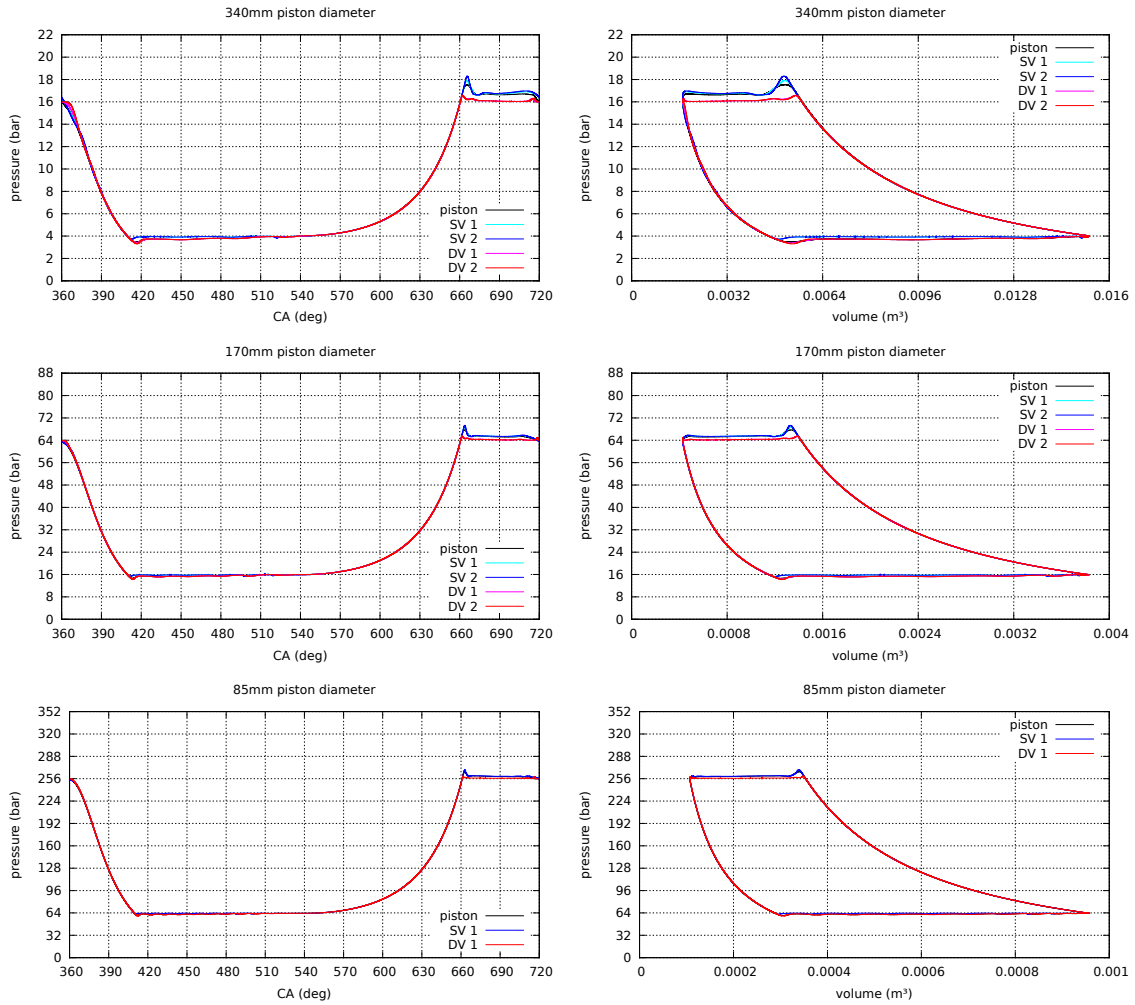


Figure 7.8: Area-averaged pressure on piston and valves over crank-angle (left) and volume (right) for compressors running with averaged piston speed  $\bar{v}_P = 4 \text{ m/s}$ . The piston diameters are  $d_P = 340 \text{ mm}$  (top),  $d_P = 170 \text{ mm}$  (middle) and  $d_P = 85 \text{ mm}$  (bottom).

## 7.4 Local Flow Properties

### 7.4.1 Pressure Distribution on the Piston

#### 7.4.1.1 After Discharge Valve Opening

The pressure wave traveling through the domain after the opening of the discharge valves at crank angle  $\varphi = 300.48^\circ$  (or  $\varphi = 660.48^\circ$  in the second period) is important for the maximal pressure reached near the suction valves, especially for compressors with larger piston diameters. Therefore, in Figure 7.9 the pressure distribution on the piston is illustrated for the compressor with piston diameter  $d_P = 680 \text{ mm}$  at six different crank angles after discharge valve opening.

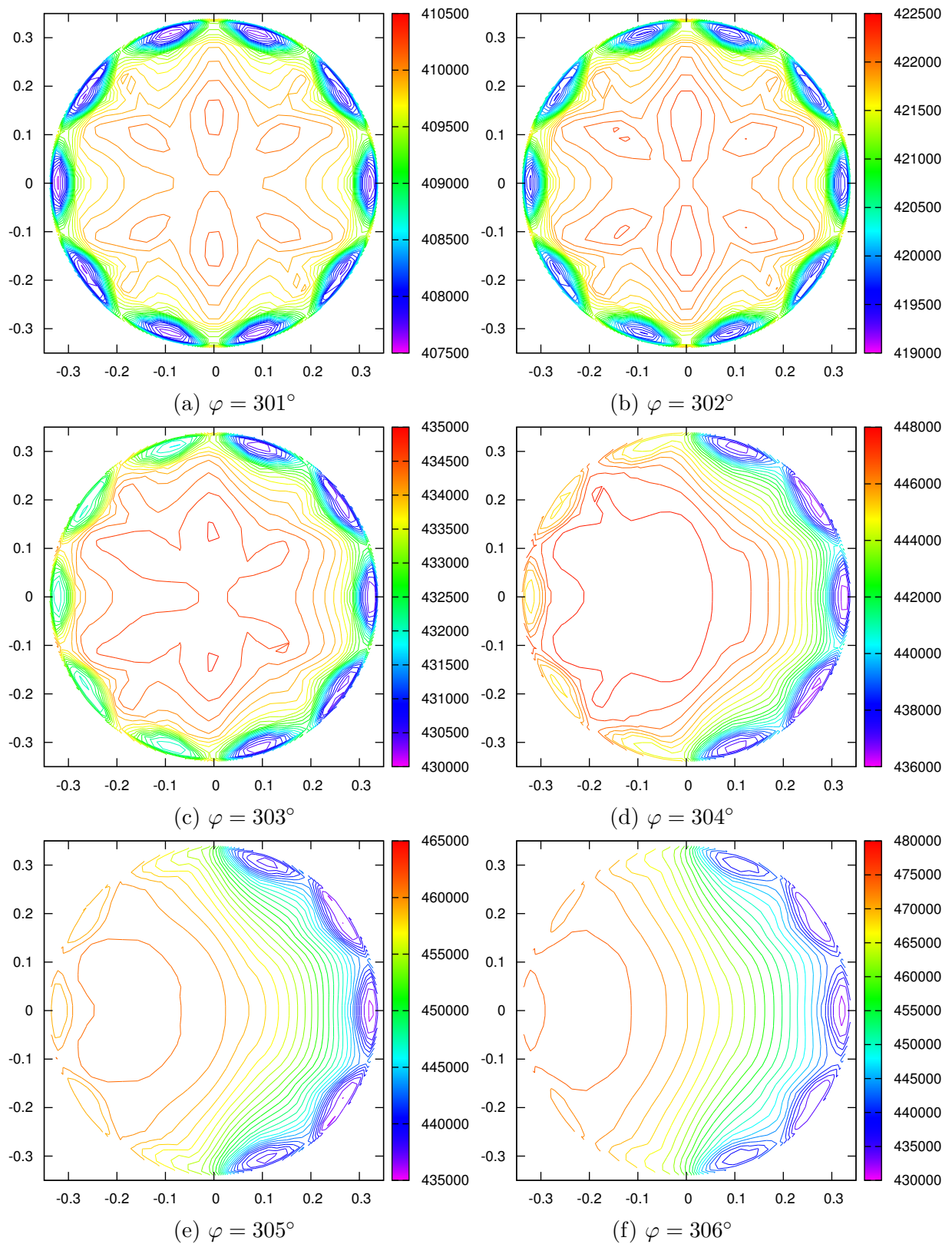


Figure 7.9: Pressure distribution on the piston at six different crank angles after opening of the discharge valves for a reciprocating compressor with piston diameter  $d_P = 680 \text{ mm}$  and with 10 valves.

Right after the discharge valve opening at crank angle  $\varphi = 301^\circ$ , Figure 7.9 (a) shows that the pressure acting on the piston is completely symmetrically. Hence, all the asymmetric flow patterns that occur during suction have disappeared at the end of compression. At crank angle  $\varphi = 303^\circ$  the pressure field becomes asymmetric. Near the connection to the suction valve pockets the piston pressure is increasing due to the ongoing gas compression, while at the connection to the discharge valve pockets the pressure on the piston increases only slightly. A large field with higher pressure on the piston forms on the left side of Figure 7.9 (d), while on the right side of the picture the pressure wave coming from the discharge valve pockets unite to a single wave front, that reaches the suction valve pockets  $SV_1$  and  $SV_5$  at crank angle  $\varphi = 305^\circ$ . At  $\varphi = 306^\circ$  the wave front in the middle of the compressor is almost planar. The discharge valve pockets  $DV_1$  and  $DV_2$  close to the suction valve pockets only cause a small deformation of the wave shape.

#### 7.4.1.2 At the Top-Dead-Center

In Figure 7.10 the pressure distribution on the piston is shown at the pistons top-dead-center, where the crank angle becomes  $\varphi = 360^\circ$ . At this position the distance between the piston and the cylinder head has its minimal value.

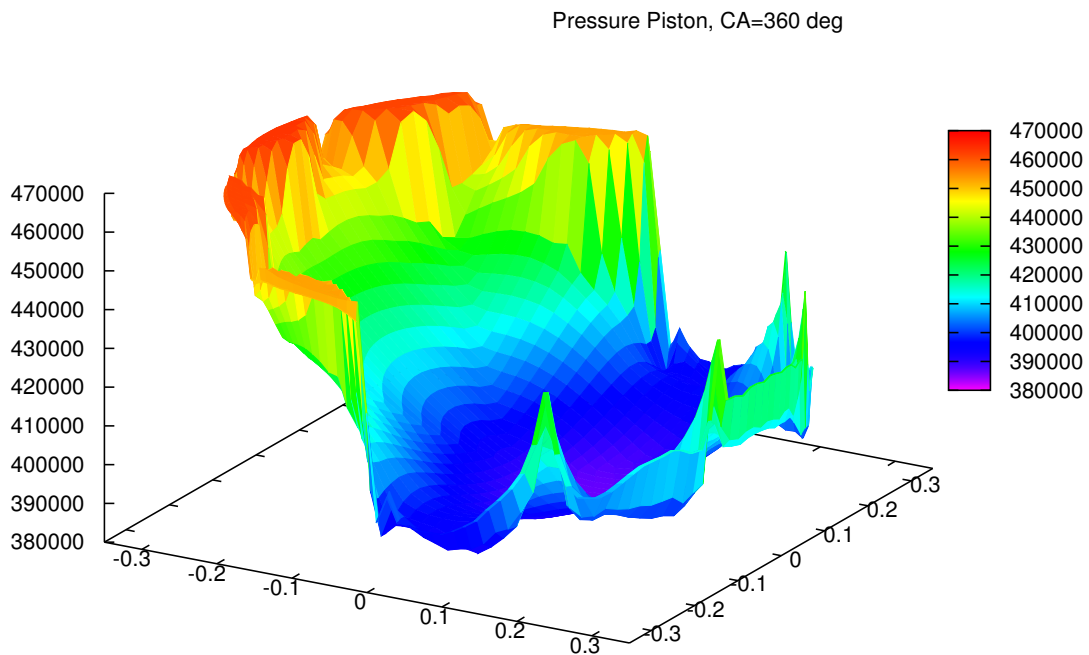


Figure 7.10: Pressure acting on the piston with diameter  $d_P = 680 \text{ mm}$  at  $\varphi = 360^\circ$ .

While the average pressure acting on the piston is larger than the discharge pressure  $p_d = 4 \cdot 10^5 Pa$ , the smallest value in the middle of the piston is below  $p_d$ . The largest value of the pressure on the piston occurs close to the mid suction valve pocket  $SV_3$ . The piston pressure dramatically drops between the position of the suction valve pocket  $SV_1$  and the discharge valve pocket  $DV_5$ , and between the pockets  $SV_5$  and  $DV_1$ . The effect of the 10 valve pockets on the piston pressure distribution can be clearly recognized in Figure 7.10. Between the discharge valve pockets the flow can not leave the cylinder domain, and the pressure increases due to the stagnation of the gas at the wall. These pressure peaks between the pockets demonstrate the functionality of the cylinder to valve pocket interface coupling method, described in section 6.4.3.

### 7.4.1.3 After the Top-Dead-Center

After the pistons top-dead-center TDC the cylinder volume starts to increase. However, as can be seen in Figure 7.5 for the compressor with  $d_P = 680 mm$  and  $x_{V,max} = 2.5 mm$ , the discharge valves are still open for a crank angle larger than  $\varphi = 360^\circ$ . The valve plate lifts after TDC seem to be very sensitive to the plate motion before TDC, and are also different for every discharge valve, depending on the location along the cylinder circumferential surface. Hence, the expansion of the gas does not happen uniformly.

In Figure 7.11 the pressure on the piston is shown for six different crank angles after the top-dead-center. The largest pressure on the piston always appears near the connection to the suction valve pockets, while in Figure 7.11 (a) the minimal pressure occurs close to the center. A local pressure maximum is present between the pockets of the discharge valves. As can be observed in Figure 7.11 (c), the region of minimal pressure separates into two zones, that are located closer to the cylinder walls, but still lie almost in the symmetry plane between suction and discharge valves. According to the coordinate system defined in Figure 2.2, this symmetry plane is the  $(y, z)$ -plane. In Figure 7.11 (d) a corridor of low pressure can be seen near the  $(y, z)$ -plane, while in Figure 7.11 (e) and Figure 7.11 (f) the pressure further decreases near the cone tips of the suction valve pockets with the largest  $x$ -value.

Although no symmetry has been assumed in the flow solver, the results are pretty much symmetrical with respect to the  $(x, z)$ -plane. The influence of non-symmetrical valve pocket arrangements or the orientation of the structured cylinder mesh to the valve pocket geometry has not been investigated so far. Note, that all the presented results are just using  $n_1 = 15$  non-uniformly distributed cells along the piston radius. Even with this coarse mesh, the contours of the pressure are resolved with acceptable accuracy. Calculations performed with  $n_1 = 20$  along the piston radius do not show any remarkable difference to the shown results.



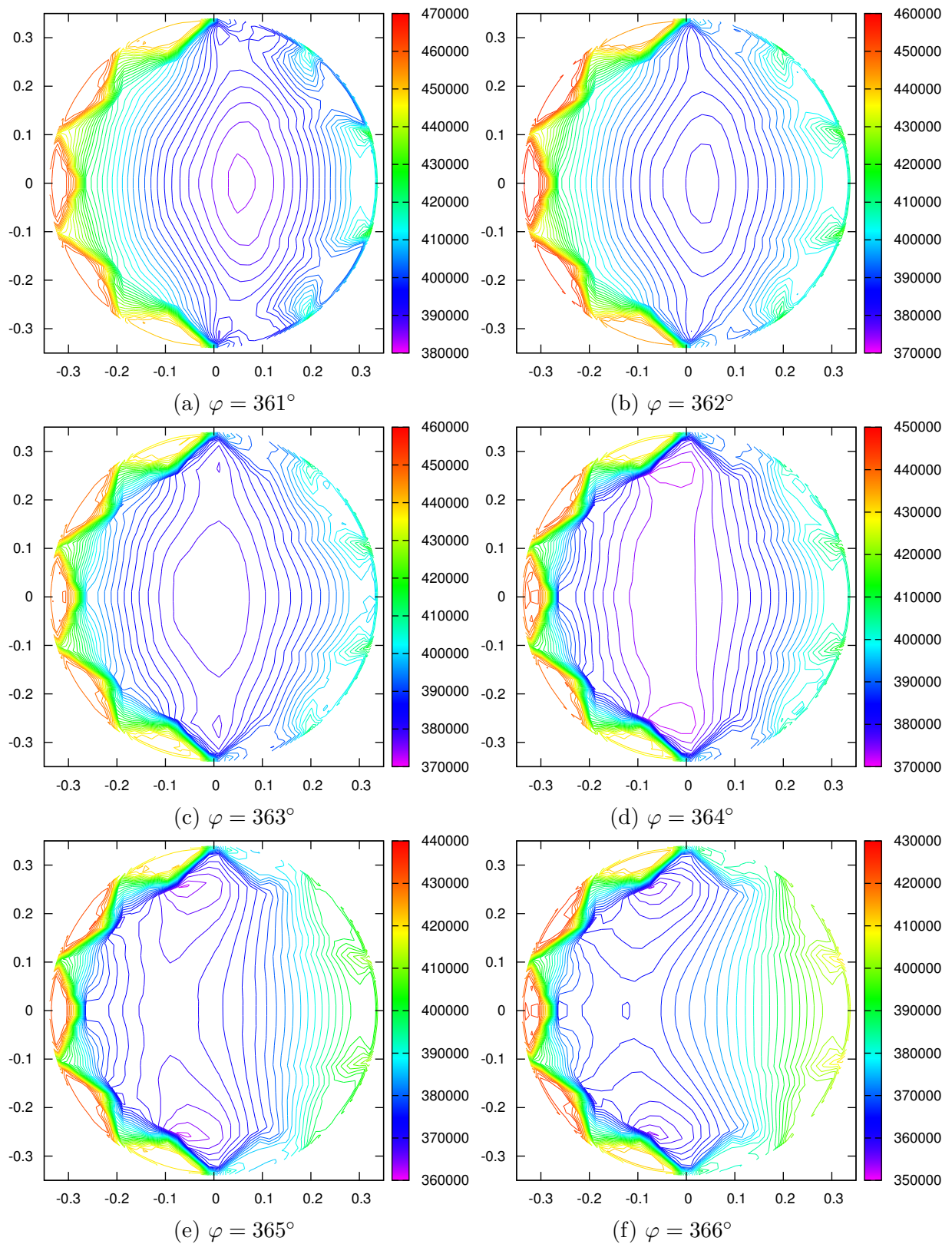


Figure 7.11: Pressure wave on piston after the pistons top-dead-center for a reciprocating compressor with piston diameter  $d_P = 680 \text{ mm}$  and 10 valves.

## 7.4.2 Velocity Distribution near the Piston

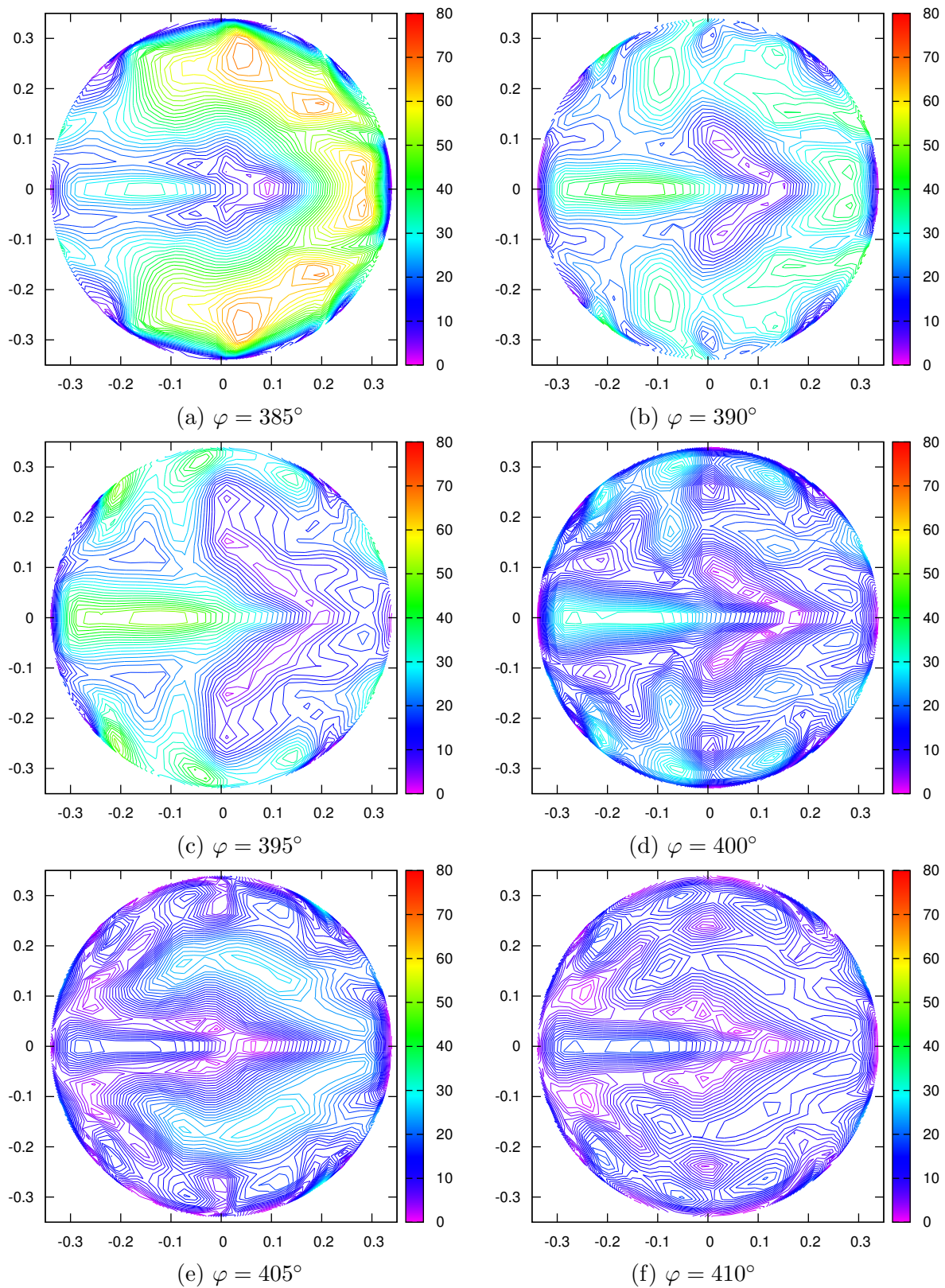


Figure 7.12: Velocity magnitude decay near the piston after discharge valve closing.

### 7.4.3 Mach-numbers for Subsonic and Supersonic Flow

In order to check if the solver can handle supersonic flows as well as subsonic flows for complex geometries, the rotational crank speed of the compressor with piston diameter  $d_P = 680\text{ mm}$  is increased from  $800\text{ rpm}$  to  $1200\text{ rpm}$ . The average piston speed for this compressor design with crank radius  $r = 75\text{ mm}$  increases from  $\bar{v}_P = 4\text{ m/s}$  to  $\bar{v}_P = 6\text{ m/s}$ .

In Figure 7.13 the maximal Mach numbers occurring inside the cylinder and in the valve pockets are plotted over crank angle for two compressor periods. The maximal Mach numbers during suction and discharge approximately follow the massflows crossing the suction valves and discharge valves. During suction, the Mach number goes up to the value 0.4 in the suction valve pockets and in the cylinder for the case running with  $800\text{ rpm}$ . Increasing the speed by 50% to  $1200\text{ rpm}$  does not increase the maximal Mach number during suction by the same factor. However, almost  $Ma = 0.55$  is obtained during suction due to increased piston velocity. The settings of the suction and discharge valves are the same for both compressor speeds, and the valve plate motion is maybe slightly different due to the increased rotational speed.

During discharge, the maximal Mach number obtained in the  $800\text{ rpm}$  case becomes slightly larger than 0.8. Hence, the flow solver only has to operate in the subsonic regime. On the other hand, for the case running with  $1200\text{ rpm}$  the Mach number during discharge becomes larger than one somewhere in the discharge valve pockets. Since the solver is suited to handle supersonic flows, the computation does not break. However, it is not recommended to run a compressor at Mach numbers larger than one, even if the supersonic flow occurs only on a small domain for a short time. The increased rotational speed is only used to demonstrate the ability of running supersonic simulations.

For a certain design operated at given conditions, the solver can be used to identify whether the flow is subsonic or supersonic during discharge. The higher mass delivery rate per rotation of a faster running compressor is an advantage, the appearance of supersonic flow can be a disadvantage. Design changes of the valve pocket geometries are maybe helpful to allow subsonic compressor operation even at high piston speeds. Since higher piston speeds are also a challenge for the design and the strength of the moving compressor parts, an average piston speed higher than  $\bar{v}_P = 6\text{ m/s}$  seems to be unrealistic also from this point of view. For compressors with smaller piston diameters, a similar behavior is expected, although not discussed herein.

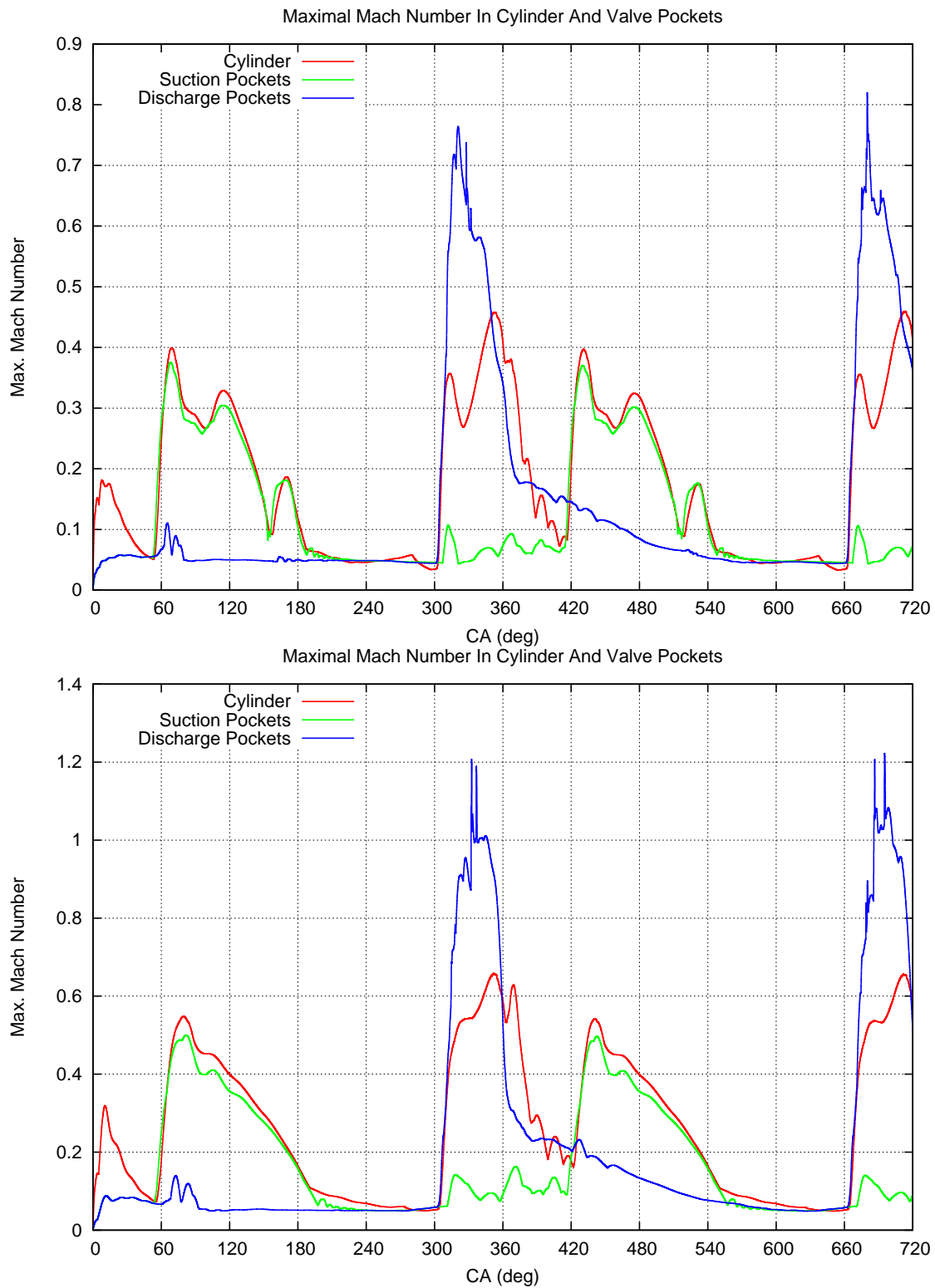


Figure 7.13: Maximal Mach number in cylinder, suction valve pockets and discharge valve pockets for a compressor with piston diameter  $d_P = 680\text{ mm}$  running with rotational crank speed  $800\text{ rpm}$  (top) and  $1200\text{ rpm}$  (bottom).

# Appendix A

## Roe 3D-Solver Derivation

### A.1 Basic Idea

The Roe method is an approximate Riemann solver used for the computation of numerical fluxes in finite volume schemes. The basic idea is to solve the linearized Euler equations locally at every face of a cell boundary. Since a constant in-cell reconstruction lets all physical quantities jump from a left state vector  $\mathbf{U}_L$  to a right state vector  $\mathbf{U}_R$  at the face, it is necessary to find an intermediate state vector  $\tilde{\mathbf{U}}$  used for the linearization of the set of partial differential equations. It can be expected, that the intermediate state lies somewhere in-between the value of the left and the right neighbor cell values.

The space and time-dependend solution of the linearized Euler equations adapted to the piecewise constant initial conditions can then be solved analytically using a decomposition in eigenvectors of the Jacobi matrix. As shown in Figure 6.1, two state vectors  $\mathbf{U}_L^*$ ,  $\mathbf{U}_R^*$  appear, that are separated by a contact discontinuity. For the linearized Euler equations the characteristics are straight lines in the space-time diagram, while for the fully non-linear Euler equations these lines are curved. The speed of the characteristics are the eigenvalues of the Jacobi matrix. The numerical flux computed by the Roe scheme makes use of  $\mathbf{U}_L^*$  and  $\mathbf{U}_R^*$ , derived in section A.4.

### A.2 Roe Condition

Although the Roe scheme was not derived this way in the original work of Roe [70], the Taylor series expansion at an unknown intermediate state  $\tilde{\mathbf{U}}$  performed by Roe and Pike [74] gives

$$\mathbf{f}_R = \mathbf{f}(\tilde{\mathbf{U}}) + \mathbf{A}(\tilde{\mathbf{U}}) \cdot (\mathbf{U}_R - \tilde{\mathbf{U}}) + \dots \quad (\text{A.1})$$

$$\mathbf{f}_L = \mathbf{f}(\tilde{\mathbf{U}}) + \mathbf{A}(\tilde{\mathbf{U}}) \cdot (\mathbf{U}_L - \tilde{\mathbf{U}}) + \dots \quad (\text{A.2})$$

where  $\mathbf{A} = \partial \mathbf{f} / \partial \mathbf{U}$  is the Jacobi matrix. Using Equation (3.20) for the sound speed  $c$  of ideal gas, and the flow velocity vector  $\mathbf{v} = [u, v, w]^\top$ , the Jacobi matrix reads

$$\mathbf{A} = \begin{bmatrix} 0 & 1 & 0 & 0 & 0 \\ -u^2 + \frac{\gamma-1}{2} \mathbf{v}^2 & (3-\gamma)u & (1-\gamma)v & (1-\gamma)w & \gamma-1 \\ -uv & v & u & 0 & 0 \\ -uw & w & 0 & u & 0 \\ -u \left[ \frac{c^2}{\gamma-1} + \left(1 - \frac{\gamma}{2}\right) \mathbf{v}^2 \right] & \frac{c^2}{\gamma-1} + \frac{1}{2} \mathbf{v}^2 - (\gamma-1)u^2 & (1-\gamma)uv & (1-\gamma)uw & \gamma u \end{bmatrix} \quad (\text{A.3})$$

Hence, for a given material equation, all entities in the matrix  $\mathbf{A}$  representing the linearized Euler equations can be expressed in the velocity components of the flow, and the velocity of the sound. The difference of Equation (A.1) and Equation (A.2)

$$\mathbf{f}_R - \mathbf{f}_L = \mathbf{A}(\tilde{\mathbf{U}}) \cdot (\mathbf{U}_R - \mathbf{U}_L) \quad (\text{A.4})$$

gives the implicit condition for the determination of the intermediate state  $\tilde{\mathbf{U}}$ , if  $\mathbf{U}_L$  and  $\mathbf{U}_R$  are given state-vectors from the neighbor cells adjacent to a face where a numerical flux is computed.

### A.3 Roe Averages

If the material equation for ideal gas is assumed, the flux vectors can also be expressed in terms of the flow velocity components and the speed of sound. In case of a three-dimensional situation Equation (A.4) gives five equations

$$\rho_R u_R - \rho_L u_L = \rho_R u_R - \rho_L u_L \quad (\text{A.5})$$

$$\begin{aligned} & \left( \rho_R u_R^2 + \frac{\rho_R c_R^2}{\gamma} \right) - \left( \rho_L u_L^2 + \frac{\rho_L c_L^2}{\gamma} \right) = \\ & \left[ -\tilde{u}^2 + \frac{\gamma-1}{2} (\tilde{u}^2 + \tilde{v}^2 + \tilde{w}^2) \right] (\rho_R - \rho_L) + (3-\gamma) \tilde{u} (\rho_R u_R - \rho_L u_L) \\ & \quad + (1-\gamma) \tilde{v} (\rho_R v_R - \rho_L v_L) + (1-\gamma) \tilde{w} (\rho_R w_R - \rho_L w_L) \\ & + (\gamma-1) \left[ \frac{\rho_R c_R^2}{\gamma(\gamma-1)} + \frac{\rho_R}{2} (u_R^2 + v_R^2 + w_R^2) - \frac{\rho_L c_L^2}{\gamma(\gamma-1)} - \frac{\rho_L}{2} (u_L^2 + v_L^2 + w_L^2) \right] \end{aligned} \quad (\text{A.6})$$

$$\rho_R u_R v_R - \rho_L u_L v_L = -\tilde{u} \tilde{v} (\rho_R - \rho_L) + \tilde{v} (\rho_R u_R - \rho_L u_L) + \tilde{u} (\rho_R v_R - \rho_L v_L) \quad (\text{A.7})$$

$$\rho_R u_R w_R - \rho_L u_L w_L = -\tilde{u} \tilde{w} (\rho_R - \rho_L) + \tilde{w} (\rho_R u_R - \rho_L u_L) + \tilde{u} (\rho_R w_R - \rho_L w_L) \quad (\text{A.8})$$

$$\begin{aligned} & \left[ \frac{\rho_R c_R^2}{\gamma-1} + \frac{\rho_R}{2} (u_R^2 + v_R^2 + w_R^2) \right] u_R - \left[ \frac{\rho_L c_L^2}{\gamma-1} + \frac{\rho_L}{2} (u_L^2 + v_L^2 + w_L^2) \right] u_L = \\ & \quad -\tilde{u} \left[ \frac{c^2}{\gamma-1} + \left(1 - \frac{\gamma}{2}\right) (\tilde{u}^2 + \tilde{v}^2 + \tilde{w}^2) \right] (\rho_R - \rho_L) \\ & \quad + \left[ \frac{c^2}{\gamma-1} + \frac{1}{2} (\tilde{u}^2 + \tilde{v}^2 + \tilde{w}^2) - (\gamma-1) \tilde{u}^2 \right] (\rho_R u_R - \rho_L u_L) \\ & \quad + (1-\gamma) \tilde{u} \tilde{v} (\rho_R v_R - \rho_L v_L) + (1-\gamma) \tilde{u} \tilde{w} (\rho_R w_R - \rho_L w_L) \\ & + \gamma \tilde{u} \left[ \frac{\rho_R c_R^2}{\gamma(\gamma-1)} + \frac{\rho_R}{2} (u_R^2 + v_R^2 + w_R^2) - \frac{\rho_L c_L^2}{\gamma(\gamma-1)} - \frac{\rho_L}{2} (u_L^2 + v_L^2 + w_L^2) \right] \end{aligned} \quad (\text{A.9})$$

Inserting

$$\tilde{v} = \frac{\rho_R u_R v_R - \rho_L u_L v_L + (\rho_L v_L - \rho_R v_R) \tilde{u}}{\rho_R u_R - \rho_L u_L + (\rho_L - \rho_R) \tilde{u}} \quad (\text{A.10})$$

from Equation (A.7) and

$$\tilde{w} = \frac{\rho_R u_R w_R - \rho_L u_L w_L + (\rho_L w_L - \rho_R w_R) \tilde{u}}{\rho_R u_R - \rho_L u_L + (\rho_L - \rho_R) \tilde{u}} \quad (\text{A.11})$$

from Equation (A.8) into Equation (A.6) gives a fourth order equation in  $\tilde{u}$  with four solutions

$$\tilde{u}_{1,2} = \frac{\rho_R u_R - \rho_L u_L \pm \sqrt{\frac{\gamma-1}{\gamma-3} \rho_R \rho_L [(v_R - v_L)^2 + (w_R - w_L)^2]}}{\rho_R - \rho_L} \quad (\text{A.12})$$

$$\tilde{u}_{3,4} = \frac{\rho_R u_R - \rho_L u_L \pm \sqrt{\rho_R \rho_L} (u_R - u_L)}{\rho_R - \rho_L} = \frac{\sqrt{\rho_R} u_R \mp \sqrt{\rho_L} u_L}{\sqrt{\rho_R} \mp \sqrt{\rho_L}} \quad (\text{A.13})$$

The root  $\sqrt{\frac{\gamma-1}{\gamma-3} \rho_R \rho_L [(v_R - v_L)^2 + (w_R - w_L)^2]}$  is not a real number if  $1 \leq \gamma \leq 3$ . Therefore,  $\tilde{u}_1$  and  $\tilde{u}_2$  from Equation (A.12) cannot be seen as general solutions. For  $\rho_R = \rho_L$  the expression  $\tilde{u}_3$  from Equation (A.13) becomes infinite, which excludes  $\tilde{u}_3$  from being a general solution as well. Hence, the only correct solution is  $\tilde{u} = \tilde{u}_4$ . Inserting this in Equation (A.10) and Equation (A.11) gives the so called Roe-averaging for the velocity components

$$\tilde{u} = \frac{\sqrt{\rho_R} u_R + \sqrt{\rho_L} u_L}{\sqrt{\rho_R} + \sqrt{\rho_L}}, \quad \tilde{v} = \frac{\sqrt{\rho_R} v_R + \sqrt{\rho_L} v_L}{\sqrt{\rho_R} + \sqrt{\rho_L}}, \quad \tilde{w} = \frac{\sqrt{\rho_R} w_R + \sqrt{\rho_L} w_L}{\sqrt{\rho_R} + \sqrt{\rho_L}} \quad (\text{A.14})$$

From (A.9) the intermediate sound-speed  $\tilde{c}$  becomes

$$\tilde{c}^2 = \frac{\sqrt{\rho_R} c_R^2 + \sqrt{\rho_L} c_L^2}{\sqrt{\rho_R} + \sqrt{\rho_L}} + \frac{\gamma - 1}{2} \frac{\sqrt{\rho_R} \sqrt{\rho_L} [(u_R - u_L)^2 + (v_R - v_L)^2 + (w_R - w_L)^2]}{(\sqrt{\rho_R} + \sqrt{\rho_L})^2} \quad (\text{A.15})$$

As a consequence, the total specific enthalpy

$$\tilde{H} = c_p \tilde{T} + \frac{1}{2} (\tilde{u}^2 + \tilde{v}^2 + \tilde{w}^2) = \frac{\tilde{c}^2}{\gamma - 1} + \frac{1}{2} (\tilde{u}^2 + \tilde{v}^2 + \tilde{w}^2) = \frac{\sqrt{\rho_R} H_R + \sqrt{\rho_L} H_L}{\sqrt{\rho_R} + \sqrt{\rho_L}} \quad (\text{A.16})$$

is also a Roe-average of the left and the right total specific enthalpies  $H_R$  and  $H_L$ .

### A.3.1 Eigenvalues and Eigenvectors

The basic concept how to find the eigenvalues and eigenvectors of a diagonalizable matrix is demonstrated in section 4.3.1. The eigenvalues  $\lambda$  and the right eigenvectors  $\mathbf{r}$  of the matrix  $\mathbf{A}$  are the solutions of the system

$$(\mathbf{A} - \lambda \mathbf{I}) \mathbf{r} = \mathbf{0} \quad (\text{A.17})$$

where  $\mathbf{I}$  is the identity matrix. All eigenvalues of the Roe-matrix  $\mathbf{A}(\tilde{\mathbf{U}})$  are

$$\lambda^{(1)} = \tilde{u} - \tilde{c}, \quad \lambda^{(2)} = \tilde{u}, \quad \lambda^{(3)} = \tilde{u}, \quad \lambda^{(4)} = \tilde{u}, \quad \lambda^{(5)} = \tilde{u} + \tilde{c} \quad (\text{A.18})$$

The eigenvalues determine the position of the characteristics in the space-time diagram, see Figure 6.1 for comparison. To each eigenvalue one can find an eigenvector  $\mathbf{r}$ . Collecting them in a matrix of right eigenvectors  $\mathbf{R} = [\mathbf{r}^{(1)}, \mathbf{r}^{(2)}, \mathbf{r}^{(3)}, \mathbf{r}^{(4)}, \mathbf{r}^{(5)}]$  gives the matrix

$$\mathbf{R} = \begin{bmatrix} 1 & 1 & 0 & 0 & 1 \\ \tilde{u} - \tilde{c} & \tilde{u} & 0 & 0 & \tilde{u} + \tilde{c} \\ \tilde{v} & \tilde{v} & 1 & 0 & \tilde{v} \\ \tilde{w} & \tilde{w} & 0 & 1 & \tilde{w} \\ \tilde{H} - \tilde{u}\tilde{c} & \frac{1}{2}\tilde{\mathbf{v}}^2 & \tilde{v} & \tilde{w} & \tilde{H} + \tilde{u}\tilde{c} \end{bmatrix} \quad (\text{A.19})$$

According to the example shown in section 4.3.2, the inverse matrix

$$\mathbf{R}^{-1} = \frac{\gamma - 1}{2\tilde{c}^2} \begin{bmatrix} \frac{1}{2}\tilde{\mathbf{v}}^2 + \frac{\tilde{u}\tilde{c}}{\gamma-1} & -u - \frac{\tilde{c}}{\gamma-1} & -\tilde{v} & -\tilde{w} & 1 \\ \frac{1}{2}\tilde{\mathbf{v}}^2 + \frac{2\tilde{c}^2}{\gamma-1} & 2\tilde{u} & 2\tilde{v} & 2\tilde{w} & -2 \\ -\frac{2\tilde{v}\tilde{c}^2}{\gamma-1} & 0 & \frac{2\tilde{c}^2}{\gamma-1} & 0 & 0 \\ -\frac{2\tilde{w}\tilde{c}^2}{\gamma-1} & 0 & 0 & \frac{2\tilde{c}^2}{\gamma-1} & 0 \\ \frac{1}{2}\tilde{\mathbf{v}}^2 - \frac{\tilde{u}\tilde{c}}{\gamma-1} & -\tilde{u} + \frac{\tilde{c}}{\gamma-1} & -\tilde{v} & -\tilde{w} & 1 \end{bmatrix} \quad (\text{A.20})$$

is required to find the vector of characteristic variables.

### A.3.2 Characteristic Variables

In contrast to section 4.3.2, where the vector of characteristic variables is denoted as  $\mathbf{v} = \mathbf{R}^{-1}\mathbf{U}$ , here the notation  $\mathbf{v} = \mathbf{R}^{-1}(\mathbf{U} - \mathbf{U}_L)$  is used instead. Because  $\mathbf{U}_L$  is a constant state vector from an adjacent cell, subtracting it from  $\mathbf{U}$  does not change the solution of the linearized systems of partial differential equations presented in Equation (4.18). However, the adaption to the initial conditions is easier, because inserting the left state vector  $\mathbf{U} = \mathbf{U}_L$  simply gives  $\mathbf{v}_L = \mathbf{0}$ , while adaption to the right state vector  $\mathbf{U} = \mathbf{U}_R$  gives  $\mathbf{v}_R = \boldsymbol{\alpha}$ , where

$$\boldsymbol{\alpha} = \mathbf{R}^{-1}(\mathbf{U}_R - \mathbf{U}_L) \quad (\text{A.21})$$

can be interpreted as wave strength vector, see e.g. Toro[81]. With the inverse matrix of Equation (A.20) based on Roe-averaged states, and  $p_R = \rho_R c_R^2/\gamma$ ,  $p_L = \rho_L c_L^2/\gamma$ ,  $\tilde{\rho} = \sqrt{\rho_R \rho_L}$ , one can write

$$\alpha_1 = \frac{1}{2\tilde{c}^2} [(p_R - p_L) - \tilde{c}\tilde{\rho}(u_R - u_L)] \quad (\text{A.22})$$

$$\alpha_2 = \frac{1}{\tilde{c}^2} [\tilde{c}^2(\rho_R - \rho_L) - (p_R - p_L)] \quad (\text{A.23})$$

$$\alpha_3 = \tilde{\rho}(v_R - v_L) \quad (\text{A.24})$$

$$\alpha_4 = \tilde{\rho}(w_R - w_L) \quad (\text{A.25})$$

$$\alpha_5 = \frac{1}{2\tilde{c}^2} [(p_R - p_L) + \tilde{c}\tilde{\rho}(u_R - u_L)] \quad (\text{A.26})$$

for the entities in the wave strength vector  $\boldsymbol{\alpha} = [\alpha_1, \alpha_2, \alpha_3, \alpha_4, \alpha_5]$ .



## A.4 Intermediate States

According to Equation (4.20), the solution of the linear PDE-system can be composed using the vector of characteristic variables and the eigenvectors

$$\Delta \mathbf{U} = \sum_{i=1}^5 \alpha_i \mathbf{r}^{(i)} \quad (\text{A.27})$$

where  $\Delta \mathbf{U}$  denotes the change of the state vector  $\mathbf{U}$ , when jumping across a characteristic. Hence, as illustrated in Figure 6.1, the intermediate state vectors  $\mathbf{U}_L^*$  and  $\mathbf{U}_R^*$  can be computed

$$\mathbf{U}_L^* = \mathbf{U}_L + \alpha_1 \mathbf{r}^{(1)} \quad (\text{A.28})$$

$$\mathbf{U}_R^* = \mathbf{U}_R - \alpha_5 \mathbf{r}^{(5)} \quad (\text{A.29})$$

Note, that according to Equation (A.18), the eigenvalues  $\lambda^{(2)}$ ,  $\lambda^{(3)}$ ,  $\lambda^{(4)}$  have the identical value  $\tilde{u}$ . Hence, the three characteristics represented by these eigenvalues melt together to a single curve in the space-time diagram.

For the computation of the numerical flux, the Roe method does not use  $\mathbf{f}(\mathbf{U}_L^*)$  and  $\mathbf{f}(\mathbf{U}_R^*)$  directly. Instead, a similar form of Equation (A.4) is used to find the intermediate fluxes, see Equation (6.6) for non-moving mesh. Therefore, the numerical flux computation is sometimes termed as flux difference splitting method.

# Appendix B

## Solver Testing

### B.1 Motivation

The development of a three-dimensional finite volume solver for the Euler equations based on structured hexahedral mesh is not very difficult, if the method is restricted to a first order accurate approximate Riemann solver. If an explicit time-intergration technique is used, problems are usually concerned with stability, especially on distorted meshes. However, numerical tests on both regular and distorted meshes with different time step size indicate, that the positivity criterion discussed in section 6.5 gives a good hint, where the stability limit can be expected for upwind-orientated methods.

On the other hand, the development of a three-dimensional solver based on tetrahedral mesh offers a lot of challanges. The unstructured nature of such a method is a possible source of code implementation failures. Therefore, it is necessary to perform extensive solver testing before using it for a complex valve pocket geometry of a reciprocating compressor with additional difficulties arising from the boundary conditions at valves or the non-conforming interfaces to the cylinder mesh. As a first step, simple tests have to be considered to check, if the basic properties expected from the solver either work or not. The conservation property of the finite volume method can be used to show, that the mass and the total inner energy inside a completely closed non-moving computational domain do not change with respect to time, for any flow that eventually appears due to some arbitrary initial conditions.

Therefore, four different tetrahedral meshes of valve pockets shown in Figure B.1 have been created, to check if mass and total inner energy inside the computational domains are conserved, if the surfaces are all set as wall boundary conditions. This valve pocket meshes are also used for the calculations with the full compressor models. Hence, the different diameters of the piston  $d_P = 680\text{ mm}$ ,  $d_P = 340\text{ mm}$ ,  $d_P = 170\text{ mm}$ ,  $d_P = 85\text{ mm}$  have to be considered already in the pocket geometry design. Note, that the valve diameters  $d_V = 200\text{ mm}$ ,  $d_V = 125\text{ mm}$ ,  $d_V = 80\text{ mm}$ ,  $d_V = 54\text{ mm}$  are also decreasing with smaller piston diameters. Therefore, for the smaller valve pockets smaller cell sizes are used as well. However, the number of

tetrahedral cells 1203, 1271, 1813, 2066 is slightly growing for the smaller pockets.

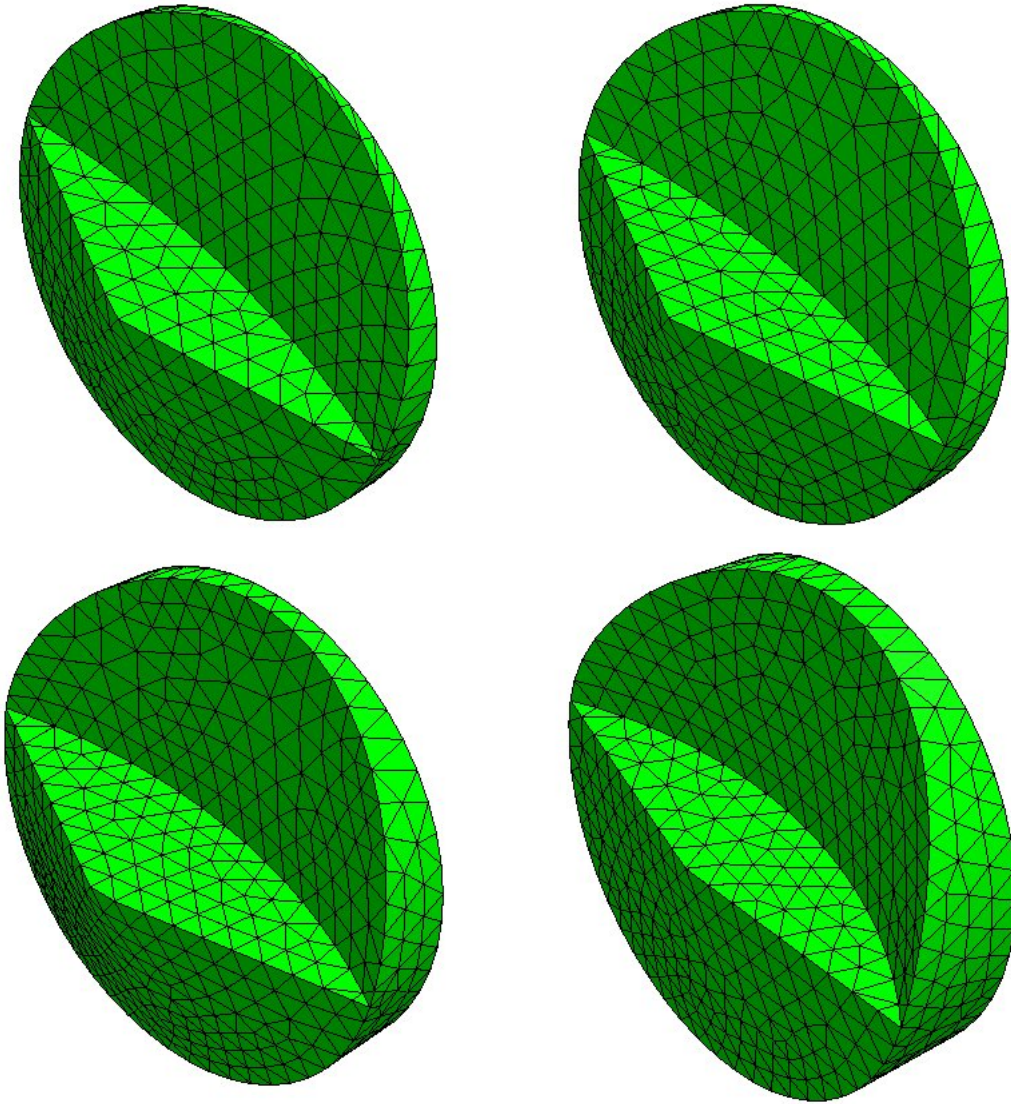


Figure B.1: Tetrahedra meshes of valve pocket geometries capable to match with piston diameters  $d_P = 680 \text{ mm}$  (top left),  $d_P = 340 \text{ mm}$  (top right),  $d_P = 170 \text{ mm}$  (bottom left) and  $d_P = 85 \text{ mm}$  (bottom right).

On the other hand, tests with completely closed complex geometries only indicate a correct implementation of the wall boundary conditions, and that every numerical flux through an inner face that leaves a cell, enters the neighbor cell of that face with the same strength. However, it cannot be verified with such tests, that the numerical flux is physically correct in terms of approximating solutions of the Euler equations. Therefore, a test is set up, where the solution of the Euler equations is known, and the accuracy of the results can be compared with a similar one-dimensional situation.

## B.2 Modified Shock Tube Test

### B.2.1 Test Case Description

In order to test a numerical method, in Toro [81] a modification of the classical shock tube example given by Sod is presented. At initial conditions, the shock tube consists of a straight pipe containing two zones with fluid at rest, separated by a thin membrane. The two fluid zones on both sides of the membrane have different density and pressure at the beginning. After the membrane is torn, a supersonic flow can occur, depending on the initial data. Hence, this configuration seems to be optimal to test a numerical solver with the capability to solve subsonic and supersonic flows. The so-called Toro test case 1 additionally allows, that the fluid at the beginning of the test has a flow velocity. For the testing of 1d-solvers, Toro [81] proposes the initial conditions listed in Table B.1 for a pipe with a length of  $1\text{ m}$ .

	$\rho\text{ (kg/m}^3\text{)}$	$u\text{ (m/s)}$	$v\text{ (m/s)}$	$w\text{ (m/s)}$	$p\text{ (Pa)}$
$0.0\text{ m} \leq x \leq 0.3\text{ m}$ :	1	0.75	0	0	1
$0.3\text{ m} < x \leq 1.0\text{ m}$ :	0.125	0	0	0	0.1

Table B.1: Initial conditions for the 1d shock tube test of Toro[81].

The velocity components  $v$  and  $w$  are not relevant for the 1d-solver testing, but are necessary for testing the 3d-solver. The fluid is assumed to be ideal gas with a specific heat capacity ratio  $\gamma = 1.4$ . Hence, the speed of sound  $c = \sqrt{\gamma p/\rho}$  obtained for  $x \leq 0.3\text{ m}$  is  $c = 1.183\text{ m/s}$  and  $c = 1.058\text{ m/s}$  for  $x > 0.3\text{ m}$ . The Mach number  $Ma = 0.634$  for  $x \leq 0.3\text{ m}$  shows, that the flow is subsonic at the beginning, but it will turn into supersonic flow right after the membrane is broken.

### B.2.2 3D-Model Setup

In order to test the three-dimensional solver for Euler equations, the one-dimensional Toro test case 1 is solved with a three-dimensional tube model. The results presented in Toro [81] at time  $t = 0.2\text{ s}$  are obtained with a 1d-version of the Roe approximate Riemann solver with an additional sonic entropy fix to avoid the wrong solutions near  $Ma = 1$ . The 1d-results for the Toro test case 1 shown in Figure B.4 are calculated with exactly the same 1d-solver explained in Toro [81]. In the 1d-situation, the mesh consists of 100 equi-sized cells along the pipe length of  $1\text{ m}$ , having a cell size of  $\Delta x = 0.01\text{ m}$ . In order to compare the accuracy of the 3d Roe-solver with the 1d-results, a 3d-mesh of a tube with a diameter of  $0.1\text{ m}$  and a length of  $1\text{ m}$  is created, consisting of 17080 tetrahedral cells. The surface mesh of the 3d-tube is shown in Figure B.2.

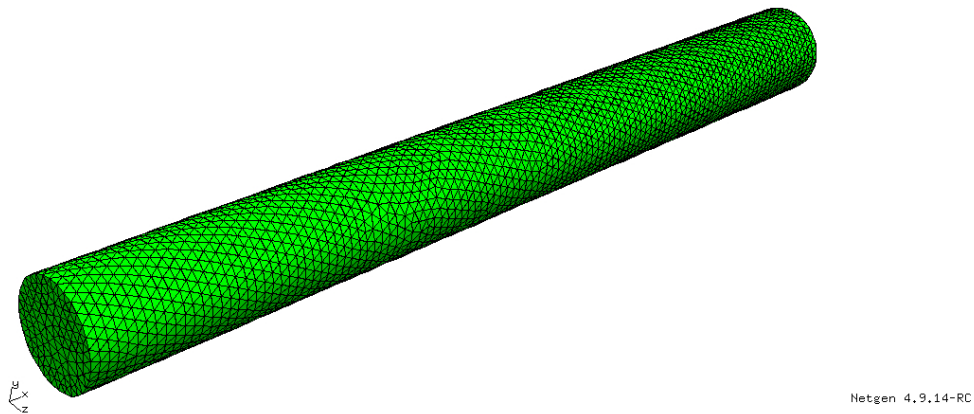


Figure B.2: Surface mesh of the 3d shock tube test model with a length of  $1\text{ m}$  and a diameter of  $0.1\text{ m}$ , consisting of 17080 tetrahedral cells.

The size of the tetrahedral cell is chosen in such a way, that approximately the same accuracy can be expected as in the 1d-situation with cell size  $\Delta x = 0.01\text{ m}$ . A detailed view on the surface mesh in Figure B.3 shows, that the tetrahedral mesh was not created by subdividing the pipe in 100 sectors in  $x$ -direction, that are meshes afterwards. Since the mesh of the 3d-tube was created with an advancing front mesh generator, the mesh on the surface and inside the domain can really have any irregularity in terms of node positions and face directions.

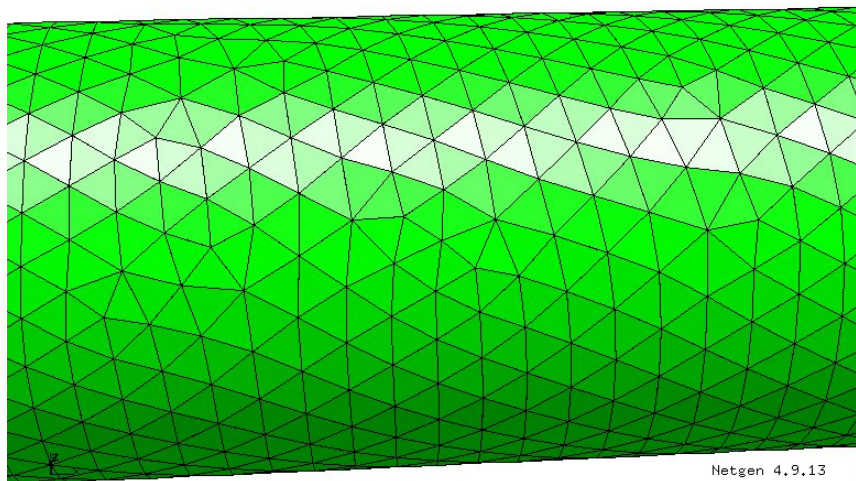


Figure B.3: Detailed view on the surface mesh of the 3d shock tube test model.

### B.2.3 Comparison 1d/3d-Results

Goal of the comparison of the 1d-version and the 3d-version of the Roe approximate Riemann solver is to show, that both methods give nearly the same results with comparable accuracy. In Figure B.4, density,  $x$ -velocity component and pressure of the gas are plotted in every cell mid-point of the 1d-mesh and the 3d-mesh at time  $t = 0.2 s$ . Similar to the description in Toro [81] for the test case 1, a Courant number  $C = 0.9$  is used for the 1d-calculation. Since for the 1d-situation the cell size  $\Delta x = 0.01 m$  is relevant for determining the timestep size, only 60 timesteps are necessary to reach the time  $t = 0.2008610 s$ , plotted in Figure B.4. On the other hand, for the 3d-calculation based on 17080 tetrahedral cells and the same Courant number  $C = 0.9$ , 371 timesteps are required to reach the plotted computation time  $t = 0.1999925 s$ .

The reason for that large difference in required timesteps is the length scale that determines the timestep size. While in the 1d-case this length is clearly  $\Delta x$ , in the 3d-case the radius  $R$  of a sphere inscribed in every tetrahedron is used for that length. It is commonly thought, that the choice of  $R$  is sufficient to guarantee stability on even highly distorted tetrahedral meshes, because a wave travelling from the center of every tetrahedron cannot reach any tetrahedra face if the Courant number fulfills  $C < 1$ . However, to the knowledge of the author, a proof for the stability concerning the Euler equations is not known. Nevertheless, for the three-dimensional advection equation with constant wave speeds, a positivity criterion exists, showing that for the first order upwind scheme this length must be smaller than one third of the smallest tetrahedra height. Since for a regular tetrahedron  $R$  is one fourth of the height, the chosen criterion based on  $R$  is assumed to be at least stronger than the criterion using one third of the height for the length scale.

Another important point is the way how the Riemann problem is solved. As already stated in section 6.2, a so-called grid-aligned rotated Riemann solver is used, as it is presented in Toro [81]. Hence, for the numerical flux computation, the decomposition of the waves occurring at the discontinuities at cell boundaries is performed in the direction of the face-normal. However, as can be seen in Figure B.3, the cell faces on the surface and on the inside of the computation domain may have any arbitrary direction. While for the 1d-case the grid-normal vector is always normal to the shock, this is definitely not the case for the 3d tetrahedral mesh. Anyway, the results in Figure B.4 demonstrate that the implemented method works with the same accuracy as the 1d Roe solver. Further improvements can be expected, by extending the 2d-version of a solution-aligned rotated Riemann solver shown in Ren [67] to three space dimensions.

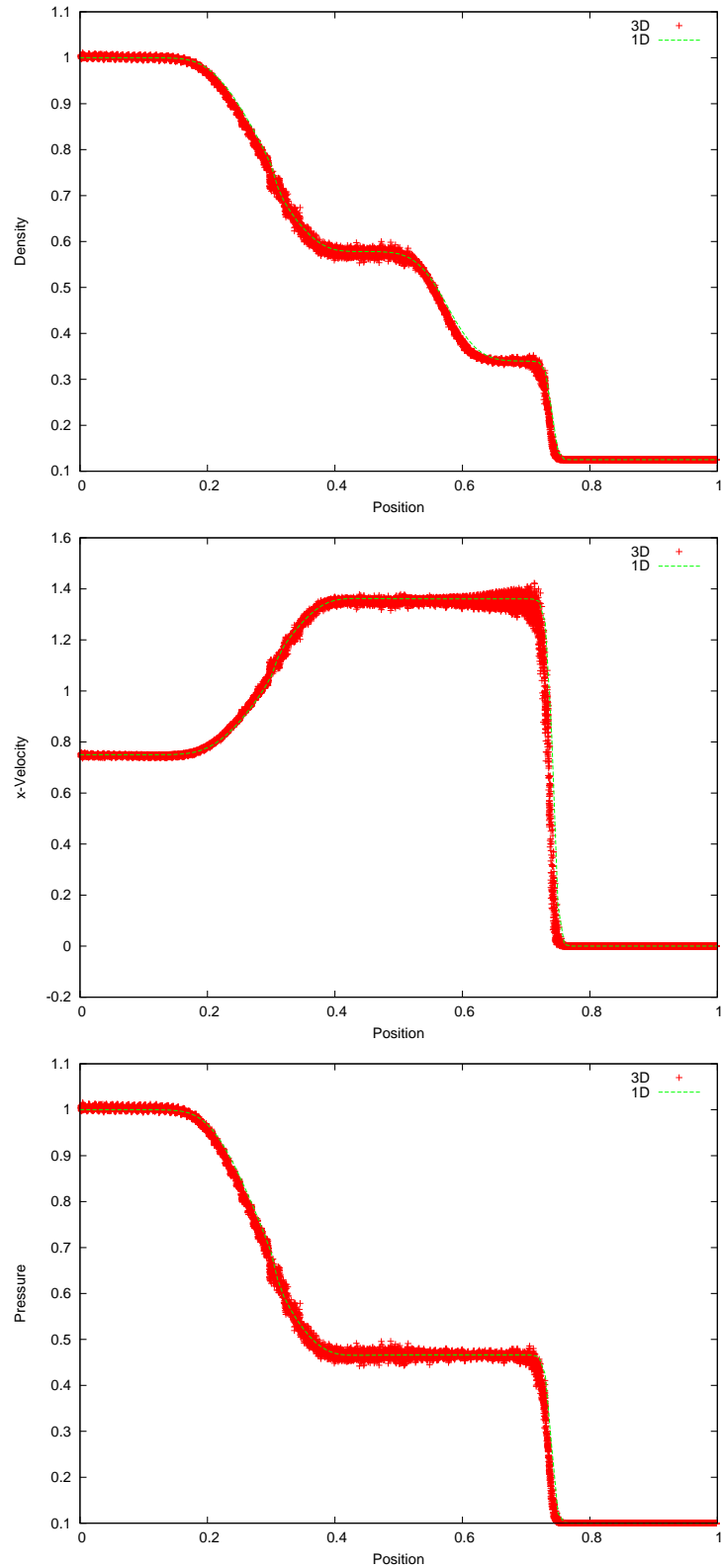


Figure B.4: One-dimensional shock tube test of Toro [81] at time  $t = 0.2$  s, solved with a 1d-version and a 3d-version of the Roe approximate Riemann solver with sonic entropy fix: density (top),  $x$ -velocity component (middle), and pressure (bottom) at every cell mid-point.

# Bibliography

- [1] Abidin, Z., Almbauer, R. A., Burgstaller, A., Nagy, D. (2007): Assessment Method for the Thermodynamic Quality of Parts of a Hermetic Piston Compressor. International Conference on Compressors and their Systems, IMechE.
- [2] Adair, R. P., Qvale, E. B., Pearson, J. T. (1972): Instantaneous Heat Transfer to the Cylinder Wall on Reciprocating Compressors, Proc. Purdue Compressor Technology Conference, 521-526.
- [3] Aigner, R., Steinrück, H. (2004): Waves in reciprocating compressors. PAMM Proceedings in Applied Mathematics and Mechanics, 4(1), 516-517.
- [4] Aigner, R., Meyer, G., Steinrück, H. (2005): Valve Dynamics and Internal Waves in a Reciprocating Compressor. Proceedings of 4th EFRC Conference, 169-178.
- [5] Aigner, R., Steinrück, H. (2007): Modelling Fluid Dynamics, Heat Transfer and Valve Dynamics in a Reciprocating Compressor. Proceedings of 5th EFRC Conference, 169-178.
- [6] Aigner, R. (2007): Internal Flow and Valve Dynamics in a Reciprocating Compressor. Dissertation, Technische Universität Wien.
- [7] Annand, W. J. D. (1963): Heat Transfer in the Cylinders of Reciprocating Internal Combustion Engines, Proc. Instn. Mech. Engrs., vol. 117, 973-996.
- [8] Arora, M. and Roe, P. L (1997): A well-behaved TVD limiter for high-resolution calculations of unsteady flow. H. Comput. Phys. (1), 3-11.
- [9] Baehr, H. D. (1996): Thermodynamik. Eine Einführung in die Grundlagen und ihre technischen Anwendungen. Springer.
- [10] Baehr, H. D., Stephan, K. (2004): Wärme- und Stoffübertragung. Springer.
- [11] Birari, Y. V. Gosavi, S. S., Jorwekar, P. P. (2006): Use of CFD in Design and Development of R404A Reciprocating Compressor. Int. Compressor Engineering Conference at Purdue.
- [12] Bloch, H. P., Hoefner, J. J. (1996): Reciprocating Compressors: Operation & Maintenance. Gulf Professional Publishing.
- [13] Böswirth, L. (1994): Strömung und Ventilplattenbewegung in Kolbenverdichterventilen. Eigenverl. L. Böswirth.
- [14] Brun, K., Nored, M., Gernentz, R. S., Platt, J. P. (2005): Reciprocating Compressor Valve Plate Life and Performance Analysis. Gas Machinery Conference 2005, Covington, Kentucky.
- [15] Burgstaller, A. (2009): Ansätze zu thermodynamischen Analysen und Bewertung von hermetisch verschlossenen Systemen am Beispiel von Kleinkältemittelkompressoren. Dissertation, Technische Universität Graz.
- [16] Cada, M., Torrilhon (2009): Compact third-order limiter functions for finite volume methods J. Comput. Physics, 228, 4118-4145
- [17] Challis, J. (1848): On the Velocity of Sound, Phil. Mag., 32, [III], 494-499.



- [18] Costagliola, M. (1950): The Theory for Spring Loaded Valves for Reciprocating Compressors. *J. Appl. Mech.*, 415-420.
- [19] Christoffel, E. B. (1877): Untersuchungen über die mit dem Fortbestehen linearer partieller Differentialgleichungen verträglichen Unstetigkeiten. *Ann. Mat. (2)* 8, 81-113, 51-80
- [20] Cyklis, P. (1994): CFD Simulation of the Flow Trough Reciprocating Compressor Self-Acting Valves. *Int. Compressor Engineering Conference at Purdue*.
- [21] Després, B. and Lagoutière, F. (2001): Contact discontinuity capturing schemes for linear advection and compressible gas dynamics. *J. Sci. Comput. (4)*, 479-524.
- [22] Disconzi, F. P., Pereira, E. L. L., Deschamps C. J. (2012): Development of an In-Cylinder Heat Transfer Correlation for Reciprocating Compressores. *Int. Compressor Engineering Conference at Purdue*.
- [23] Drikakis D. (2007): Symmetry Bifurcation and Instabilities, in Grinstein, F. F., Margolin L. G., Rider W. J. (2007): *Implicit Large Eddy Simulation: Computing Turbulent Fluid Dynamics*. Cambridge University Press., 292-300.
- [24] Drikakis, D., Hahn, M., Grinstein, F., DeVore, C. R., Fureby, C., Liefvendahl, M., Youngs, D., Numerics for ILES, in Grinstein, F. F., Margolin L. G., Rider W. J. (2007): *Implicit Large Eddy Simulation: Computing Turbulent Fluid Dynamics*. Cambridge University Press., 94-128.
- [25] Einfeldt, B. (1988): On Godunov-Type Methods for Gas Dynamics. *SIAM J. Numer. Anal.* 25,294-318.
- [26] Einfeldt, B., Munz, C. D., Roe P. L., Sjögreen B. (1991): On Godunov-Type Methods near Low Densities. *J. Comput. Phys.* 92, 273-295.
- [27] Fahs, H. (2013): High-order discontinuous Galerkin method for time-domain electromagnetics on non-conforming hybrid meshes. Preprint submitted to Elsevier.
- [28] Ferziger, J. H., Perić, M. (2002): *Computational Methods for Fluid Dynamics*. Springer Berlin Heidelberg.
- [29] Flade, G. (2006): Weiterentwicklung der Berechnungsmethoden für Kobenverdichterventile auf der Basis zweidimensionaler Strömungssimulation. Dissertation, Technische Universität Dresden.
- [30] Godunov, S. K. (1959): A difference method for numerical calculation of discontinuous solutions of the equations of hydrodynamics, *Mat. Sb.*, 47, pp. 271-306
- [31] Goodman, J. B., LeVeque R. J. (1985): On the Accuracy of Stable Schemes for 2D Scalar Conservation Laws. *Mathematics of Computation*, Volume 45, Number 171, 15-21.
- [32] Grinstein, F. F., Margolin L. G., Rider W. J. (2007): *Implicit Large Eddy Simulation: Computing Turbulent Fluid Dynamics*. Cambridge University Press.
- [33] Hadamard, J. (1903): *Leçons sur la Propagation des Ondes et les Équations de l'Hydrodynamique*. Hermann & Cie., Paris. Re-issued (1949) by Chelsea Publishing Company, New York.
- [34] Hugoniot, H. (1887): Mémoire sur la propagation du mouvement dans les corps et plus spécialement dans les gaz parfaits, 1<sup>e</sup> Partie, I. *Journal de l'École Polytechnique (Paris)*, 57, 3-97
- [35] Hugoniot, H. (1889): Mémoire sur la propagation du mouvement dans les corps et plus spécialement dans les gaz parfaits, 2<sup>e</sup> Partie, I. *Journal de l'École Polytechnique (Paris)*, 58, 1-125
- [36] Harten, A. (1983): High Resolution Schemes for Hyperbolic Conservation Laws. *J. Comp. Phys.* 49, 357393.

- [37] Harten, A., Lax, P. D., van Leer, B. (1983): On upstream differencing and Godunov-type schemes for hyperbolic conservation laws. *SIAM Rev.* 25, 35-61.
- [38] Hirsch, C. (1992): Numerical Computation of internal and external flows. Fundamentals of numerical discretization. John Wiley & Sons.
- [39] Hirsch, C. (1992): Numerical Computation of internal and external flows. Computational methods for inviscid and viscous flows. John Wiley & Sons.
- [40] Hussaini, M. Y., van Leer, B., Van Rosendale, J. (Eds), (1997): Upwind and High-Resolution Schemes. Collection of reprinted ICASE reports, Springer.
- [41] Jeng, Y. N. and Payne, U. J. (1995): An adaptive TVD limiter. *J. Comput. Phys.* (2), 229-241
- [42] Kemm, F. (2011): A comparative study of TVD limiters – well known limiters and an introduction of new ones. *Internat. J. Numer. Methods Fluids* 67 (4), 404-440.
- [43] Kerpicci, H., Oguz, E. (2006): Transient Modeling of Flows Through Suction Port and Valve Leaves of Hermetic Reciprocating Compressors. *Int. Compressor Engineering Conference at Purdue*.
- [44] Kotchine, N. E. (1926): Sur la théorie des ondes de choc dans un fluide. *Rend. Circ. Mater. Palermo*, 50, 305-344.
- [45] Koop, L. (2012): Design and manufacturing of a new large bore compressor cylinder. *Proceedings of Int. Rotating Equipment Conference*, 165-171.
- [46] Kopsick G. M. (2004): Application and operating history of moderate-speed API 618 reciprocating compressors. *Proceedings of the thirty-third turbomachinery symposium*.
- [47] Küttner, K. -H. (1992): *Kolbenverdichter*. Springer.
- [48] Laney, Culbert B. (1998): *Computational Gasdynamics*. Cambridge University Press.
- [49] Lax, P. D., Wendroff, B. (1960): System of Conservation Laws. *Comp. Pure and Appl. Math.*, 13, 217-237.
- [50] Leveque, R. J. (1999): *Numerical Methods for Conservation Laws*. Birkhäuser.
- [51] Leveque, R. (2002): *Finite Volume Methods for Hyperbolic Problems*. Cambridge University Press.
- [52] Machu, E. (1998): Problems with modern high speed short stroke reciprocating compressors: Increased power requirement due to pocket losses, piston masking and gas inertia, eccentric gas load on the piston. *Proceedings of Gas machinery conference USA*.
- [53] Machu, G. (2004): Calculating reliable impact valve velocity by mapping instantaneous flow in a reciprocating compressor. *Proceedings of gas machinery conference GMRC USA*.
- [54] Machu, G. (2005): Pulsationen im Verdichtungsraum - eine potentielle Schadensursache. *Industriepumpen und Kompressoren Heft 2/2005* Vulkann Verlag Essen, Mai 2005.
- [55] Machu, G., Albrecht, M., Bielmeier, O., Daxner, T., Steinrück, P. (2004): A universal simulation tool for reed valve dynamics. *17th Int. Compressor Engineering Conference at Purdue*, C045.
- [56] Marie P.H., De Buhan M., Diaz A., Dobrzynski C., Kluth G., Lagoutiere F. (2008): A Cell-Centered Arbitrary Lagrangian Eulerian (ALE) Method For Multi-Material Compressible Flows. *ESAIM: PROCEEDINGS*, 24, 1-13, Editors: C. Dobrzynski, P. Frey, Ph. Peday.
- [57] Manfrone, F., Raggi, A. (2012): Analysis of the Movements of the Valve Sealing Elements. *Proceedings of Int. Rotating Equipment Conference*, 146-155.

- [58] Matos, F. F. S., Deschamps, C. J., Prata, A. T. (2006): A two-dimensional simulation model for reciprocating compressors with automatic valves. Proc. Int. Compressor Engineering Conference at Purdue, C-053, 8 p.
- [59] Meyer, G. (2004): Simulation der Strömung in einem Kolbenverdichter. Diplomarbeit, Technische Universität Wien.
- [60] Müllner, T., Bielmeier O. (2008): Heat transfer in small piston compressors. Int. Compressor Engineering Conference at Purdue.
- [61] Nishikawa, H., Kitamura. K. (2008): Very simple, carbuncle-free, boundary-layer-resolving, rotated-hybrid Riemann solvers. J. Comput. Phys. 227: 2560-2581.
- [62] Pereira, E. L. L, Deschamps, C. J., Ribas, F. A. (2008): A Comparative Analysis of Numerical Simulation Approaches for Reciprocating Compressors. Int. Compressor Engineering Conference at Purdue.
- [63] Pereira, E. L. L, Deschamps, C. J., Ribas, F. A. (2010): Numerical Analysis of Heat Transfer inside the Cylinder of Reciprocating Compressors in the Presence of Suction and Discharge Processes, Int. Compressor Engineering Conference at Purdue.
- [64] Pratelli, G., Babbini, A., Balduzzi, F., Ferrara, G., Maleci, R., Romani, L. (2012): CFD Evaluation of Pressure Losses on Reciprocating Compressor Components. Proceedings of Int. Rotating Equipment Conference, 33-41.
- [65] Quirk, J. J. (1994): A Contribution to the Great Riemann Solver Debate. Int. J. Numer. Meth. Fluids 18: 555-574.
- [66] Rankine, W. J. M. (1870): On the Thermodynamic Theory of Waves of Finite Longitudinal Disturbance, Philosophical Transactions, London/Edinburgh, Band 160, 270-288.
- [67] Ren Y.-X. (2003): A robust shock-capturing scheme based on rotated Riemann solvers. Computers & Fluids 32, 1379-1403.
- [68] Ribas, F. A., Deschamps C. J. (2006): A Simplified Numerical Methodology for the In-Cylinder Flow at the Top-Center Crank Position. Int. Compressor Engineering Conference at Purdue.
- [69] Riemann, B. (1860): Über die Fortpflanzung ebener Luftwellen von endlicher Schwingungsweite, Abhandlungen der Gesellschaft der Wissenschaften zu Göttingen, Mathematisch-physikalische Klasse, 8, 43.
- [70] Roe, P. L. (1981): Approximate Riemann Solvers, Parameter Vectors, and Difference Schemes. J. Comp. Phys. 43, 357-372.
- [71] Roe, P. L. (1986): Discrete Models for the Numerical Analysis of Time-Dependent Multidimensional Gas Dynamics. J. Comp. Phys. 63, 458-476.
- [72] Roe, P. L. (1986): Characteristic-Based Schemes for the Euler Equations. Ann. Rev. Fluid Mech. 337-365.
- [73] Roe, P. L. and Baines, M. (1982): Algorithms for advection and shock problems. Numerical methods in fluid mechanics, Proc. 4th GAMM-Conf., Paris 1981, Notes Numer. Fluid Mech. 5, 281-290.
- [74] Roe, P. L., J. Pike (1984) Efficient Construction und Utilisation of Approximate Riemann Solutions. Computing Methods in Applied Science and Engineering. North-Holland.
- [75] Rovaris, J. B., Deschamps, C. J. (2005) A Hybrid Simulation Methodology for Reciprocating Compressors. Proc. International Conference on Compressors and Their Systems, London: 183-192.
- [76] Rusanov, V. V. (1961): Calculation of interaction of non-steady shock waves with obstacles. J. Comput. Math. Phys. USSR 1, 267-279.

- [77] Serre, D. (1999): Systems of conservation laws 1. Hyperbolicity, Entropies, Shock Waves. Cambridge University Press.
- [78] Stokes, G.G. (1848): On a difficulty in the theory of sound. The London, Edinburgh, and Dublin Philosophical Magazine and Journal of Science, 33, London, 349-356
- [79] Tannehill, J. C., Anderson, D. A., Pletcher, R. H. (1997): Computational fluid mechanics and heat transfer. Taylor and Francis.
- [80] Toro, E. F., Clarke, J. F. (1998): Numerical methods for Wave Propagation. Kluwer Academic Publishers.
- [81] Toro, E. F., (1999): Riemann Solvers and Numerical Methods for Fluid Dynamics. Springer.
- [82] Toro, E. F., Spruce, M. & Speares, W. (1994): Restoration of the contact surface in the HLL-Riemann solver. Shock Waves J. 4, 25-34.
- [83] van Leer, B. (1982): Flux-Vector Splitting for the Euler Equations. Lecture note in Physics, Vol. 170, Springer.
- [84] Truesdell, C., Toupin, R.A. (1960). The classical field theories. Encyclopedia of Physics, Vol III/1, (Ed.: S. Flgge), pp. 226-858, Springer-Verlag, Berlin.
- [85] Wilson, D. B. (1990), The Correspondance Between Sir George Gabriel Stokes and Sir William Thomson, Baron Kelvin of Largs, Cambridge University Press, Cambride, GB, Vol. I 1846-1869
- [86] Wilson, D. B. (1990), The Correspondance Between Sir George Gabriel Stokes and Sir William Thomson, Baron Kelvin of Largs, Cambridge University Press, Cambride, GB, Vol. II 1846-1869
- [87] Woschni, G. (1976): Universally Applicable Equation for the Instantaneous Heat Transfer Coefficient in the Internal Combustion Engine. SAE Transactions, vol. 76, SAE paper 670931.

# Curriculum Vitae

## Personal Data

Name: Thomas Müllner  
Nationality: Austria  
Date of Birth: April 3<sup>rd</sup>, 1979  
E-mail: thomas.muellner@tuwien.ac.at

## Education

02/2008 - present Vienna University of Technology, Austria  
Institute of Fluid Mechanics and Heat Transfer  
Doctorate in Mechanical Engineering

10/1999 - 02/2008 Vienna University of Technology, Austria  
Graduated in Mechanical Engineering  
Diploma Thesis: "Calculation of Heat Transfer  
Coefficients in the Packings of Reciprocating Compressors"

09/1993 - 06/1998 Technical School TGM Vienna, Austria  
Automotive and Mechanical Engineering

## Professional Experience

03/2014 - present Robert Bosch AG, Hallein, Austria  
Development Engineer for Diesel Injection Systems

01/2007 - 04/2013 Vienna University of Technology, Austria  
Assistent at Institute of Fluid Dynamics and Heat Transfer  
Project: "Heat Transfer in a Reciprocating Compressor"  
European Forum for Reciprocating Compressors

08/2002 Intern at AVL List GmbH, Graz, Austria

08/2001 Intern at AVL List GmbH, Graz, Austria

08/2000 - 09/2000 Intern at Volkswagen AG, Wolfsburg, Germany

08/1996 Intern at BMW Wien GmbH, Vienna, Austria

08/1995 Intern at Schindler Aufzüge/Fahrtreppen AG, Vienna, Austria